University of Strathclyde
Department of Electronic and Electrical Engineering

Resilience-Oriented Hierarchical Energy Management and Dynamic Inertia Damping Method for Renewable-Integrated Grid-Forming Converters

Ayse Colak

A thesis submitted in fulfilment of the requirements for the degree of Doctor of Philosophy

2026

This thesis is the result of the author's original research. It has been composed by the author and has not been previously submitted for examination which has led to the award of a degree.

Signed: Ayse Colak

Date: 07/06/2026

Acknowledgments

This thesis would not have been possible without the guidance and help of several individuals who contributed and extended their valuable assistance in the preparation and completion of this study. It is a pleasure to thank those who made it a possibility.

Firstly, I am indebted to my supervisor, Professor Khaled Ahmed, whose guidance, support, and expertise enabled me to complete my PhD within the shortest possible time frame. He was always available to help with any problems, both academic and non-academic. Special thanks to my colleague, Mohamed Abouyehia, for his generous help and support. I also want to thank all the amazing people I met in Glasgow, especially the PEDEC group, for making my PhD journey memorable.

I am deeply grateful to my family, who always supported my choices in life. Any success I have achieved would not have been possible without their unwavering support. My mum, Necla Colak, supported me throughout my entire PhD journey with unconditional love from miles away. My dad, Ilhami Colak, provided financial and academic support whenever needed, inspiring me with his own academic success, having completed his PhD 30 years ago. My siblings, Medine Colak and Alperen Colak have been a source of strength and encouragement. I feel incredibly lucky to have you both as my siblings.

This thesis is dedicated to my dad whose ambition and drive, greater even than my own, were the true forces behind this work.

Abstract

As power systems evolve to incorporate more renewable energy sources, it faces new challenges in maintaining grid stability and reliability, especially during critical situations such as black start events, emergency conditions that necessitate load shedding, and the resulting power imbalance transients. The inherent variability of renewable sources complicates the grid's ability to quickly and efficiently recover from outages.

One of the main research problems in modern power systems is the difficulty in managing the intermittent nature of renewable energy sources during disturbances and system restoration. Traditional energy management and restoration methods were mainly developed for conventional centralised power plants and are not fully suitable for power systems with high renewable energy penetration. Rapid changes in renewable generation, sudden load variations, and power imbalances during emergency conditions can affect system frequency, voltage stability, and overall reliability. In addition, the lack of proper coordination between transmission and distribution networks reduces the effectiveness of load shedding, black start operation, and service restoration. These challenges make it difficult to maintain stable and reliable grid operation and increase the restoration time after major outages.

To address these challenges, the investigations in this thesis begin by proposing a novel energy management system (EMS) at both distribution and transmission levels with a hierarchical order. This advanced energy management involves not only predicting and reducing fluctuations due to renewable sources but also ensuring that power can be rapidly and efficiently redistributed during outages. This thesis is essential in addressing the dual challenges of maintaining system reliability and stability in the face of increasing renewable energy integration while simultaneously advancing toward a more sustainable energy future. The proposed method is validated in the IEEE 10-Bus test network and IEEE 39-Bus test network using MATLAB/Simulink.

The key findings demonstrate that the proposed hierarchical energy management system effectively improves load shedding performance, enhances system stability, and increases renewable energy utilisation during black start conditions. Coordination between transmission and distribution controllers enabled efficient restoration of critical loads and improved support between interconnected network areas. In addition, the proposed control strategy prioritised renewable energy sources, particularly solar generation, during the restoration process, contributing to a more reliable and sustainable power system operation.

Another important challenge for future power system integration is the low inertia and damping properties due to the characteristics of renewable energy sources. This transition necessitates the development of grid-forming converters that can emulate the dynamic behaviour of synchronous machines to preserve grid stability and maintain a reliable electricity supply.

This thesis proposes a frequency and power dependent dynamic inertia damping controller designed for droop-based grid-forming converters. This innovative method significantly improves upon existing techniques by optimizing the interaction between inertia, active power, and frequency. Crucially, it departs from traditional methods that depend predominantly on static power or frequency metrics. Through an advanced mathematical model, the thesis establishes a dynamic correlation between per-unit inertia and real-time frequency as well as power fluctuations. A novel dynamic inertia damping controller is applied to the IEEE 9-bus system to demonstrate its practical effectiveness. The validation process employs the PLECS platform to verify the controller's performance under different operating conditions. Notably, the inclusion of dynamic inertia damping proves especially useful during critical grid events such as black starts and load shedding transitions, where rapid and accurate system response is essential. This method not only improves the precision of the damping responses but also ensures better adaptability and robustness in grids with a substantial presence of renewable energy sources.

Acronyms/Abbreviations

AGC	Automatic Generation Control
BESS	Battery Energy Storage Systems
BSA	Black Start Area
BSU	Battery Storage Unit
CIG	Converter-interfaced Generators
DC	Direct Current
DER	Distributed Energy Resources
DL	Distribution Line
DSP	Digital Signal Processor
EFR	Enhanced Frequency Response
EMS	Energy Management Systems
ESS	Energy Storage System
EV	Electric Vehicle
FCP	Fuel Cell Power
FFR	Fast Frequency Response
GFC	Grid Forming Controller
GFL	Grid Following
GFM	Grid Forming
GHz	Gigahertz
GP	Grid Power
GW	Gigawatt
HILP	High Impact Low Probability
HLC	High Level Controller
iPOD	Intelligent Power Oscillation Damper
LLC	Low Level Controller
LQR	Linear-quadratic Regulator
MPPT	Maximum Power Point Tracker
MVA	Mega Volt-Amperes
MVAR	Mega Volt-Amperes Reactive
MW	Megawatt
NBS	Non-Black Start

NBSA	Non-Black Start Area
NESO	National Energy System Operator
P&O	Perturb and Observe
PCC	Point of Common Coupling
PFR	Primary Frequency Response
PLECS	Piece-wise Linear Electrical Circuit Simulation
PSS	Power System Stabilisers
PV	Photovoltaic
RES	Renewable Energy Sources
RoCoF	Rate of Change of Frequency
SCR	Short-Circuit Ratio
SoC	State of Charge
STATCOM	Static Compensator
SynComn	Synchronous Compensator
TL	Transmission Line
TSO	Transmission Line System Operator
VSM	Virtual Synchronous Machine

Table of Contents

Acknowledgments iii

Abstract v

Acronyms/Abbreviations vii

List of Figures xiv

List of Tables xvii

Chapter 1 Introduction 1

1.1. Background 1

1.2. Research Motivation 2

1.3. Aim and Objectives 3

1.4. Publications 4

1.4.1. Journal Papers 4

1.4.2. Conference Papers 4

1.5. Thesis Structure 5

Chapter 2 Literature Review 7

2.1 Introduction 7

2.2. Challenges in Modern Power Systems 7

2.2.1. Rise of Renewable Energy and System Decentralisation 8

2.2.2. Low Inertia and Frequency Stability Issues 10

2.3. Energy Management Systems in Modern Power Networks 12

2.3.1. Traditional EMS Architectures and Core Objectives 12

2.3.2. EMS for Microgrids and Distributed Energy Resources 13

2.3.3. Hierarchical and Decentralised EMS: Recent Trends 13
2.3.4. Resilience-Oriented EMS: Load Prioritisation and Black Start Coordination 16
2.3.5. Limitations of Existing EMS Architectures 17
2.4. Dynamic Inertia and Damping Control in Converter-Dominated Grids 19
2.4.1. Role of Inertia and Damping in Power System Stability 19
2.4.2. Synthetic and Virtual Inertia Techniques 20
2.4.3. Damping Control Strategies for Grid-Forming Converters 22
2.5. Co-Optimised EMS and Damping Control Frameworks 22
2.6. Summary of Identified Gaps 25
2.6.1. Identified Gaps in the State of the Art 25
Chapter 3 Novel Hierarchical Energy Management System 27
3.1. Proposed EMS Method 27
3.1.1. Operational Framework of DL-EMS in Non-Black Start-Capable Areas (NBSAs) 29
3.1.2. Operational Framework of DL-EMS in Black Start-Capable Areas (BSAs) 30
A. Normal Operation Path 31
B. Black Start Operation Path 32
C. Load Shedding Path 34
D. Night Operation Path 35
E. Emergency Operation Path 36
3.1.3. Operational Framework of TL-EMS for High-Level Controller (HLC) 36
3.2 Objective Function of the Optimisation Problem 39

Constraints of the Optimisation Problem....42
3.3. Summary....44
Chapter 4 System Modelling and Simulation Validation....46
4.1 Model Derivation and Parameter Definition....46
4.2 Modelling of the PV System with Converter Control for AC Coupling....47
4.2.1 PV Array Modelling....48
4.2.2 Converter Control Architecture....48
A. Maximum Power Point Tracking (MPPT)....49
B. DC-Link Voltage Regulation....49
C. Current Control (d-q Frame)....50
D. PWM and Modulation....50
4.2.3 Critical Modelling Considerations....50
4.3 Battery Energy Storage System and Converter Control for Grid-Following AC Coupling....51
4.3.1 Lithium-Ion Battery Dynamic Model....51
4.3.2 Converter Control for AC-Coupled Battery System....52
A. Grid-Following (GFL) Control Mode....53
B. Grid-Forming (GFM) Control Mode....54
C. Control Mode Selection Based on Grid Strength....55
D. PWM and Synchronization....55
4.3.3 Limitations and Assumptions....55
4.4 Fuel Cell System Modelling for Power Flow Analysis....56

4.4.1 Modelling Approach and Justification 56

4.4.2 Simplified Dynamic Fuel Cell Model 56

4.4.3 Integration with Power Flow Control 57

4.4.4 Assumptions and Limitations 57

4.5 Load and Coupling System 58

4.5.1 Load Classification and Control 58

4.5.2 Electrical Coupling and Voltage Interface 59

4.5.3 Integration with Energy Management System (EMS) 59

4.6 Model Validation Through Simulation Studies 59

4.6.1. DL-EMS in a BSA 60

4.6.2 TL-EMS under the HLC 66

4.6.3 Comparative Analysis 75

4.6.4 Additional Analysis on the IEEE-10 Bus System 81

4.7. Summary 91

Chapter 5 A Frequency and Power Dependent Virtual Dynamic Inertia Damping Method for Grid Forming Converters 93

5.1. Proposed Damping Method Structure 93

5.2 System Performance and Stability Analysis 98

5.2.1. Frequency Response Analysis 98

5.2.2. Phase Portrait Analysis of System Dynamics 99

5.2.3. Equilibrium Point Analysis 101

5.2.4. Small-Signal Stability Analysis 103

5.2.5. Gain Design Constraints for Stability and Robustness 105

5.3. Results and Discussion 107

Case Study 1: Response to a 50 MW Step Load 109

Case Study 2: Response to Transmission Line Disconnection 111

Case Study 3: Comparative Analysis with Existing Damping Methods 112

5.4. Summary 114

Chapter 6 Conclusions and Future Work 116

6.1. Conclusions 116

6.2. Author's Contributions 116

6.3. Future Work 117

References 120

Appendix A: The EMS Algorithm 128

List of Figures

Figure 1-1 Overview of the research process 3
Figure 2-1Projected trends and shifts in power generation over the 2025-2050 horizon[11] . .8
Figure 2-2 Centralised and distributed power generation system [16]. 9
Figure 3-1 The proposed hierarchical energy management system including both DL -EMS and TL -EMS. 28
Figure 3-2 Flow chart of DL-EMS in non-black start-capable areas (NBSAs).....30
Figure 3-3 Generation capability curve. 31
Figure 3-4 Flow chart of DL-EMS in black start-capable areas (BSAs): detailing the paths for normal operation and black start support. 33
Figure 3-5 Flow chart of DL-EMS in black start-capable areas (BSAs): detailing the paths for night operation, load shedding, and emergency operation. 34
Figure 3-6 Flow chart of TL − EMS for the centralised HLC. 37
Figure 4-1(a) Daily power flow in the normal scenario: solar, battery, BSA load, fuel cell power, and grid interaction power. (b) Normal scenario battery SoC and DC voltage of the PV side throughout the day. 61
Figure 4-2 (a) Daily power flow in load shedding scenario: solar, battery, BSA load, fuel cell power, and grid interaction power. (b) Load shedding scenario battery SoC throughout the day 62
Figure 4-3 (a) Daily power flow in night and emergency scenarios: solar, battery, BSA load, fuel cell power, and grid interaction power. (b) Night and emergency scenario battery SoC and remaining fuel percentage in the fuel tank throughout the day. 63
Figure 4-4 Comprehensive diagrams of transmission and distribution networks: (a) detailed diagram of the IEEE 39-Bus transmission system with minimum-impedance path determination for black start restoration using Dijkstra's algorithm between BSAs and NBSAs, and (b) detailed diagram of the distribution network for the BSAs. 66
Figure 4-5 Information received from BSAs: (a) reserve power distribution and load status in BSAs; (b) battery SoC and remaining fuel percentage in BSAs 68
Figure 4-6 Information received from BSAs: (a optimal power allocation for G3 startup from BSAs; (b) SoC and fuel percentage post-cranking for G3. 69
Figure 4-7 Information received from BSAs: (a) optimal power allocation for G4 and G2 startup from BSAs; (b) SoC and fuel percentage post-cranking for G4 and G2. 70

Figure 4-8 Information received from BSAs: (a) optimal power allocation for G1 startup from BSAs; (b) SoC and fuel percentage post-cranking for G1.....72
Figure 4-9 Information received from BSAs: (a) optimal power allocation for G5 startup from BSAs; (b) SoC and fuel percentage post-cranking for G5.....73
Figure 4-10 Comparative analysis of TL-EMS methods on IEEE 39 buses for black start: (a) generator startup times using the two methods against the proposed method; (b) computational time required by the three methods for optimising the black start on IEEE 39 buses; (c) system generation capacity during the black start process. The methods compared include the Proposed method, the method by El-Zonkoly 2015 [105], and the method by Su et al. 2022 [106].....79
Figure 4-11Comparative analysis of DL−EMS methods: (a) results of methods in [107]; (b) results of the proposed method. 81
Figure 4-12 Results for the cloudy day scenario. (a) Power supply and consumption during the morning, (b) battery SoC and fuel percentage during the morning, (c) power supply and consumption during the night, and (d) battery SoC and fuel percentage during the night.....84
Figure 4-13 Results for the sunny day scenario. (a) Power supply and consumption during the morning, (b) battery SoC and fuel percentage during the morning, (c) power supply and consumption during the night, and (d) battery SoC and fuel percentage during the night.....87
Figure 4-14 Minimum-impedance path determination using Dijkstra's algorithm for black start restoration between BSAs and NBSAs for IEEE-10 bus standard system.....88
Figure 4-15 Information received from BSAs: (a) Optimal power allocation for G2 start-up from BSAs, (b) SoC and fuel percentage post-cranking for G2.....89
Figure 4-16 Information received from BSAs: (a) Optimal power allocation for G1 start-up from BSAs, (b) SoC and fuel percentage post-cranking for G1.....90
Figure 4-17 Computational time for optimization algorithm across various IEEE bus systems. 91
Figure 5-1: Integration of the proposed add-on controller within the traditional droop control loop. 98
Figure 5-2: Magnitude response of the system with varying gain K.....99
Figure 5-3: Phase response of the system with varying gain K.....100
Figure 5-4: Phase portrait analysis of system dynamics with varying gain K.....100
Figure 5-5: System response ($\Delta\omega$) over time for different values of the controller gain k at a droop coefficient $mp = 0.02$.....105

Figure 5-6: IEEE-9 Bus. 108
Figure 5-7: Control hardware-in-the-loop validation. 1) PLECS RT simulator, 2) Box breakout board (for input/output interface), 3) DSP, and 4) Oscilloscope. 108
Figure 5-8: Real-time results for case study 1- system response to a 50 MW step load, (a) active power response, and (b) frequency response of grid forming converter 1. 110
Figure 5-9: Real-time results for case study 2- system response to a transmission line disconnection, (a) active power response, and (b) frequency response of grid forming converter 1. 112
Figure 5-10: Comparative transient response of active power output under 55 MW step load change, which illustrates the damping performance of the proposed method versus RoCoF-based, voltage-based, and virtual resistance-based damping methods. 114

List of Tables

Table 2-1 Key Characteristics and Functional Requirements of EMS for Microgrids and DERs 14
Table 2-2: Key characteristics of both centralised and decentralised control architectures [47]. 15
Table 2-3 Overview of energy management systems: capabilities and methodologies. 18
Table 2-4: Classification and Assessment of Damping Control Strategies for GFCs 23
Table 4-1 System Parameters 47
Table 4-2 PV Module Parameters (SunPower SPR-415E-WHT-D) 49
Table 4-3 Battery System Parameters 52
Table 4-4 Summary of Control Modes 55
Table 4-5 Data of generator characteristics [57] 67
Table 4-6 Time to complete restorative actions [104]. 74
Table 4-7 Actions to restore entire power system. 76
Table 4-8 Comparison of energy management system methods at distribution and transmission levels. 82
Table 4-9 Data of generator characteristics. 87
Table 5-1: System Parameters 101
Table 5-2 : Impact of gain K on maximum overshoot, settling time, and damping ratio with case study 1. 109
Table 5-3: Impact of gain K on maximum overshoot, settling time, and damping ratio with case study 2. 111

Chapter 1 Introduction

The importance of transitioning from traditional energy to renewable energy is becoming more critical day by day, especially for countries working towards net zero. As the adoption of renewable energy increases, many challenges arise, such as the increase in decentralised energy systems, energy optimisation, energy stability and reliability, and energy demand response. It is essential to have a reliable, secure, and efficient energy management system that addresses these issues at both the distribution and transmission levels. Another emerging issue is the low inertia and damping properties in power systems dominated by wind and solar power, which exposes a need to develop more robust and efficient damping solutions.

1.1. Background

The global energy landscape is undergoing a fundamental transformation, driven by the urgent need to decarbonise and transition towards sustainable power generation. This paradigm shift is characterised by the large-scale integration of Renewable Energy Sources (RES), such as solar photovoltaics (PV) and wind power, into national and international grids. Unlike the conventional power system, which has historically relied on large, centralised synchronous generators, the modern grid is becoming increasingly decentralised and dominated by converter-interfaced generation.

This architectural evolution introduces a profound technical challenge: the systemic reduction of rotational inertia. Synchronous generators inherently provide inertia through their large rotating masses, which naturally opposes sudden changes in grid frequency and support stability. As these units are displaced by RES, which are connect to the grid via power electronics and lack this physical property, the grid's overall inertia declines. Consequently, the power system becomes more vulnerable to disturbances, exhibiting a faster Rate of Change of Frequency (RoCoF) and a heightened risk of instability. This new paradigm of a low-inertia grid renders conventional control and management strategies insufficient, exposing a critical gap in ensuring operational security.

To bridge this gap, the focus of grid management must shift towards sophisticated, high-speed coordination of distributed assets. This directly motivates the evaluation of advanced Energy Management Systems (EMS). An EMS is no longer just a tool for economic optimisation but has become an essential platform for system stability. Its role is to orchestrate the collective

response of diverse resources including battery energy storage, controllable loads, and the RES themselves to emulate the stabilising properties once provided by synchronous machines. Therefore, the rigorous evaluation of an EMS's capability to provide these critical ancillary services, such as synthetic inertia and fast frequency response, is paramount to guaranteeing the reliability of the future power system.

1.2. Research Motivation

EMS play a critical role in efficiently and reliably integrating renewable energy sources into the power grid. A key challenge lies in the heterogeneous nature of these sources each with different dynamic behaviours, operational constraints, and levels of availability. For instance, solar cells may not always be available throughout the day or may produce excess power relative to system demand. In such cases, storing surplus energy and deploying it during periods of low generation becomes essential. Fuel cells, on the other hand, are often limited by high costs and are typically reserved for critical demand scenarios to ensure cost-effectiveness.

The increasing presence of diverse renewable resources introduces coordination complexity, which must be addressed through robust EMS frameworks. Efficient and effective utilization of these energy sources based on real-time system demand is vital for both cost optimization and system resilience. However, current EMS architectures often fall short in handling such diversity, especially in managing resource intermittency, prioritizing loads, and responding to disturbances in real time[1]. This underscores the need to enhance existing EMS designs by incorporating hierarchical control structures, emergency support mechanisms, and advanced optimization strategies ensuring scalable and sustainable energy system operation across both transmission and distribution levels. The overall research flow and its main stages are illustrated as shown in Figure 1.1.

Beyond the importance of EMS, addressing the low-inertia issue in renewable energy systems is essential for enhancing grid stability, improving reliability, and accelerating responses to disturbances. Although several damping methods have been proposed to mitigate the impact of low inertia system, they present inherent limitations, which are discussed in the following chapter. Many existing approaches rely on direct frequency measurements or power derivatives. However, these fail to capture critical real-time dynamics, thereby reducing the system’s responsiveness to sudden grid perturbations.

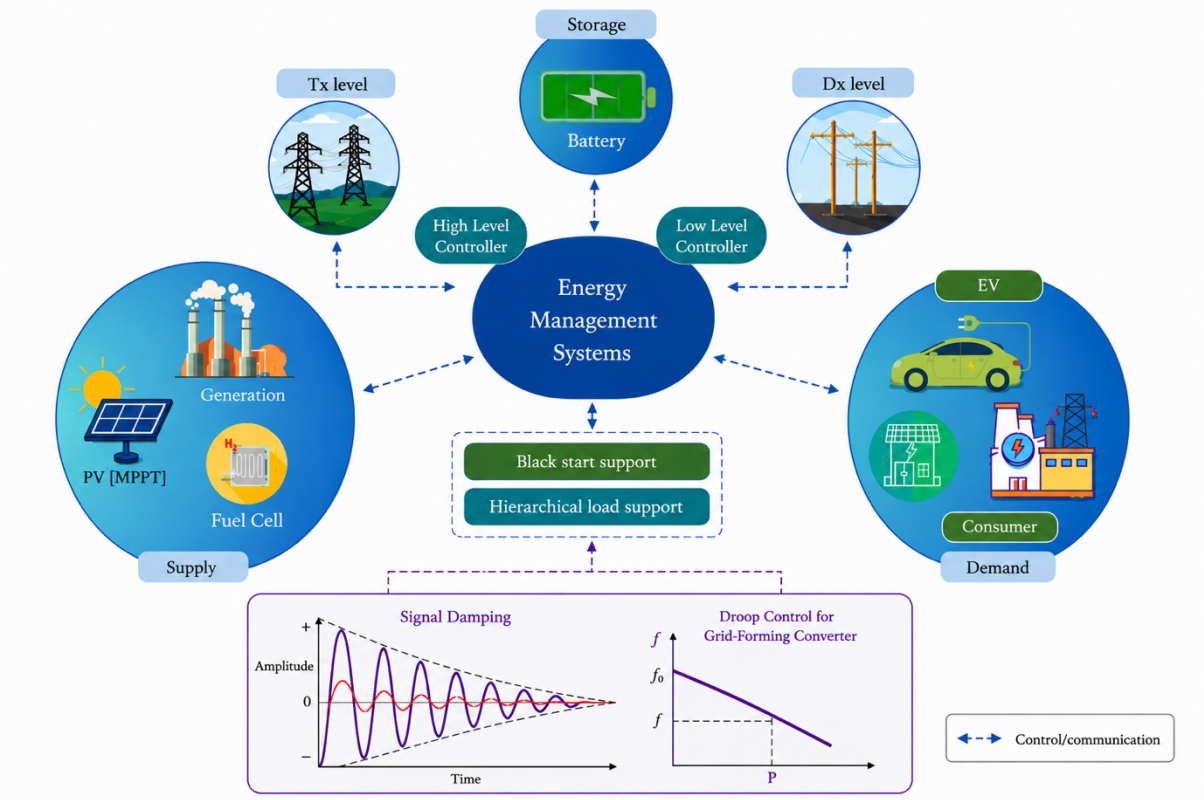

Figure 1-1 Overview of the research process

During EMS operation, significant variations in the power pattern can occur due to fluctuating generation and load demands. These rapid changes necessitate the use of effective damping mechanisms to maintain system stability. Given the strong coupling between dynamic inertia, active power, and frequency, integrating advanced damping methods into EMS frameworks becomes essential for accurately handling instant changes and ensuring fast, coordinated control actions. These shared limitations underscore the need for more robust and adaptable damping strategies that can operate in real time within evolving EMS architectures.

1.3. Aim and Objectives

Based on the research motivation, the investigation carried out in this thesis aims to provide insightful analysis and methods for energy management systems and damping techniques. Therefore, this thesis will achieve its aims by pursuing the following specific objectives:

1. To design and develop a hierarchical EMS capable of coordinating control actions across both transmission and distribution networks. The design will explicitly

incorporate functionalities for system-wide black start restoration and priority-based load shedding to enhance operational resilience.

2. To formulate and implement a multi-objective optimisation framework that integrates with the hierarchical EMS. This framework will be designed to enhance dynamic system stability by optimally coordinating synthetic inertia provision, intelligent load shedding, and the dispatch of renewable energy sources.
3. To develop and validate an advanced inertia and damping control algorithm for grid-forming converters. The objective is to improve the dynamic frequency response and ensure accurate power-sharing by optimising the real-time interaction between synthetic inertia, active power output, and system frequency.
4. To evaluate and quantify the performance of the integrated system through dynamic simulations on a benchmark low-inertia power system model. The evaluation will measure the improvement in key stability metrics, such as RoCoF, frequency nadir, and settling time, under various contingency scenarios.

1.4. Publications

The presented work resulted into couple of journal and conference papers as it is listed below.

1.4.1. Journal Papers

1. A. Colak, M. Abouyehia, and K. Ahmed, "Novel Hierarchical Energy Management System for Enhanced Black Start Capabilities at Distribution and Transmission Networks," *Energies*, vol. 17, no. 11, p. 2605, Jan. 2024, doi: https://doi.org/10.3390/en17112605.

2. A. Colak, M. Abouyehia, and K. Ahmed, "Novel Dynamic Inertia Damping Enhancement of Droop Control for Grid-Forming Converters," IET Power Electronics, vol.19, issue.1, March 2026, doi: https://doi.org/10.1049/pel2.70219.

1.4.2. Conference Papers

1. A. Colak and K. Ahmed, "A Brief Review on Capacity Sizing, Control and Energy Management in Hybrid Renewable Energy Systems," *2021 10th International Conference on Renewable Energy Research and Application (ICRERA)*, Sep. 2021, doi: https://doi.org/10.1109/icrera52334.2021.9598654.

2. A. Colak, Melike Selcen Ayaz, and K. Ahmed, "Long Term Benefits of Advanced Communication Techniques in Smart Grids," *2021 9th International Conference on Smart Grid (icSmartGrid),* Jun. 2021, doi: https://doi.org/10.1109/icsmartgrid52357.2021.9551259.

3. A. Colak, N. Guler, and K. Ahmed, "Intelligent Communication Techniques for Smart Grid Systems: A Survey," *2021 9th International Conference on Smart Grid (icSmartGrid),* Jun. 2021, doi: https://doi.org/10.1109/icsmartgrid52357.2021.9551027.

4. A. Colak, M. Abouyehia, and K. Ahmed, "Resilience and Frequency Control in Low-Inertia Power Systems: Challenges and Solutions," *2023 13th International Conference on Renewable Energy Research and Applications*, Oct. 2024.

doi: https://doi.org/10.1109/ICRERA62673.2024.10815552

5. M. Abouyehia, A. Colak, et.al "A Novel Fractional-Order Damping Control Method for Enhancing Synchronization in Grid-Forming Converters," *2025 13th International Conference on Smart Grid (icSmartGrid)*, May. 2025.

1.5. Thesis Structure

This thesis presents a comprehensive study on enhancing the resilience, stability and renewable integration capabilities of moder power systems through advance energy management and control strategies. It develops two distinct approaches to improve overall system performance.

The first approach proposed a novel hierarchical energy management system that operates across both transmission and distribution level. The systems prioritise renewable energy sources, optimises load shedding, introduces a coordinated strategy for black start operations, enabling faster and more reliable restoration of power in multi-area networks.

The second approach introduces a dynamic inertia damping enhancement for droop control in grid-forming converters. This technique dynamically adjusts synthetic inertia and damping based on frequency and active power variations, improving frequency stability and system response in renewable -rich power grids.

The remainder of this thesis is organised to present the research in a logical and progressive manner. The following chapter-by-chapter outline details the structure of the investigation, from the foundational literature review to the final conclusions and recommendations.

- **Chapter 2** presents a comprehensive literature review of existing EMS and power system damping techniques. This chapter establishes the theoretical foundation for the thesis by critically analysing the design principles, operational frameworks, and practical applications of conventional methods in low-inertia and renewable-heavy power networks. The limitations and disadvantages of current approaches are identified to establish the research gap.
- **Chapter 3** introduces the design and coordination of the proposed hierarchical energy management system. This chapter details the architecture of the novel EMS, focusing on its application at both the transmission and distribution levels. The discussion covers the methodologies for prioritising renewable energy sources, the strategies for implementing load shedding, and the protocols for a coordinated black-start operation.
- **Chapter 4** focuses on the validation of the proposed EMS. This chapter describes the simulation environment, which is based on the IEEE 39-bus and IEEE 10-bus test networks. The methodology for evaluating the system's performance is detailed, including the specific contingency scenarios used, such as blackouts and the integration of renewable energy sources. The chapter outlines the key performance indicators and metrics used to assess the practical applicability and benefits of the system.
- **Chapter 5** presents the development of a novel dynamic inertia damping enhancement technique for droop-control in grid-forming converters. This chapter describes the control method, which is based on the dynamic adjustment of inertia in response to frequency variations and active power. The validation methodology is also detailed, using the IEEE 9-bus system with simulations designed to assess the performance of the damping characteristics, particularly within renewable-rich energy environments.
- **Chapter 6** concludes the thesis by synthesising the primary findings and contributions of the research. This chapter provides a summary of the key scientific advancements presented and discusses the overall impact of the proposed methods on power system resilience and stability. Finally, it outlines potential directions for future research to further advance energy management and control in grids with high renewable penetration.

Chapter 2 Literature Review

2.1 Introduction

The global energy landscape is undergoing a transformative shift, driven by the urgent need to decarbonise electricity generation and accelerate progress toward net-zero emission targets [2]. This transition has resulted in the widespread integration of RES such as wind and PV, fundamentally altering the structure and dynamic behaviour of modern power systems [3]. Unlike conventional generation based on synchronous machines, renewable sources are typically interfaced through power electronic converters, which decouple the mechanical inertia from the grid [4]. As a consequence, traditional assumptions regarding frequency stability, system resilience, and operational control are being challenged. Amidst this transformation, power systems are facing a dual set of challenges. First, the variability and intermittency of RES introduce significant operational uncertainty, requiring advanced coordination and optimisation of generation and load [5]. Second, the reduction in system inertia due to the displacement of synchronous generators increases the RoCoF following disturbances, thereby heightening the risk of frequency instability and cascading failures [6]. These challenges are further exacerbated by increased system decentralisation, the proliferation of distributed energy resources (DERs), and the growing frequency of extreme weather events linked to climate change.

In this context, EMS have emerged as critical tools for ensuring the operational reliability, economic efficiency, and resilience of power systems [7]. Traditional EMS architectures, however, are often centralised, rigid, and limited in their ability to respond to the fast dynamics and distributed nature of modern grids [8]. Furthermore, existing EMS implementations frequently overlook essential aspects of system resilience, such as black start capabilities, load prioritisation, and real-time adaptability in the presence of uncertainty. At the same time, the lack of adequate damping and inertia control in converter-dominated grids necessitates the development of advanced control strategies that can emulate the dynamic behaviour of synchronous machines and provide synthetic inertia in real time.

2.2. Challenges in Modern Power Systems

The increasing decentralisation of generation, the proliferation of behind-the-meter technologies, and the influence of climate-related extreme events are further complicating grid

operations [9]. This subsection outlines the most pressing challenges facing modern power systems, starting with the systemic impacts of renewable energy integration and decentralisation, followed by a discussion of reduced inertia and frequency instability, and concluding with the vulnerability of modern grids to climate-induced high-impact, low-probability (HILP) events.

2.2.1. Rise of Renewable Energy and System Decentralisation

The increasing penetration of RES, particularly wind and solar, has emerged as a cornerstone of global decarbonisation strategies. As governments and utilities strive to meet climate agreements such as the Paris Accord [10], the share of RES in the global generation mix has surged. Figure 2.1 illustrates the projected trends in global power generation, highlighting the accelerating shift from synchronous conventional generation toward converter-based renewable sources. This trend, while environmentally beneficial, underscores the urgency of developing new control frameworks that can operate reliably in a system with low inertia.

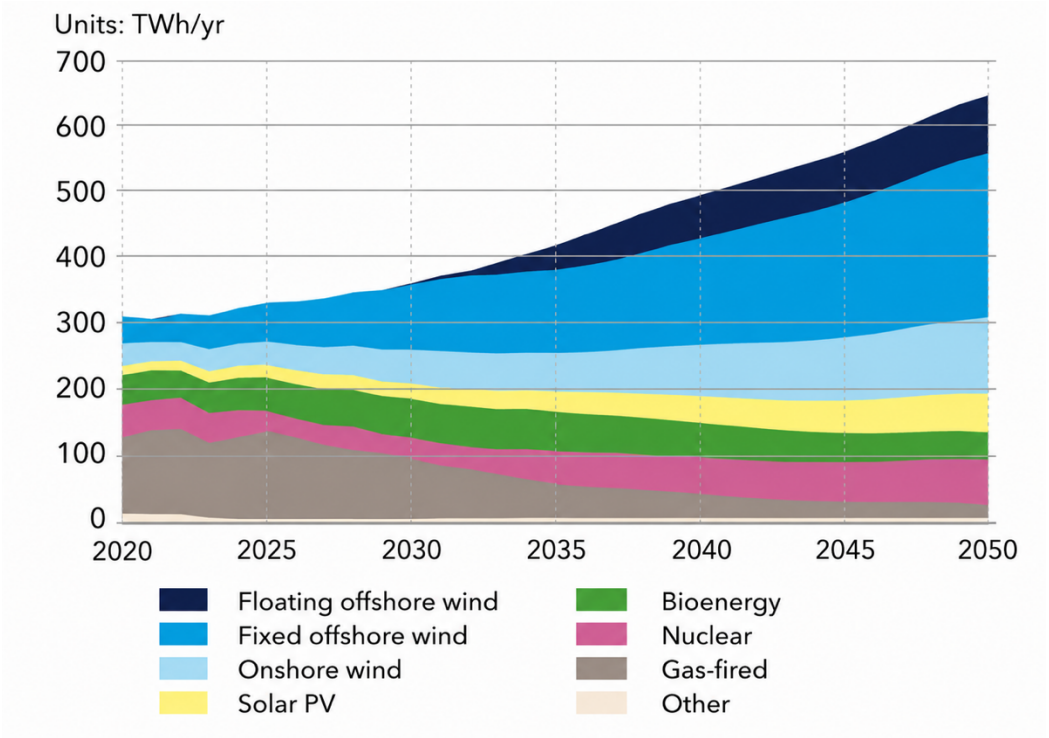

Figure 2-1Projected trends and shifts in power generation over the 2025-2050 horizon[11] .

Unlike conventional thermal power plants, which use large, rotating synchronous machines that inherently contribute to system inertia and stability, RES are typically connected to the grid via inverter based power electronic converters [4]. These converter-interfaced generators

(CIGs) decouple the mechanical dynamics of generation from the grid, resulting in a pronounced reduction in the system's ability to resist frequency deviations [12].The consequences of this shift are not just theoretical, they are already being observed in several power systems with high shares of inverter-based generation, including faster rates of RoCoF and deeper frequency nadirs [13].

In parallel, power systems are changing from a centralised to a decentralised model (Fig. 2.2). In the past, electricity flowed one way from large power plants to customers [14]. Now, many small, local power sources like rooftop solar, batteries, and electric vehicles are being added [15]. This creates a new system where power flows in two directions, which is different from the old design [16]. This change brings new challenges, making it harder to manage the grid, predict power needs, and control voltage [17]. System operators often cannot see or control these new power sources [18, 19]. Because these new sources are all diverse, variable, and often less predictable than traditional generation, it becomes more challenging to maintain the balance between supply and demand, ensure system stability, and sustain overall grid reliability [20].

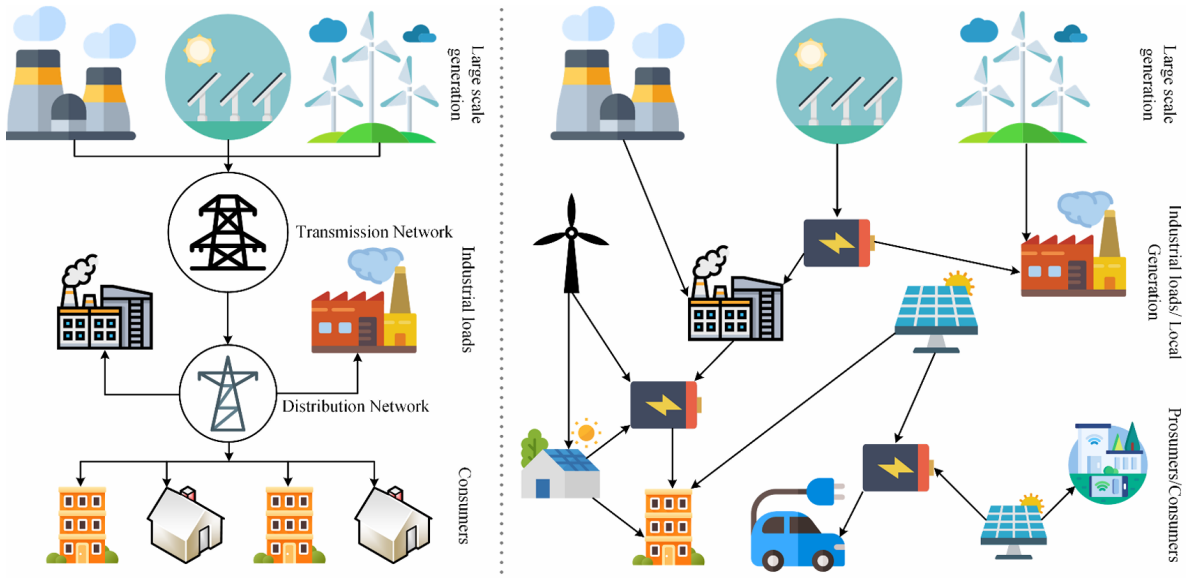

Figure 2-2 Centralised and distributed power generation system [16].

In addition to technical challenges, decentralisation also raises questions related to system ownership, control boundaries, and market integration. The rise of prosumers (entities that both consume and produce electricity) introduces new actors into the energy value chain [21].

Coordinating their participation in frequency regulation, voltage support, and black start recovery requires not only technical solutions but also regulatory and policy innovations.

In summary, the rise of renewable energy and system decentralisation has fundamentally altered the operational context of modern power networks. These trends demand a departure from traditional, centralised grid management practices and necessitate the design of intelligent, decentralised, and resilient EMS. Such systems must be capable of coordinating diverse resources, predicting system conditions, and responding dynamically to disturbances in real time, all while ensuring that sustainability goals are not achieved at the expense of grid reliability or stability.

2.2.2. Low Inertia and Frequency Stability Issues

The integration of RES through converter-interfaced generators has led to a paradigm shift in the dynamic behaviour of modern power systems, particularly with respect to system inertia and frequency stability [4]. As outlined in the previous section, conventional synchronous generators, due to their large rotating masses, inherently provide inertia to the grid, allowing it to resist sudden changes in frequency following disturbances such as load-generation imbalances or generation outages. In contrast, most renewable energy technologies, including solar PV and many wind turbine configurations, are decoupled from the grid frequency via power electronic converters [4]. This decoupling eliminates the natural inertial response, resulting in what is now widely recognised as a “low-inertia” power system.

System inertia plays a critical role in the first few seconds following major disturbances. When a sudden imbalance between generation and demand occurs, inertia slows the RoCoF [13], providing a temporal buffer for primary frequency control mechanisms (e.g., governor response or fast frequency response from batteries) to activate. In the absence of sufficient inertia, frequency deviations occur much more rapidly, increasing the risk of under-frequency load shedding, generator tripping, or even system-wide blackouts [22].

Recent studies have shown that with high levels of RES penetration, system inertia can fall below critical thresholds, especially during periods of low conventional generation [23]. For example, in the Republic of Ireland power system, which is one of the most renewable-intensive grids in the world, system operators have had to impose inertia floors and dynamically curtail RES output to maintain frequency stability [24]. Similarly, in the UK, the National Energy System Operator (NESO) has developed Enhanced Frequency Response (EFR) services to mitigate the effects of low inertia by incentivising fast-acting assets such as batteries

to respond within one second of a frequency deviation [25, 26] pg 35.

The technical mechanism behind this instability is rooted in the physics of the swing equation:

$$M\frac{d\omega}{dt} = P_m - P_e \tag{2.1}$$

Where M is the inertia constant (proportional to the kinetic energy in the rotating mass), ω is the angular frequency, P_m is the mechanical input power, P_e is the electrical output power. Inertia represents the ability of a power system to resist sudden changes in frequency by temporarily storing and releasing kinetic energy. In conventional synchronous machines, the rotating masses of turbines and generators inherently provide this inertial response. During disturbances such as sudden load increases or generation losses, the stored kinetic energy is instantaneously released to compensate for the power imbalance, thereby slowing the rate of frequency deviation and supporting system stability. This natural inertial behaviour is essential for maintaining frequency stability, reducing the RoCoF, and allowing sufficient time for primary and secondary frequency control mechanisms to react.

In low-inertia systems, the value of M is significantly reduced, causing $\frac{d\omega}{dt}$ (i.e., RoCoF) to increase sharply in response to any power imbalance. This reduction is mainly associated with the growing penetration of renewable energy sources interfaced through power electronic converters, which do not inherently contribute rotational inertia like synchronous machines In the event of a sudden increase in demand or a loss of generation, this results in deeper frequency nadirs and increased likelihood of triggering under-frequency protection schemes or frequency collapse. Conversely, a sudden loss of load leads to over-frequency transients, which may trigger over-frequency relay protection. In both cases, the reduced inertia makes the system more sensitive to disturbances, increasing the need for fast, precise, and coordinated frequency control.

Despite these promising developments, inertia emulation is not without limitations. Synthetic inertia often involves delays in frequency measurement and control response, which can undermine its effectiveness [27]. Additionally, without proper coordination, multiple inertia-emulating devices may interact in unintended ways, potentially destabilising the system [28]. Grid-forming control (GFC) strategies, such as virtual synchronous machines, synchronverters, and droop-based GFCs, offer more robust solutions but require advanced tuning and validation in diverse network conditions[29].

In summary, the reduction of system inertia due to RES integration is one of the most critical technical challenges for modern power systems. It undermines frequency stability, complicates protection schemes, and necessitates the development of fast, intelligent, and adaptive control strategies. While synthetic and virtual inertia methods provide partial remedies, they must be carefully integrated within a broader energy management and control framework.

2.3. Energy Management Systems in Modern Power Networks

In light of the operational challenges associated with centralised and decentralised control structures and reduced system inertia challenges discussed in Section 2.2, it is evident that modern power systems require advanced control and coordination frameworks capable of operating under conditions of high uncertainty, variability, and decentralisation. EMS play a central role in achieving secure, reliable, and economic power system operation. This section critically reviews the evolution of EMS architectures and identifies the key limitations of current EMS implementations.

2.3.1. Traditional EMS Architectures and Core Objectives

EMS are centralised software and hardware platforms designed to monitor, control, and optimise the operation of power systems in real time. They are typically deployed at the transmission system operator (TSO) level and serve as the nerve centre of grid operations. The development of EMS architectures dates back to the mid-20th century, evolving in parallel with the expansion of large-scale, centralised electricity grids dominated by dispatchable thermal generation [30].

Traditional EMS architectures are centralised by design. All monitoring data is collected and processed at a central control centre, which then issues commands to generation units and grid assets [31]. This architecture was highly effective in vertically integrated systems characterised by a small number of large generators, predictable load patterns, and relatively slow system dynamics. However, this centralised paradigm introduces several limitations in the context of modern power systems, such as, scalability constraints, latency and communication bottlenecks, vulnerability to single points of failure, and inadequate support for emerging services [32].

Moreover, the effectiveness of traditional EMS is rooted in a set of implicit assumptions, including, generation is dispatchable and predictable, load is passive and uncontrollable, grid

topology is static and hierarchical, frequency control is provided by synchronous inertia and governor response, and restoration is centrally coordinated through planned black start procedures [31].

In a modern context, these assumptions are increasingly invalid. Loads are evolving from passive loads, which traditionally consume electricity in a fixed or predictable manner without responding to system conditions, to active loads, which can adjust their consumption, provide flexibility, or even inject power in response to signals (e.g., EVs, smart appliances). At the same time, generation is intermittent and distributed, and control actions must now be responsive to both fast transients and long-duration uncertainties[24]. As such, while traditional EMS architectures provide a foundational starting point, they are insufficient for managing the complexity, speed, and uncertainty of future grid operations.

2.3.2. EMS for Microgrids and Distributed Energy Resources

As power systems transition from centralised, bulk-generation paradigms to decentralised architectures characterised by locally embedded generation and storage, the role of EMS has fundamentally shifted. Traditional EMS, designed for top-down control of transmission networks, lack the agility, granularity, and autonomy required to manage the operational complexity of microgrids and high-penetration distributed energy resource (DER) environments. In response, a new generation of EMS solutions is emerging, marked by distributed intelligence, real-time adaptability, and interoperability. Table 2.1 outlines the distinguishing features, functions, and architectural imperatives of modern EMS for microgrids and DERs, alongside the supporting literature.

2.3.3. Hierarchical and Decentralised EMS: Recent Trends

The increasing complexity of modern power systems, driven by the proliferation of DERs, growing demand-side participation, and the imperative for enhanced resilience, has catalysed a shift from monolithic, centralised EMS architectures toward more modular, decentralised, and hierarchical frameworks [14, 33]. Hierarchical EMS architectures have thus emerged as a promising paradigm to bridge the control gap between centralised transmission operations and decentralised distribution management. A typical hierarchical EMS consists of three control layers. The tertiary layer operates at the transmission level. The secondary layer operates at the distribution or microgrid level. The primary layer operates at the device level, executing real-time voltage and frequency regulation, MPPT, and current control[34].

Table 2-1 Key Characteristics and Functional Requirements of EMS for Microgrids and DERs

Aspect	Description	Reference(s)
System Architecture	Transition from centralised to localized or hierarchical EMS to support distributed assets embedded in the distribution grid.	[31]
Operational Complexity	EMS must manage variability in local generation, real-time load balancing, and seamless transitions between grid-connected and islanded modes.	[31]
Control Frequency	Requires faster control and optimization cycles (real-time or near real-time), unlike traditional hourly/daily scheduling.	[35]
Forecasting Integration	Incorporates advanced forecasting tools (e.g., machine learning, time-series models) to predict generation, load, and contingencies.	[36]
Adaptive Decision-Making	Utilises algorithms that support control under uncertainty, targeting objectives like cost minimisation, reliability, and emissions reduction.	[37, 38]
Multi-Agent Coordination	Coordinates DERs owned by diverse stakeholders using distributed control approaches, market signals, or consensus-based mechanisms.	[39]
Emerging Market Mechanisms	Integration of peer-to-peer energy trading, virtual power plants (VPPs), and demand response to enhance flexibility and resource utilisation.	[40] [41] [42]
Edge Intelligence & Control	Embeds intelligence at the device level, enabling edge computing to reduce latency and improve responsiveness and fault tolerance.	[43]
Regulatory Compliance	EMS must incorporate grid support functions (e.g., voltage ride-through, reactive power control) as required by updated interconnection standards.	[20, 44]
Cybersecurity & Resilience	Designs must address increasing needs for cybersecurity, data privacy, and operational resilience in distributed, digitalized environments.	[45]

One of the key advantages of hierarchical EMS is its ability to coordinate distributed assets without overwhelming the central controller. Local and regional EMS units can autonomously manage their respective subsystems, while periodically communicating with higher-level controllers to report status, receive setpoints, or participate in global optimisation routines [31].

This distributed intelligence not only reduces the computational burden on the central EMS but also enables faster response times, greater fault tolerance, and improved resilience against communication failures or cyber threats.

Despite its many advantages, the deployment of hierarchical EMS architectures is not without challenges. One of the primary issues lies in the standardisation of communication protocols and data models across EMS layers [46]. Interoperability remains a key barrier, particularly when integrating legacy infrastructure with modern digital platforms. Furthermore, the complexity of coordinating objectives across multiple layers, each with its own control horizon, constraints, and priorities, necessitates robust coordination strategies and real-time data exchange.

Table 2-2: Key characteristics of both centralised and decentralised control architectures [47].

Feature	Centralized Control	Decentralized Control
Reliability	Moderate to low dependability	Generally high dependability
Decision-making	All decisions managed by a well-informed central controller	Decisions made by local controllers with limited global insight
Communication Demand	Heavy data exchange load	Minimal communication requirements
Information Flow	Data sent upward to the master controller and commands issued downward	Shared information between neighbouring units without hierarchy
Adaptability / Flexibility	Structural changes require controller modification; limited adaptability	Easily scalable and supports smooth integration of new subsystems
Risk of Failure	Sensitive to single-point failures that can stop the whole system	More resilient; local faults are isolated and rerouted
Technique Development	Mature and proven methods from conventional grid systems	Partly developed; ongoing research for new control concepts
Operational Goal	One unified target set by the central entity	Multiple objectives or owners with independent goals
System Configuration	Fixed structure, rarely modified	Dynamic structure allowing frequent expansion
Major Advantages	Consistent coordination, unified control, secure centralised data management	Local flexibility, faster local response, easy expansion, and better data privacy
Main Drawbacks	Needs large communication bandwidth and high computational power at centre; single-point vulnerability	Limited global awareness; system-wide optimization more difficult

Table 2.2 summarises the key characteristics of both centralised and decentralised control architectures. To summarise, by enabling distributed decision-making, enhancing scalability,

and improving resilience, these frameworks offer a viable path forward for managing the growing complexity of power system operations under high renewable penetration, active demand participation, and increasing climate-induced uncertainty. The next step in this evolution involves embedding resilience logic, such as load prioritisation, black start coordination, and fault recovery, directly within the EMS framework, as explored in the following subsection.

2.3.4. Resilience-Oriented EMS: Load Prioritisation and Black Start Coordination

Traditional EMS platforms, even when adapted for decentralised or hierarchical control, often lack intrinsic mechanisms for navigating prolonged outages, extreme contingencies, or system recovery under partial observability [48]. In this context, the concept of resilience within EMS extends beyond preventive planning or fault detection; it encompasses the ability to actively prioritise critical functions, autonomously initiate recovery procedures, and adapt to degraded or isolated grid conditions in real time [46].

A resilience-capable EMS must therefore incorporate a context-aware load classification mechanism that evaluates both static designations and dynamic parameters (e.g., real-time resource availability, forecasted outage duration, or local storage levels) to determine optimal load shedding or restoration sequences [49]. Complementing load prioritisation is the equally critical function of black start coordination. In conventional systems, black start procedures are pre-defined, centrally managed, and reliant on a small number of designated generating units with self-starting capabilities. However, in high-DER environments with fragmented system topologies and variable generation profiles, such rigid and centralised black start strategies are increasingly inadequate. A modern, resilience-oriented EMS must instead support distributed black start logic, whereby multiple subsystems, each potentially capable of partially restoring service, coordinate autonomously to re-energise segments of the grid.

The integration of distributed black start into EMS design involves several key capabilities. First, the EMS must be able to detect islanded conditions and assess local resource adequacy to determine whether a black start attempt is feasible. This includes evaluating the availability of converter-based resources with grid-forming capabilities, stored energy reserves, and load composition. Second, the EMS must synchronise restoration actions with neighbouring systems, using either direct communications or indirect methods such as synchro phasor measurements, to avoid phase, frequency, or voltage mismatches that could destabilise the recovering grid. Finally, the EMS must incorporate decision logic that can sequence restoration

steps, including energising feeders, reconnecting loads in priority order, and coordinating with upstream controllers as larger segments of the grid are reconstituted.

Despite the clear benefits offered by the resilience-oriented EMS, it has received limited attention in existing research. For instance, in [50, 51] focus on management strategies for electric vehicle charging to reduce costs, but they overlook considerations for black start capabilities and broader network-level implications. Similarly, the authors of [52, 53] propose optimising microgrid profits to enhance community welfare, yet they also fail to address the importance of black start capabilities. Efforts have also been made to balance multiple objectives in energy management using complex machine learning algorithms, as demonstrated in [54, 55]. However, these studies do not directly address the critical issues of black start capabilities or the inherent complexity of the proposed algorithms.

The authors of [56] explore maximising active power reserve in isolated microgrids using nonlinear optimisation, yet they overlook the management of black start recovery alongside renewable resource integration.

On the other hand, some authors broaden the focus on black start capabilities, each contributing different insights into emergency recovery mechanisms. For instance, the authors of [57] enhance the utilisation rate of photovoltaic systems and the state of charge tracking, which effectively manage energy during critical recovery phases. However, they do not address broader energy distribution optimisation challenges at both distribution and transmission levels. Conversely, the authors of [58] tackle key issues such as voltage and frequency support during black start but lack a comprehensive optimisation framework, which limits the energy management capability. Similarly, the authors of [59] focus on minimising voltage and frequency transients but fail to address broader grid management and constraints in their optimisation problem. Table 2.3 provides a detailed comparison of energy management systems as proposed in the literature.

2.3.5. Limitations of Existing EMS Architectures

Despite recent advancements, current EMS frameworks face several technical and operational obstacles that hinder their performance in modern power grids. The following points highlight the primary limitations of existing architectures:

Table 2-3 Overview of energy management systems: capabilities and methodologies.

Ref.	Black Start Support	Level Implementation	Renewable Energy	Complexity	Timeframe
[50, 51]	No	Distribution	Yes	Linear programming	Day ahead
[52, 53]	No	Distribution	Yes	Reinforcement learning	Day ahead
[54, 55]	No	Distribution	Yes	Machine learning	Day ahead
[60, 61]	No	Distribution	No	Nonlinear programming	Day ahead
[62, 63]	No	Distribution	Yes	Two-stage nonlinear optimisation	Day ahead
[56]	No	Distribution	Yes	Nonlinear optimisation problem	Real time
[64]	No	Distribution	Yes	Mixed-integer linear programming	Day ahead
[57]	Yes	Distribution	Yes	Model predictive control	Day ahead
[58]	Yes	Distribution	Yes	Algorithmic approach	Day ahead
[59]	Yes	Distribution	Yes	No optimisation included	Real time
[65, 66]	No	Distribution	No	Quadratic programming	Real time
[67, 68]	No	Distribution	No	Stochastic programming	Real time
[69]	No	Distribution	Yes	Bi-level iterative optimisation	Real time
[70]	No	Transmission	Yes	Dynamic programming	Real time

- Rigid Control Logic: Traditional EMS platforms rely on fixed rules and schedules that assume predictable conditions. They struggle to adapt quickly to the rapid fluctuations caused by renewable energy sources.
- Separation of Resilience: Resilience functions are often disconnected from daily operations, treating emergency responses as separate activities [65, 66]. This separation delays recovery because response actions are frequently manual rather than automatic.
- Scalability Issues: Centralised systems have difficulty managing the growing number of distributed energy resources. This leads to communication bottlenecks and slower decision-making.
- Lack of Interoperability: Many systems use vendor-specific software that cannot communicate with other platforms. This makes it difficult to integrate new digital technologies with older infrastructure.
- Underused Forecasting: Many EMS implementations do not fully utilise available weather and load predictions. Decisions are often based on past data rather than

proactive models.

- Focus on Economics over Resilience: Current systems typically prioritize cost reduction over system safety. This focus on short-term efficiency can weaken the grid's ability to withstand stress or emergencies.

2.4. Dynamic Inertia and Damping Control in Converter-Dominated Grids

The loss of physical inertia has introduced new challenges in maintaining frequency stability and damping electromechanical oscillations [71]. In response, research and development efforts have increasingly focused on replicating the stabilising functions of synchronous machines using converter control strategies [72]. These include synthetic or virtual inertia emulation, as well as advanced damping control mechanisms embedded within GFC topologies [73]. However, unlike synchronous machines, whose inertial and damping properties are intrinsic and passive, converter-based systems must actively measure, compute, and inject the appropriate responses in real time. This subsection provides a focused review of dynamic inertia and damping control in converter-dominated systems.

2.4.1. Role of Inertia and Damping in Power System Stability

Inertia and damping are two fundamental dynamic properties that govern the response of power systems to disturbances [74]. Inertia, provided naturally by the rotating mass of synchronous generators, resists sudden changes in frequency by absorbing or releasing kinetic energy during imbalances [75]. Damping, on the other hand, dissipates oscillatory energy over time, preventing sustained frequency or power oscillations that could otherwise destabilise the system [76]. Together, these parameters determine the speed, magnitude, and settling behaviour of the system’s frequency response following a disturbance.

In traditional power systems dominated by synchronous machines, the inertial response is immediate and passive. When a sudden loss of generation occurs, the kinetic energy stored in the rotating masses of generators is instantaneously converted into electrical energy, slowing the rate of frequency decline. This inertial buffer provides system operators with a short time window, typically a few seconds, to deploy active frequency control mechanisms such as primary frequency response (PFR) or automatic generation control (AGC) [77]. The damping contribution of the system, meanwhile, arises from both inherent machine characteristics and the droop-based control responses of generators, which collectively work to stabilise the

frequency trajectory and prevent undershoot or oscillatory behaviour.

However, in converter-dominated grids, this natural buffering mechanism is largely absent. Converter-based resources interface with the grid through power electronic converters that decouple the generation source from grid frequency. As a result, these systems do not contribute rotational inertia unless explicitly programmed to do so. Moreover, the loss of damping in converter-dominated systems poses an equally critical threat to stability. In synchronous machine-based systems, damping arises naturally from mechanical losses and electromechanical interactions, providing a self-regulating effect that suppresses inter-area oscillations and encourages system synchronisation. In contrast, converters are inherently fast-acting and lack these natural dissipative properties.

The absence of inertia and damping not only affects transient frequency response but also degrades small-signal stability [71]. Systems with insufficient damping are prone to poorly damped oscillatory modes, including inter-area and local modes, which can lead to power swings, voltage instability, and even loss of synchronism [78].

In summary, inertia and damping are not auxiliary features of power systems but fundamental stabilising forces that shape the dynamic behaviour of the grid. Their absence in converter-dominated environments necessitates the deliberate design of control strategies that can emulate or replace these properties in a coordinated and scalable manner. The next subsection explores how synthetic and virtual inertia techniques attempt to fulfil this stabilising role through control-based emulation of inertial behaviour in converter-based systems.

2.4.2. Synthetic and Virtual Inertia Techniques

Synthetic and virtual inertia techniques have emerged as prominent approaches, aiming to emulate the inertial response through programmed converter behaviour [79]. Though the terms “synthetic” and “virtual” inertia are often used interchangeably in the literature, they generally refer to two distinct implementation philosophies: synthetic inertia typically describes response derived from frequency measurement and feedforward control, while virtual inertia often refers to control schemes that more closely replicate the differential equations of synchronous machine dynamics, including both inertia and damping characteristics.

Synthetic inertia is commonly implemented in grid-following converter architectures, where the converter tracks the grid voltage and injects a power output modulated by the measured RoCoF [74]. In this configuration, the converter monitors frequency variations and responds

by adjusting active power injection proportionally to the frequency derivative. While this approach is relatively simple to implement and requires minimal computational overhead, it is inherently reactive and subject to measurement delays and filtering. These delays can significantly degrade response speed and accuracy, particularly during fast transients, and may result in overshoot or underdamped behaviour if not properly tuned.

In contrast, virtual inertia is more commonly associated with GFC control strategies. In virtual synchronous machine (VSM) implementations, for instance, the converter mimics the swing equation of a synchronous generator, allowing it to respond to disturbances with a power output that reflects both inertial and damping properties [80]. This is achieved by integrating virtual mass and damping coefficients into the control loop, effectively embedding a differential equation solver within the digital controller. The resulting behaviour produces a more natural and instantaneous inertial response, since it is not reliant on external frequency measurements but instead on internal control states that evolve according to the defined machine model.

Another variant of virtual inertia control involves droop-based GFCs augmented with virtual kinetic energy storage models. These controllers dynamically adjust their output power in response to deviations in internal frequency [81], emulating the exchange of kinetic energy that would occur in a rotating machine. These systems can operate in islanded or weak grid conditions and provide a stable frequency reference for other resources to synchronise to. However, they also introduce implementation challenges, including increased control complexity, sensitivity to parameter tuning, and the need for high-bandwidth current control loops to ensure accurate waveform synthesis under dynamic conditions.

An important consideration in both synthetic and virtual inertia schemes is energy availability [82]. In contrast to synchronous machines, which store kinetic energy mechanically, converter -based systems must draw on energy stored in capacitors, batteries, or other fast-response sources to deliver inertial power injection. This imposes constraints on the duration and magnitude of the emulated inertial response [83]. Battery Energy Storage System (BESS), in particular, are well-suited to this task, given their fast response times and controllable output, but they require careful energy management to ensure sufficient reserves are available for multiple events or prolonged disturbances. Control strategies must therefore coordinate inertial support with state-of-charge (SoC) constraints, often integrating scheduling or prioritisation logic to balance frequency support with other operational objectives such as peak shaving or load shifting [84].

The deployment of inertia emulation techniques also raises important questions regarding coordination and system-wide behaviour. Uncoordinated synthetic inertia responses from multiple devices can lead to instability or oscillatory interactions, particularly if devices operate with differing response delays or controller gains. This is especially problematic in systems with high penetrations of independently operated DERs, where lack of standardisation and communication can result in conflicting control actions. To mitigate these risks, recent research has focused on adaptive inertia emulation schemes, where the response characteristics of each converter are dynamically adjusted based on local grid conditions, system inertia estimation, or coordination signals from higher-level EMS or grid-forming controllers [85].

Despite these advances, synthetic and virtual inertia techniques are not a one-to-one replacement for physical inertia. The emulated response, while programmable, lacks the passive and instantaneous nature of mechanical inertia, and remains dependent on both control system integrity and communication infrastructure. Nevertheless, when properly designed and coordinated, these techniques provide a viable means of improving frequency stability and reducing RoCoF in low-inertia environments.

2.4.3. Damping Control Strategies for Grid-Forming Converters

In converter-dominated power systems, the displacement of synchronous machines eliminates the inherent electromechanical damping traditionally provided by rotor dynamics and Power System Stabilizers (PSS). This reduction in natural damping increases the system's susceptibility to inter-area oscillations, local plant modes, and high-frequency instabilities. Consequently, GFCs must move beyond simple voltage and frequency reference provision to actively inject damping into the grid. This requires sophisticated control architectures capable of emulating the stabilizing characteristics of synchronous machines while managing the fast-switching dynamics of power electronics. Table 2.4 categorizes the primary damping strategies currently employed in GFCs, detailing their operational mechanisms, inherent trade-offs, and the specific challenges associated with their implementation as discussed in the literature.

2.5. Co-Optimised EMS and Damping Control Frameworks

As power systems evolve into complex, converter-dominated, and highly distributed networks, the longstanding functional separation between EMS and dynamic stability control is becoming increasingly untenable. Traditionally, EMS platforms have been designed with a steady-state optimisation mindset prioritising economic dispatch, load forecasting, and resource

scheduling- while inertia and damping control have been addressed separately within the realm of primary and secondary frequency regulation.

Table 2-4: Classification and Assessment of Damping Control Strategies for GFCs

Control Strategy / Category	Mechanism & Operational Focus	Key Characteristics & Advantages	Limitations & Challenges	Reference(s)
Virtual Synchronous Machine (VSM)	**Inertia Emulation:** Embeds inertia and damping terms into the converter's frequency dynamics.	Mimics resistive torque damping; tuneable virtual damping coefficient allows for critical or underdamped responses.	Requires careful tuning to balance dynamic response with stability margins.	[86]
Droop Control: Frequency-Based	**Measurement-Driven:** Adjusts damping based on actual output frequency (via PLL) or nominal grid frequency.	Direct response to frequency deviations; essential for maintaining grid stability.	PLL dynamics can cause instability in weak grids; nominal-based methods may fail to zero damping if frequency deviates.	[87] [88] [89]
Droop Control: RoCoF-Based	**Derivative Control:** Uses RoCoF with filtering to control damping power.	Eliminates need for direct frequency measurement; preserves steady-state characteristics.	Fine-tuning filters to optimize performance without degrading inertial response is difficult.	[90] [91]
Droop Control: Active Power-Based	**Forward Damping:** Calculates damping based on the difference between input and output power.	Simplifies control by avoiding frequency measurements; maintains steady-state and inertial dynamics.	Proven inefficient when handling large system disturbances.	[92]
Droop Control: Voltage-Based	**PSS Analogue:** Introduces a voltage damping term at the output of the reactive power control loop.	Functions similarly to a traditional Power System Stabilizer (PSS).	Challenging to tune for a well-damped response while simultaneously maintaining voltage stability.	[93]
Advanced & Adaptive Control	**Dynamic Optimization:** Utilizes Linear-Quadratic Regulators (LQR) or Adaptive Virtual Impedance.	LQR balances response speed vs. control effort; Adaptive Impedance performs well in specific regions.	LQR is complex; Adaptive Impedance requires precise tuning and may adversely impact inertia outside designated regions.	[94, 95] [96, 97]
AI-Based Methods	**Intelligent Damping:** Uses AI (e.g., Intelligent Power Oscillation Damper - iPOD) to attenuate oscillations.	Superior capability in attenuating electromechanical inter-area power oscillations.	High computational complexity and resource requirements; requires robust hardware.	[98, 99] [100]

However, in modern grid environments characterised by low inertia, high renewable penetration, and rapidly shifting operating conditions, these domains are no longer orthogonal.

Their interdependence is now structural, dynamic, and temporal.

The core issue is that decisions made by the EMS such as dispatching energy storage, scheduling DERs, or islanding microgrids directly influence the grid's dynamic state, including its ability to withstand and recover from disturbances. Conversely, the performance of damping and inertial control mechanisms is heavily contingent on system operating points, network topology, and resource availability all of which are orchestrated by the EMS. For instance, an EMS that schedules minimal battery usage to preserve state-of-charge may inadvertently leave the system without adequate reserves for virtual inertia injection. Similarly, a decentralised EMS that fails to account for weak-grid conditions or inter-area oscillatory modes may dispatch DERs in ways that destabilise the network.

This emerging coupling between optimal control and dynamic stability necessitates a paradigm shift: from sequential or siloed control hierarchies to co-optimised architectures that embed dynamic awareness into energy management decisions and vice versa. In this context, damping and inertia support must be treated not merely as ancillary services but as integral constraints and objectives within EMS optimisation routines.

Recent research has begun to explore such integrative approaches. Studies such as [101] have proposed multi-objective optimisation frameworks where frequency nadir constraints are included in the EMS formulation, while others [102] have demonstrated the benefits of dynamically coordinating GFC damping parameters with EMS dispatch signals in microgrid environments. However, most of these efforts remain proof-of-concept or limited to centralised implementations that do not scale across hierarchical or distributed systems.

Furthermore, the challenge is not only technical but architectural. Traditional layered control paradigms where EMS operates at a supervisory level and dynamic control is relegated to device-level firmware are inadequate for future power systems where actions at all levels must be both temporally coordinated and dynamically aware. What is required is a hierarchical, modular control framework in which EMS functions are co-designed with dynamic stabilisation layers. Such a framework must allow for:

- **Bidirectional communication** between EMS and GFCs, enabling real-time feedback on system dynamics;
- **Predictive co-optimisation**, wherein damping and inertia constraints are explicitly modelled within EMS dispatch formulations;
- **Context-aware control**, where damping gains and inertia emulation parameters are

adjusted based on EMS-provided forecasts and operating scenarios;

This thesis proposes such a framework: a resilient, hierarchical EMS architecture that embeds co-optimised damping and inertia control mechanisms at its core.

2.6. Summary of Identified Gaps

The preceding sections have highlighted a series of interrelated challenges confronting modern power systems as they transition toward converter-dominated, distributed, and low-inertia architectures. These challenges span across the domains of system stability, energy management, and coordinated control, and collectively underscore the inadequacy of current paradigms when applied to future grid scenarios. This section summarises these insights into a coherent identification of key research gaps and positions the proposed work as a direct response to these deficiencies.

2.6.1. Identified Gaps in the State of the Art

- Fragmented Treatment of Energy Management and Dynamic Stability

A recurring theme in the literature is the conceptual and operational separation between EMS and dynamic stability control mechanisms. Traditional EMS frameworks are designed primarily for steady-state optimisation and economic dispatch, with limited or no integration of dynamic stability metrics such as inertia adequacy, damping sufficiency, or frequency response margins. Conversely, dynamic services such as synthetic inertia provision or damping control are often implemented as ad-hoc, device-level enhancements without coordination with system-wide scheduling or operational constraints.

- Static and Non-Adaptive Inertia and Damping Control Strategies

Most existing inertia and damping emulation techniques rely on fixed control parameters tuned offline based on nominal operating conditions. While effective in isolated or well-defined scenarios, these static strategies are ill-suited to systems with high variability in topology, loading, and converter penetration. The absence of adaptive, context-aware control frameworks limits the effectiveness of synthetic inertia and damping schemes under real-time disturbances, particularly in low-inertia or weak-grid conditions.

- Lack of Scalable Architectures for Multi-Layer Coordination

The literature reveals a critical architectural gap: there is no widely accepted framework that synthesises EMS decision-making with dynamic control in a scalable, hierarchical manner. While some centralised approaches have demonstrated technical feasibility, they are often

impractical for large-scale or distributed systems due to latency, communication overhead, and single points of failure. Conversely, decentralised control schemes lack the systemic visibility required for global optimisation and coordination across multiple voltage levels or control zones.

- Insufficient Integration of Stability Constraints into EMS Optimisation

Current EMS formulations including those applied to microgrids and islanded systems rarely incorporate stability-related constraints such as frequency nadir bounds, or RoCoF limits. This omission leads to dispatch schedules that may be optimal in an economic sense but dynamically infeasible or even destabilising. There is a pressing need to embed dynamic performance metrics directly into EMS optimisation problems.

- Limited Frameworks for Real-Time Co-Optimisation

While some recent works have advocated for co-optimisation of energy and stability services, these are generally limited to off-line scheduling. The absence of real-time capable, hierarchical co-optimisation frameworks restricts the industry's ability to respond to fast disturbances or reconfigure in response to system events in a dynamically efficient manner.

Chapter 3 Novel Hierarchical Energy Management System

This chapter introduces a novel EMS designed for coordinated control of multi-area power networks, with a particular focus on black start operations and load restoration. The proposed EMS features a unique hierarchical control framework that operates across both distribution and transmission network levels. A central component of the EMS is an optimised objective function that simultaneously enhances system inertia during black start conditions and improves the efficiency of load shedding strategies.

3.1. Proposed EMS Method

The proposed energy management system employs a multi-level control strategy across the power system. It utilises a hierarchical structure with Distribution Layer (DL)-EMS and Transmission Layer EMS (TL-EMS) to efficiently manage energy within the areas of the power system and maintain overall grid stability, particularly during normal scenarios and emergencies. It categorises areas based on their black start capabilities. Certain areas lack black start capability as they primarily use traditional steam-powered synchronous generators for energy production. These generators require the power grid to be operational to start up, limiting their ability to restart the system independently during a blackout. In contrast, areas with black start capability are characterised by their integration of distributed energy resources such as solar panels, batteries, and fuel cells. These distributed renewable energy resources can initiate the restoration of the grid independently, which enhances the overall resilience and sustainability of the power system. The dual layer of the proposed system, including both DL-EMS and TL-EMS under the hierarchical energy management system, significantly enhances operability and coordination. It ensures smooth communication and integrated control across all levels of the energy distribution network, addressing both normal operations and contingency scenarios effectively. The High-Level Controller (HLC) and Low-level Controller (LLC) engage in two-way communication, exchanging various types of information depending on different operational scenarios. Detailed explanations are provided in the following sections. The architecture and operational dynamics of this novel energy management system are depicted in Figure 3.1.

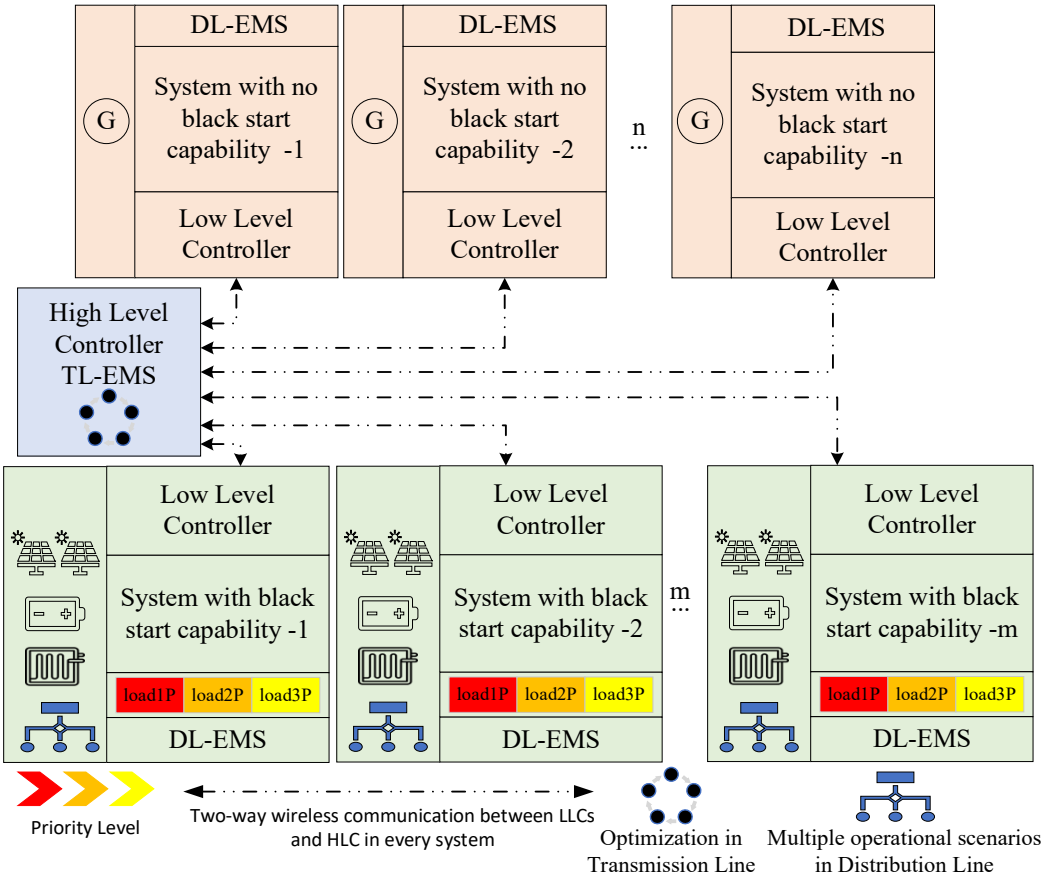

Figure 3-1 The proposed hierarchical energy management system including both DL -EMS and TL -EMS.

The network includes ‘n’ DL-EMSs with areas with no black start capability. Black Start Areas (BSA) integrates a hybrid configuration of energy sources, consisting of two parallel-connected solar panels, a battery, and a fuel cell. The use of two parallel-connected solar panels in the BSA configuration serves several purposes. It demonstrates the proposed management system’s capability to handle power aggregation from multiple distributed sources operating simultaneously, as commonly observed in microgrid systems. It also increases the available generation capacity and improves redundancy, enhancing supply reliability under variable operating conditions. These sources support three different loads to maintain the simplicity of the system while also representing hierarchical order by their criticality, where the first load represents the most critical load and the third load is the least critical one, as shown in Figure 3.1. A BSA operates under various scenarios including normal operation, black start operation, night operation, load shedding operation, and emergency operation to demonstrate the flexibility and resilience of the DL-EMS managed by the LLC. Conversely, there are ‘n’ areas with no black start capability (NBSA), which depend on only single conventional steam generators for energy supply to reflect a reliance on traditional power generation. An NBSA operates under only two scenarios, namely, normal operation and black start operation. For

simplicity, it is assumed that within this area, all loads are treated uniformly without differentiation based on criticality levels. During blackout scenarios, BSAs initially focus on restoring power to their critical loads. Once stability is achieved and if surplus power is available, these areas then look to support NBSAs in need. It is the role of the TL-EMS to determine the optimal allocation of this excess power from BSAs to NBSAs, ensuring that the distribution is carried out efficiently and effectively. This process takes into consideration the available reserve power within BSAs and the geographical proximity of NBSAs, underlining a novel proposal for power outage management through a hierarchical energy management system. The following subsection describes each area in detail.

3.1.1. Operational Framework of DL-EMS in Non-Black Start-Capable Areas (NBSAs)

As previously indicated, NBSAs are traditionally equipped with a single synchronous generator for simplicity. There are two primary operational scenarios for these areas, as shown in Figure 3.2, which are the black start support path and the normal operation path. Under normal operation, the generator power is adjusted to meet load demand power (loadPwr) using its governor system to achieve a balance between the load and generation, and system stability is maintained. However, the inherent challenge with synchronous generators is their dependency on an external electricity supply to start up during black start conditions.

This necessity is graphically represented in Figure 3.3, where the generation capability curve indicates that the generator must be supplied with a specific cranking power ($\mathrm{P_{Crank}}$) for a defined period, known as the cranking time (T_{crank}), to begin starting up. After this period, the generator has the capacity to produce power, but its output increases gradually in accordance with the ramp rate (R_r). Accordingly, loads within the NBSA are incrementally reintroduced to service as the generator progresses along the ramping curve, incrementally generating more power. This sequence continues until all the loads in the area have been reconnected. At this point, the generator is considered to have successfully started up and transitions to the normal operation path. Moreover, the LLC of NBSAs necessitates communication with the HLC at the transmission level. This involves transmitting not only the required power and cranking time but also two critical parameters: the minimum critical time (*Tgcmin*) and the maximum critical time (*Tgcmax*). These parameters indicate the timeframe within which the generator must be cranked. If an NBSA does not start within the corresponding maximum critical time, the unit will become unavailable after a considerable time delay. Furthermore, an NBSA with the minimum critical time is not ready to receive cranking power until after this time. Thus, the

HLC optimally allocates this cranking power from the nearest BSA within these timeframe constraints. Upon receiving the command about the availability of the cranking power from the HLC, the generator in the NBSA begins to crank and moves to operational status.

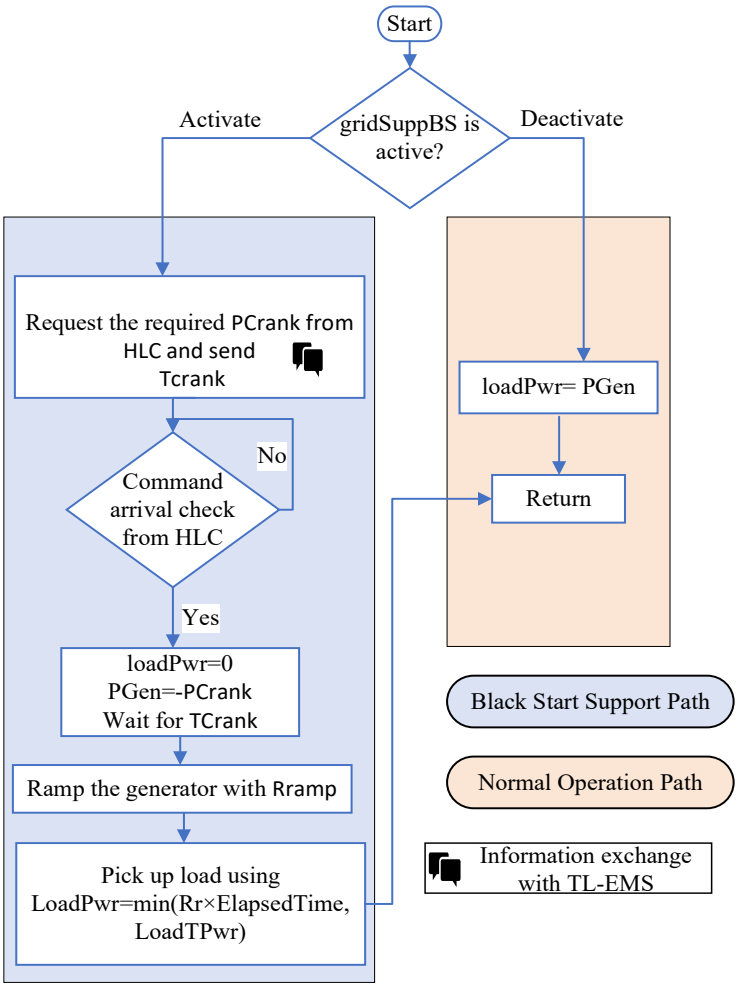

Figure 3-2 Flow chart of DL-EMS in non-black start-capable areas (NBSAs).

3.1.2. Operational Framework of DL-EMS in Black Start-Capable Areas (BSAs)

The DL-EMS within BSAs is structured to efficiently transition between several operational scenarios. These include normal operation, black start operation, night operation, load shedding operation, and emergency operation. The control strategies for the normal and black start operations are shown in Figure 3.4, while Figure 3.5 illustrates the remaining operational scenarios. This study assumes the first load (L_1) is the most critical load while the third load (L_3) is the least critical load, as shown in Figure 3.1 where the criticality levels are predefined based on customer-defined criteria and user preferences.

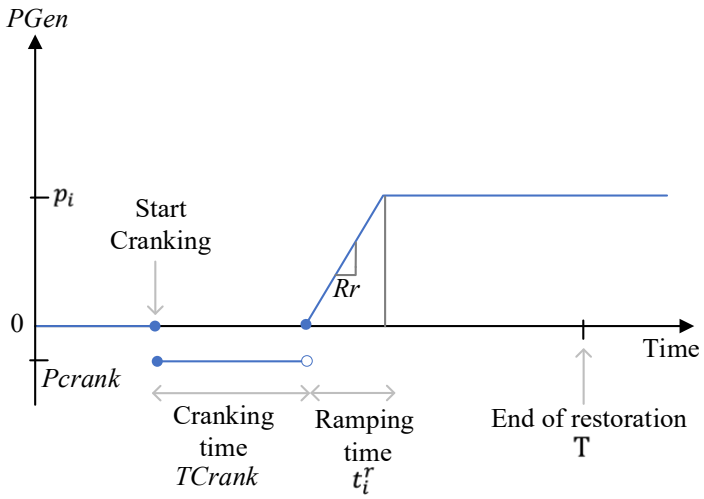

Figure 3-3 Generation capability curve.

Moreover, the DL-EMS within the BSAs demonstrates advanced intelligence by optimising load distribution based on predictive solar energy data for the next day and user preferences. It ensures operational satisfaction by aligning energy management systems with customer-chosen criteria, thereby integrating a customer-centric proposal within the technical framework of power distribution. This proposal reflects the demands of its end-users. Furthermore, forecasting solar irradiance for the next day enables the system to strategically adjust daily load management, thus safeguarding and optimising power availability for next-day operation. The following parts describe the different scenarios in detail.

A. Normal Operation Path

During normal operation, which occurs when solar power (*SPwr*) is available and load shedding (*LoadShed*) is deactivated by the operator first assesses whether the available solar power can meet the combined total demand of all the loads (loadTPower) in the system, i.e. L_1, L_2, and L_3. If so, these loads are powered to their full nominal power. The controller then evaluates any surplus power. If solar power exceeds demand and if the battery is not fully charged, the surplus is directed towards battery charging without exceeding the battery's maximum charging capacity. If the surplus exceeds the limit, the controller communicates with the HLC to determine if the excess can be dispatched into the grid. If not, the system is adjusted to operate the solar panels in voltage regulation mode to bypass maximum power point tracking to match the load nominal power (*LoadNPwr*) and charge the battery within its limits.

These decisions during real-time normal operation are based on actual measurements rather than predictions. The controller relies on real-time values of solar power output (SPwr), load

demand (loadTPower), battery state of charge (SoC), and available charging capacity to execute instantaneous power management actions. However, at the planning stage, the DL-EMS uses day-ahead solar irradiance forecasts to schedule load distribution and prepare operational strategies in advance. In summary, planning is prediction-based, whereas real-time control is measurement-driven.

B. Black Start Operation Path

In black start scenarios, the LLC within the BSA receives a command from the HLC indicating the need to assist neighbouring areas in initiating their startup processes. In response, the LLC maximises solar generation through precise MPPT and sends the current load conditions to the HLC. Therefore, depending on operational feasibility, the LLC provides feedback. If the current load states prevent support, the HLC might request the LLC to shed less critical loads to allocate more power for the black start effort where necessary. During BS mode, all available DERs (solar, battery, and fuel cell) are assessed collectively, and loads are restored sequentially based on their criticality, starting from L_1 (most critical), followed by L_2, and then L_3 (least critical), depending on the total combined power available from all sources. Subsequently, the LLC assesses the available reserve power from its array of sources: battery, solar, and fuel cell. It begins by evaluating the battery SoC and its current power status. If the battery is in a charging state, benefitting from surplus solar power, then the reserve power for solar is considered to be the excess energy directed towards unnecessary battery charging. Moreover, the battery reserve power is considered at its maximum discharge capability assuming it has not been fully discharged. Conversely, if the battery power status is discharged, there is no surplus solar power, resulting in the solar reserve being zero. The battery reserve power, in this scenario, is assessed based on its maximum charging capacity minus the power being utilised to compensate for load deficits. If the battery is discharging at or near its maximum capacity to support the loads, its available reserve for black start is zero.

The LLC then sends the calculated reserve powers from the solar array, battery, and fuel cell, alongside the battery SoC and the fuel cell available fuel percentage, to the HLC. This enables the HLC to estimate the duration these reserves can sustainably support the black start operation. Based on this analysis, the HLC solves an optimisation problem, detailed in subsequent sections, to determine the optimal power dispatch strategy. Operational instructions are then sent back to the LLC on how much power is effectively needed from this BSA to support neighbouring areas during the black start process, as shown in Figure 3.4.

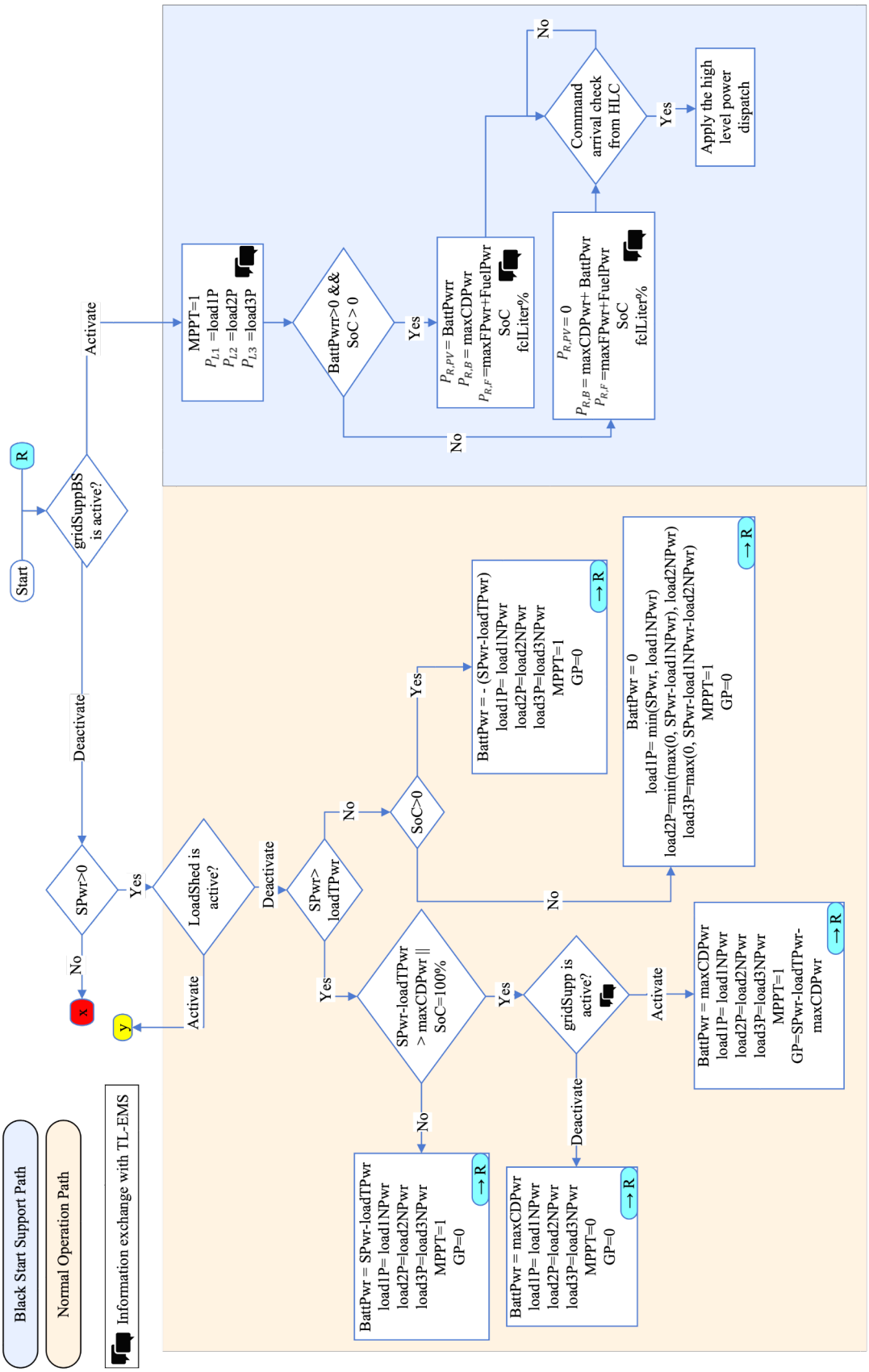

Figure 3-4 Flow chart of DL-EMS in black start-capable areas (BSAs): detailing the paths for normal operation and black start support.

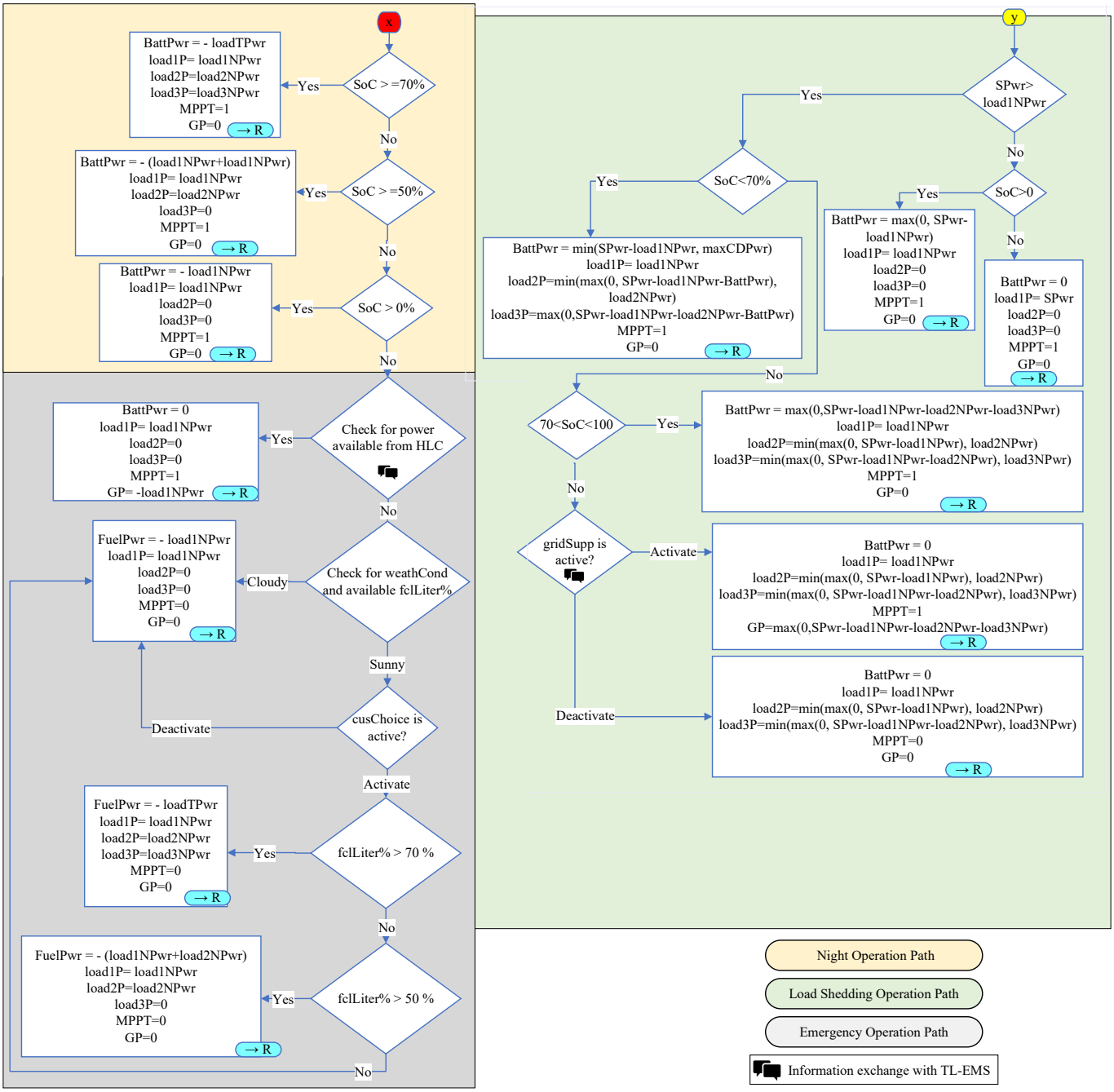

Figure 3-5 Flow chart of DL-EMS in black start-capable areas (BSAs): detailing the paths for night operation, load shedding, and emergency operation.

C. Load Shedding Path

During the load shedding path, priority is assigned to charging the battery rather than supplying power to the least critical loads. This approach differs from normal operations, where the preference is to support all loads before charging the battery, as shown in Figure 3.5. In this scenario, the LLC evaluates whether solar power can fully supply the most critical load (L_1).

If solar power is insufficient, the controller checks the battery SoC. If the battery is charged, both solar and battery power are utilised to supply L_1 to its full capacity. However, if the battery is fully discharged, L_1 operates below its normal capacity, relying solely on the available solar power.

In the case that solar generation is above the requirements of L_1, the LLC progresses to the next evaluation phase, examining the battery SoC to determine if it exceeds the threshold considered safe for night-time operations, assumed to be 70%. If the surplus power, after supporting L_1, exceeds the battery's maximum charging capacity, the controller allocates the remaining surplus to supply L_2 according to its criticality. Any additional power, after attending to L_2 and maximising battery charging, is then directed to L_3. Conversely, if the battery SoC is above the safe threshold, the system shifts its operational focus to powering L_2 and L_3, based on their respective criticality levels. If there is excess solar power after supporting these loads, the battery begins to charge with the surplus until it reaches its maximum SoC. Upon reaching this limit and if additional solar power remains, the LLC asks the HLC to determine the need for this extra power in the grid. If external support is not required, the LLC disables the MPPT and switches to voltage regulation mode, distributing the remaining solar power to the three loads as per their criticality. The load shedding operation path is determined based on the estimated irradiance for the day. If the irradiance is projected to be low, the load shedding mechanism is activated.

D. Night Operation Path

During night-time operation, when solar irradiance is unavailable and solar panels do not contribute power, the system relies entirely on battery reserves to supply the loads, which are prioritised according to their criticality. Specifically, if the battery SoC exceeds 70%, it possesses sufficient energy to simultaneously power all three loads at full capacity. However, in cases where the SoC falls between 50% and 70%, the battery's reduced capacity necessitates the disconnection of the least critical load (L_3) to ensure system stability, allowing only the two more critical loads (L_1 and L_2) to be powered fully. In scenarios where the SoC is between 10% and 50%, the available battery power is allocated exclusively to the most critical load (L_1), with the less critical loads (L_2 and L_3) being disconnected from the system. The choice of maintaining a minimum SoC threshold of 10%, rather than discharging the battery entirely to 0%, is made to avoid full discharge, thereby extending the battery lifespan. In cases where the SoC drops below 10% without the availability of solar power, the system moves to an

emergency operation mode, as shown in Figure 3.5, to manage the remaining energy resources effectively.

E. Emergency Operation Path

In the scenario where the DL-EMS within the BSA faces an emergency situation due to insufficient solar and battery resources to power the critical loads, the EMS asks for power from the HLC. The LLC inquires if available power can be supplied from adjacent areas through the grid to feed the most critical load (L_1). If the HLC manages to secure the required power, it is directed to support L_1. However, if the HLC is unable to obtain external power for L_1, the system then relies on its fuel cell as a backup energy source. The allocation of power from the fuel cell is prioritised based on load criticality and the available fuel percentage. Utilising its intelligent capabilities, the DL-EMS forecasts the next day's solar irradiance. If a cloudy day is expected and there is sufficient fuel, the system prioritises conserving fuel by supplying power only to L_1, preparing for limited solar generation for the next day. Conversely, if sunny conditions are expected, reducing the need to conserve fuel, the LLC consults with the customer to determine their preference regarding the distribution of power among the loads ($P_{\mathrm{L1}}, P_{\mathrm{L2}}, P_{\mathrm{L3}}$). This step enhances user satisfaction by allowing choices in power distribution based on available resources. In case the customer chooses to support all loads and the fuel cell capacity is above 70%, the system can power all loads fully. If the fuel capacity is between 50% and 70%, the system will power only the first two critical loads. However, if fuel levels drop below 50%, the decision is made to supply power solely to the most critical load. This approach not only incorporates intelligent system management and customer input into operational decisions but also ensures effective integration with the grid power (GP) supply capabilities.

3.1.3. Operational Framework of TL-EMS for High-Level Controller (HLC)

For the TL-EMS centralised under the HLC that interlinks all the LLCs from various areas, the HLC is pivotal in coordinating between them. It primarily functions in two scenarios: normal operations and black start operations. During normal operations, the HLC's role is to optimally manage power distribution, especially in emergency scenarios where a BSA requires additional power. In case a BSA needs supplementary power for its critical loads, the HLC surveys both BSAs and NBSAs for any available surplus power. If found, the HLC efficiently determines and dispatches the optimal allocation of this excess power to the BSA in need. Conversely, if

no additional power is available from surrounding areas to support the BSA during its emergency, the HLC communicates back to the BSA, as illustrated in Figure 3.6.

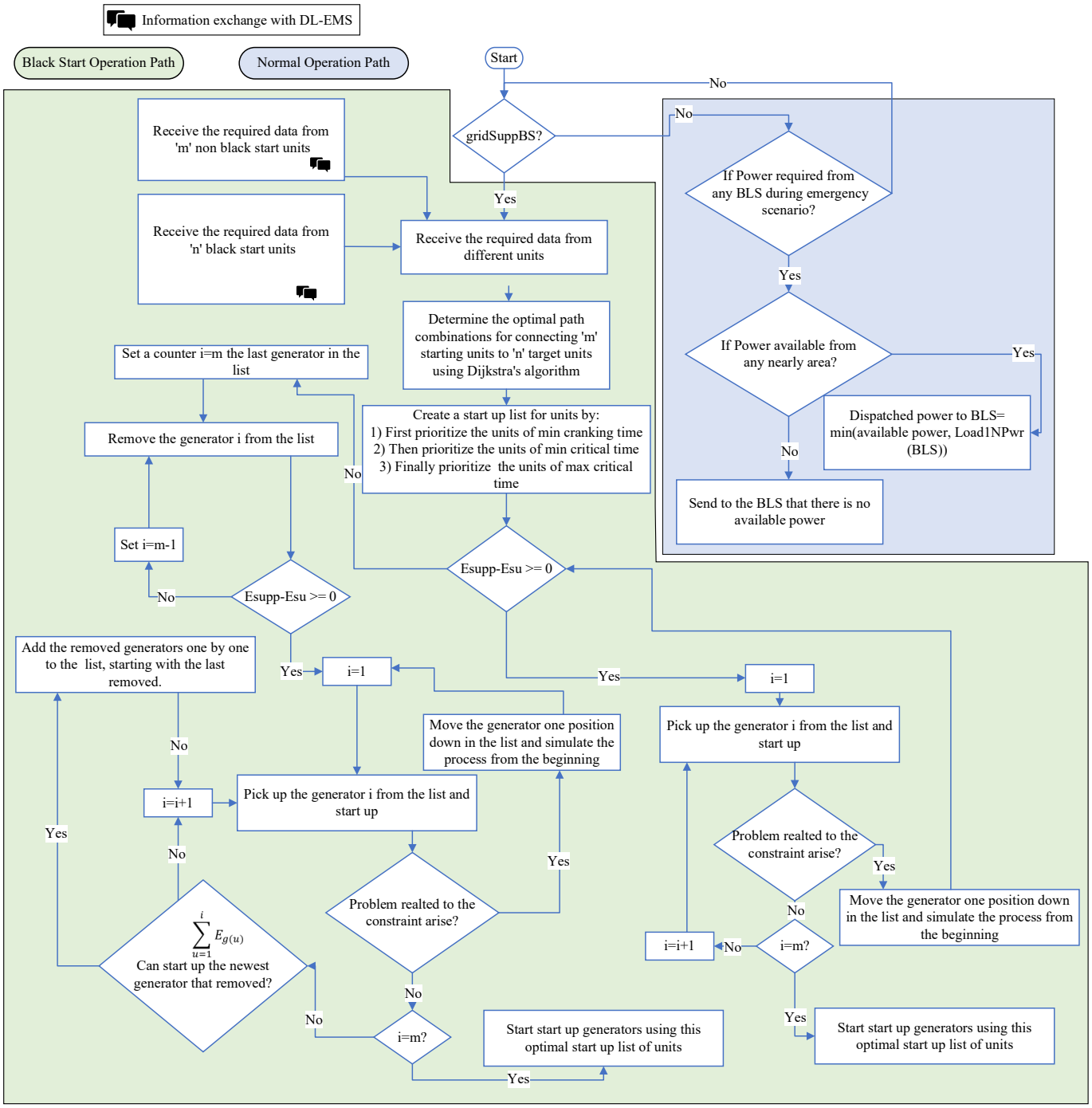

Figure 3-6 Flow chart of TL − EMS for the centralised HLC.

In black start scenarios, the HLC requests essential information from both the BSA and NBSA. From the BSA, the HLC gathers data on available reserve power sources, including solar, battery, and fuel cell, along with the status of less critical loads such as L_2 and L_3. This information is crucial because, in situations where available power is insufficient, the HLC may decide to disconnect these lower-priority loads to conserve power for black start

operations, albeit as a last option. Additionally, the HLC collects details on battery capacity, SoC, fuel capacity, fuel level, and estimated solar availability from the LLC intelligent forecasts. This comprehensive dataset aids the HLC in determining how long these resources can sustain the black start process to prioritise the resources that can reliably support operations until successful completion. From the NBSA, the HLC receives information about the cranking power needed for each generator, including cranking times and generator characteristics such as minimum and maximum critical times.

The HLC ensures that power supplying occurs within these critical timeframes to guarantee successful startup. Upon compiling this information, the HLC employs Dijkstra's algorithm to identify the optimal routing for connecting BSA and NBSA buses. In power system applications, Dijkstra's algorithm is widely used for network path optimisation and decision-making processes due to its ability to efficiently determine the shortest and most suitable path between interconnected buses. This algorithm considers network resistance to minimise total path losses during the black start to optimise energy distribution. The HLC then constructs a preliminary generator startup sequence, ranking generators based on their readiness and critical timing constraints. Generators with shorter cranking times are prioritised and are followed by those with urgent critical timing needs. If generators have similar cranking times, then preference is given to those with narrower windows between their minimum and maximum critical times to ensure no generator startup falls outside its critical window. Finally, the HLC calculates the energy reserves from the BSA and compares it with the energy demanded by the generators to start up in the NBSA using the following equations:

$$\mathrm{E}_{BSA} = \sum_{i=1}^{n} P_{R,PV} \times T_{sun} + SoC \times C_{batt} + \left(v_{fuel\%} \times C_{tank}\right) \times D_{fuel} \times \eta \qquad (3.1)$$

$$\mathrm{E}_{NBSA} = \sum_{j=1}^{m} P_{crank} \times T_{crank} \qquad (3.2)$$

where E_{BSA} and E_{NBSA} are the total reserved energy from the BSA and the total energy required by the generator to start up, respectively. $P_{R,PV}$ is the reserved power from solar energy, $P_{R,B}$ is the reserved power from the battery, $P_{R,F}$ is the reserved power from fuel cells, T_{sun} is the estimated time of irradiance lasting in hours, C_{batt} is the total capacity of the battery, $v_{fuel\%}$ is the percentage of fuel in the tank, C_{tank} is the total capacity of the tank in litres, D_{fuel} is the energy density of the fuel (kWh per litre), and η is the efficiency of the fuel generator.

In cases where energy reserves from the BSA exceed the demand of NBSA generators, the HLC sequentially addresses each generator to refine the startup list based on operational constraints. If a generator encounters optimisation issues, adjustments are made to the sequence to address any conflicts to ensure a smooth startup process for all generators. For example, if the scheduled startup time for a generator on the list falls before its minimum critical time, that generator is moved up one position in the sequence. Conversely, if a generator startup time exceeds its maximum critical time, it is shifted one position down in the list.

On the other hand, if BSA reserves are inadequate for all NBSA generators, the HLC removes some generators in the list from the bottom up to focus on generators with less strict operational constraints. This iterative process continues, then the HLC reintegrates generators in the list as more energy becomes available from already activated generators, always prioritising reintegrating those with stricter operational necessities. Ultimately, this detailed procedure ends in a refined, optimal startup sequence list. Following this optimised list, the HLC coordinates the startup of NBSA generators. This strategic approach guarantees that following the refined startup sequence will lead to the error-free activation of all targeted generators, effectively restoring power without issues. The subsequent part outlines the optimisation problem and constraints employed by the HLC in formulating the optimal startup sequence for generators.

3.2 Objective Function of the Optimisation Problem

This section presents a mathematical model for the TL-EMS operated by the HLC, aimed at improving grid restoration following a blackout. The model includes three objectives: enhancing system inertia to stabilise the grid during black starts, refining load shedding to ensure critical loads are maintained, and expanding the renewable energy use in grid restoration. The heart of this system is a novel multi-objective optimisation function, combining the following objectives: $\boldsymbol{I}_{\max}$ for system inertia, $\mathcal{L}_{\boldsymbol{shed}}$ for load prioritisation, and $\mathcal{R}_{\max}$ for renewable integration into a unified goal to enhance overall performance. This optimisation framework is defined as follows:

$$Objective\ Function = (I_{max} + \mathcal{L}_{shed} + \mathcal{R}_{max}) \tag{3.3}$$

In this model, $I_{\max}$ represents the objective to enhance the grid inertia by optimising the allocation of reserve power, mitigating frequency deviations. $\mathcal{L}_{shed}$ focuses on minimising power supply to non-essential loads, thereby ensuring priority is given to critical services during the restoration phase. $\mathcal{R}_{\max}$ emphasises increasing the grid's reliance on renewable

energy, integrating sustainable solutions into the black start process. The "+" symbol denotes a weighted-sum formulation used to combine the three objectives into a single unified objective function. Although $I_{\max}$ and $R_{\max}$ are inherently maximisation objectives, while L_{shed} is a minimisation objective, each term is reformulated in a consistent optimisation direction. In particular, L_{shed} is expressed in an inverse form such that its maximisation corresponds to a reduction in actual load shedding, effectively representing load retention. Accordingly, the aggregated objective is constructed such that its maximisation simultaneously promotes higher system inertia, reduces load shedding, and increases renewable energy integration. Each objective is defined by specific equations that illustrate their individual contributions to the grid recovery strategy. For instance, $I_{\max}$ is described as follows:

$$I_{\max}(D) = \max\left(\sum_{i=1}^{n} D_i \left(\sum_{j=1}^{k} RP_{ji} \times \frac{T_{ji}}{RT_{ji}}\right)\right) \tag{3.4}$$

In this model, the distribution factor (D_i) for each area i is determined based on the outcomes of Dijkstra's algorithm, which identifies the minimum-impedance paths between BSAs and the generators in NBSAs planned for startup. The model assigns weights to these paths, favouring shorter routes with higher values over longer ones. Consequently, the distribution factor enhances the prioritisation of areas closer in distance to the generators being activated, ensuring they receive power more promptly, which contributes to greater grid stability and reduced transmission losses. RP_{ji} is the reserve power from source j in area i. Furthermore, the term T_{ji} represents the estimated duration for which power sources like solar, fuel cells, and batteries can sustain their output, informed by the LLC predictions on solar availability and the current SoC and fuel level percentage. RT_{ji} denotes the response time for source j in area i; it reflects how quickly a power source can react to disturbances. Therefore, the inertia contribution increases as the reserve power and its availability duration increase and also increases as the source's response time shortens. Finally, the model combines the objectives of minimising unnecessary load shedding and enhancing the integration of renewable energy using Equation (3.5). This dual objective is captured in a unified minimisation function as follows:

$$\begin{aligned}\mathcal{L}_{shed}(\text{P}, \text{P}_{\text{L3}}, \text{P}_{\text{L2}}, \delta_1, \delta_2) + \mathcal{R}_{max}(\text{P}, \text{P}_{\text{L3}}, \text{P}_{\text{L2}}, \delta_1, \delta_2) \\ = \min(f_1(\text{P}) + \delta_1[f_2(\text{P}_{\text{L3}}) + M_1] + \delta_2[f_3(\text{P}_{\text{L2}}) + M_2])\end{aligned} \tag{3.5}$$

where, P is a vector that symbolises the collective available reserve power from diverse sources such as solar energy, batteries, and fuel cells.

The objective function also categorises loads into two categories, less critical and least critical, to optimise power distribution with the application of binary variables (δ_1, δ_2). This approach ensures customised energy allocation, focusing on the prioritisation of power delivery based on load criticality. For example, δ_1 disconnects the least critical loads and introduces its power in the black start operation in case the reserving power is not sufficient. δ_2 disconnects the less critical loads and introduces its power in the black start operation in case the reserving power and least critical power are not sufficient. Furthermore, the model introduces penalties (M_1 and M_2) to discourage the unnecessary shedding of loads and to promote the integration of renewable energy. M_1 and M_2 are large positive numbers with M_2 being substantially larger than M_1 to reflect load criticality, where M_1 corresponds to shedding the least critical load L_3 and M_2 corresponds to shedding the less critical load L_2, ensuring higher-priority loads are preserved unless absolutely necessary. In this formulation, $M_1$and M_2act as big-M penalty terms in a mixed-integer optimisation framework, enforcing load shedding only as a last resort when available reserve power from solar, battery, and fuel cell sources is insufficient. Moreover, the optimisation function in (3.5) incorporates functions (f_1, f_2 and f_3) designed to account for the power source location and cost. Specifically, (i) the distance-based penalty function $f_1(\mathbf{P})$ applies penalties for using power sources based on their distance to the NBS area and the type of source. This encourages the use of closer and more cost-effective energy sources.

$$f_1(\mathbf{P}) = \sum_{i=1}^{n} D_i \times \left(\sum_{j=1}^{k} c_{ji} \times \mathrm{p}_{ji} \right) \tag{3.6}$$

where, D_i is the distribution factor related to the proximity to the NBSA. c_{ji} is a penalty coefficient and varies based on the type of power source, with a preference for those that are less costly (e.g., solar panels are preferred over batteries, and batteries over fuel cells), ensuring an efficient and cost-effective power restoration process. c_{ji} represents the marginal running cost of dispatching power from source j in area i during the black start process, rather than the initial capital cost of the technology. The assumed cost hierarchy follows solar having the lowest marginal cost due to zero fuel consumption, followed by batteries, which incur degradation and cycling costs, and finally fuel cells, which have the highest marginal cost due

to hydrogen fuel usage. (ii) The load shedding cost functions $f_2(\mathbf{P})$ and $f_3(\mathbf{P})$ evaluate the financial impact of disconnecting the least L_3 and the less critical load L_2, respectively, aiming to minimise these actions unless absolutely necessary.

$$f_2(\mathbf{P}) = \sum_{i=1}^{n} D_i \times \mathbf{p}_{L3_i} \tag{3.7}$$

$$f_3(\mathbf{P}) = \sum_{i=1}^{n} D_i \times \mathbf{p}_{L2_i} \tag{3.8}$$

Constraints of the Optimisation Problem

The optimisation model integrates various constraints essential for maintaining grid stability and operational efficiency. These constrains can be summarised as follows:

1. Distribution factor constraint:

This ensures that the sum of distribution factors in (3.4) and (3.5) across all areas equals 1 ($\sum_{i=1}^{n} D_i = 1$). This constraint plays a pivotal role in determining the allocation of power based on the geographical proximity of areas to the black start zone by using Dijkstra's algorithm. Areas closer to the black start area are assigned higher distribution factors, reflecting their increased importance in power distribution.

2. Power balance constraint:

The power balance constraint is another critical component, formulated to ensure that the total power generated, including adjustments for non-critical and priority loads, matches the requirements for the black start operation (BS_p) of the chosen generator. This balance is vital for upholding system stability.

$$\sum_{i=1}^{n}\left(\sum_{j=1}^{k} \mathrm{p}_{ji}\right) + \delta_1 \sum_{i=1}^{n}\left(\mathbf{p}_{L3_i}\right) + \delta_2 \sum_{i=1}^{n}\left(\mathbf{p}_{L2_i}\right) = BS_p \tag{3.9}$$

3. Voltage and power transmission constraints:

This constraint regulates the voltage levels and power flow within the grid to ensure that the voltage at any bus remains within predefined limits and that the power transmitted along any

line does not exceed its capacity. These constraints prevent potential overloads and contribute to the reliable operation of the grid during restoration.

$$0.95 \leq u_b \leq 1.05 \; \forall b \in \mathrm{B} \tag{3.10}$$

$$\sqrt{(p_{bx}^t)^2 + (q_{bx}^t)^2} \leq u_{bx}^t S_{bx} \tag{3.11}$$

where u_b represents the voltage level at bus b and B is the total number of buses. p_{bx}^t and q_{bx}^t represent the active and reactive power flow, respectively, between buses b and x. u_{bx}^t denotes the voltage level between these buses at the specified time, and S_{bx} is the apparent power limit of the line connecting them.

4. Operational characteristics and capacities:

Furthermore, the model includes specific operational characteristics and capacities of energy storage and generation units, including batteries and fuel cells. Constraints related to these units ensure their output aligns with operational capabilities and state of charge, securing against overutilisation.

$$P_{B_i} \times T_{crank} \leq soc_i * C_{B_i} \quad \forall i \in chosen\ areas \tag{3.12}$$

$$P_{F_i} \times T_{crank} \leq C_{F_i} \quad \forall i \in chosen\ areas \tag{3.13}$$

$$T_{crank} \leq \mathrm{T}_{sun_i} \quad \forall i \in chosen\ areas \tag{3.14}$$

These constraints ensure that if batteries and fuel cells are selected to support the black start process, they will be capable of providing continuous support throughout the entire cranking period, thereby enhancing the system stability during black start operations. P_{B_i} represents the power output from the battery storage in area i, $T_{cranking}$ denotes the time for the cranking of non-black start units, SoC_i is the state of charge of the battery in area i, and C_{B_i} is the capacity of the battery in that area. Moreover, P_{F_i} is the power output from the fuel cells in area i, and C_{F_i} is the available capacity. Additionally, if the solar panel in area i is selected to power the black start, it must be verified that the power can be sustained throughout the entire cranking period. This is achieved by ensuring that the cranking time does not exceed the duration of sunlight availability, as predicted by the LLC of area i.

5. Operational Timing Constraints for Generator Startup

These constraints are pivotal in ensuring successful startup of all generators without black start capability such as steam turbines. For instance, operational timing constraints are formulated as follows:

$$t_{gstart} \leq T_{gcmax} \quad \forall g \in G \tag{3.15}$$

$$t_{gstart} \geq T_{gcmin} \quad \forall g \in G \tag{3.16}$$

These constraints ensure that NBSAs' start operations are performed within a specific timeframe: the start time (t_{gstart}) must not exceed the critical maximum time interval (T_{gcmax}), ensuring readiness for activation before becoming critical to the restoration process. Conversely, (t_{gstart}) should not precede the critical minimum time interval (T_{gcmin}), allowing for preparations that ensure a stable startup. These timing constraints are essential for the orderly and efficient re-energisation of NBSA generators, facilitating a coordinated restoration process.

3.3. Summary

This chapter presents a hierarchical EMS for coordinated control of multi-area power networks during normal and blackout conditions, with a focus on black start operations and load restoration. The proposed framework integrates DL-EMS and TL-EMS to improve grid resilience, stability, and restoration efficiency.

The system categorises areas into BSAs, which use renewable energy sources such as solar panels, batteries, and fuel cells, and NBSAs, which rely on conventional synchronous generators requiring external cranking power. Local LLCs manage operations within each area, while a centralised HLC coordinates power allocation and restoration across the network.

The EMS supports multiple operational modes, including normal operation, black start support, load shedding, night operation, and emergency operation. Load prioritisation is based on criticality levels to ensure essential loads remain supplied during power shortages. The HLC uses Dijkstra's algorithm and a multi-objective optimisation framework to determine optimal power routing and generator startup sequences while maximising system inertia, reducing load shedding, and increasing renewable energy utilisation.

The optimisation model incorporates operational constraints such as power balance, voltage limits, energy storage capacity, renewable availability, and generator startup timing requirements to ensure stable and reliable grid restoration. Overall, the proposed EMS offers an intelligent and resilient solution for black start management in renewable-integrated power systems.

Chapter 4 System Modelling and Simulation Validation

In this chapter, a comprehensive and detailed presentation of the proposed modelling methodology is provided. The theoretical foundations of the model are derived and explained step by step to ensure clarity and reproducibility. All system parameters used in the model are presented in clearly labelled tables for ease of reference. Following the methodological framework, simulation results are presented to validate the effectiveness and robustness of the proposed approach.

4.1 Model Derivation and Parameter Definition

The detailed converter control architecture, including current control loops, voltage regulation, phase-locked loop (PLL) synchronisation, and pulse-width modulation (PWM) strategies, is presented in Sections 4.2, 4.3, and 4.4 for the PV, battery, and fuel cell converters, respectively. These sections also include comprehensive converter control block diagrams or schematics illustrating the complete control structure, rather than focusing solely on mathematical formulations, to provide a clearer representation of the system-level implementation.

The model comprises a distributed energy system featuring two PV panels connected in parallel, a single battery storage unit, one fuel cell, and three distinct loads with prioritised demand levels. The PV arrays are interfaced with the system via a three-level IGBT bridge converter, which facilitates the conversion of DC power to AC power the output of the converter is then stepped up through a transformer from the converter-side low-voltage AC level to the 11 kV medium-voltage AC bus to meet grid transmission voltage requirements. The converter control incorporates a Maximum Power Point Tracking (MPPT) algorithm, which continuously adjusts the operating point of the PV panels to ensure they operate at their maximum power output despite varying irradiance and temperature conditions. The MPPT algorithm adjusts the DC-side operating voltage of the PV array to extract maximum power. It does not control the grid-side AC voltage, which is regulated separately by the converter's current control loop operating in the dq reference frame. This optimisation maximises energy extraction and overall system efficiency. The three loads connected to the system have different priority rankings, enabling hierarchical load management, including selective load shedding

during contingencies. Both the battery and the fuel cell are connected through identical converter topologies. The battery's converter can operate in either grid-forming or grid-following mode depending on the system strength and operational conditions, while the fuel cell converter operates exclusively in grid-following mode. The battery has fast response dynamics in the millisecond range and can quickly regulate voltage and frequency, making it suitable for grid-forming operation when the grid is weak or during islanding such as black start scenarios. The fuel cell has inherently slower electrochemical dynamics with response times in the order of seconds, which makes it unsuitable for grid-forming duty where fast voltage and frequency regulation is required. Therefore the fuel cell operates only in grid-following mode, relying on the grid voltage reference established either by the main grid or by the battery's grid-forming converter. The EMS algorithm used for coordinating the power dispatch, load prioritisation, and operational mode transitions across the distributed energy resources is detailed in Appendix A, and all system parameters and component specifications are summarised in the Table 4.1.

Table 4-1 System Parameters

Solar PV		
	Parallel strings	220
	Series- connected modules per string	11
	Module	SunPower SPR-415E-WHT-D
	Maximum Power	414.801 (W)
Battery		
	Operating Volt	11165 (RMS)
	Max Charging Power	2100 (kW)
	Capacity	2220 (kWh)
Fuel Cell		
	Operating Volt	11165 (RMS)
	Max Charging Power	2100 (kW)
	Capacity	2220 (kWh)

4.2 Modelling of the PV System with Converter Control for AC Coupling

This section presents a comprehensive mathematical and control model of the PV source and its associated three-phase converter system configured for AC coupling. The modelling approach is grounded in physical principles and control theory to ensure fidelity and reproducibility.

4.2.1 PV Array Modelling

The PV array is modelled based on an equivalent single-diode model, which captures the nonlinear I–V characteristics of a solar module under varying irradiance and temperature conditions. The array under study comprises 220 parallel strings, each consisting of 11 SunPower SPR-415E-WHT-D modules connected in series. Each module comprises 128 cells, yielding a total of 1,408 cells per string.

The output current of the PV array, I_{PV}, is given by:

$$I_{PV} = I_L - I_0(e^{\frac{q(V_{PV}+I_{PV}R_s)}{nkT}} - 1) - \frac{V_{PV} + I_{PV}R_s}{R_{sh}} \quad (4.1)$$

where I_{PV} is the output current of the array (A), V_{PV} is the array terminal voltage (V), I_L is the light-generated current (A), I_0 is the diode saturation current (A), q is the elementary charge (1.602×10^{-19} C), n is the diode ideality factor, k is Boltzmann's constant (1.3806×10^{-23} J/K), T is the cell temperature in Kelvin, R_s is the series resistance (Ω), R_{sh} is the shunt resistance (Ω). The model accounts for temperature and irradiance dependence through the variation in I_L and I_0. Temperature coefficients of voltage and current are incorporated to adjust V_{oc} and I_{sc} under varying environmental conditions.

The total number of modules is $220 \times 11 = 2{,}420$, providing a theoretical peak power of approximately $2{,}420 \times 414.801$ W $= 1.004$ MW. The PV output is filtered and measured through voltage and current filters to reduce high-frequency switching noise, ensuring accurate control feedback.

4.2.2 Converter Control Architecture

The converter control system is designed for grid-connected operation using an AC-coupled topology. It comprises several hierarchical control layers, including Maximum Power Point Tracking (MPPT), DC voltage regulation, current control in the synchronous reference frame, and Pulse Width Modulation (PWM) for switching signal generation.

Table 4-2 PV Module Parameters (SunPower SPR-415E-WHT-D)

Parameter	Value	Unit
V_{oc}	85.3	V
I_{sc}	6.09	A
V_{mp}	72.9	V
I_{mp}	5.69	A
I_L	6.0978	A
I_0	7.1698×10^{-13}	A
n	0.87223	–
R_s	0.53711	Ω
R_{sh}	419.7781	Ω
Temp. Coeff. of V_{oc}	–0.229	%/°C
Temp. Coeff. of I_{sc}	0.0307	%/°C

A. Maximum Power Point Tracking (MPPT)

The MPPT is implemented using the Perturb and Observe (P&O) algorithm. It tracks the maximum power point by perturbing the reference voltage and observing the change in power. The algorithm updates the reference voltage V_{ref} as:

$$V_{ref}(k+1) = V_{ref}(k) + \Delta V_{MPPT}(k) \tag{4.2}$$

Where ΔV_{MPPT} is the output increment set by the MPPT controller, and the update direction depends on the sign of ΔP.

B. DC-Link Voltage Regulation

The DC-link voltage regulator ensures a constant DC bus voltage V_{dc} by adjusting the d-axis current reference i_d^{ref}. The control law is given by:

$$i_d^{ref} = K_p^{dc}(e_{dc}) + K_i^{dc}\int e_{dc}\, dt \tag{4.3}$$

where $e_{dc} = V_{dc}^{ref} - V_{dc}^{meas}$

Where: K_p^{dc}, K_i^{dc} are the proportional and integral gains, V_{dc}^{ref} is the reference DC voltage, V_{dc}^{meas} is the measured DC voltage. The error is normalised by the nominal voltage V_{nom_dc} before PI control.

C. Current Control (d-q Frame)

The converter operates in the synchronous rotating $d-q$-frame using a Phase-Locked Loop (PLL) for angle detection. The current control law applies PI regulation with feedforward of grid voltage and RL terms:

$$v_d^{ref} = v_d + Ri_d + L\frac{di_d}{dt} + K_p(i_d^{ref} - i_d) + K_i\int (i_d^{ref} - i_d)dt \quad (4.4.)$$

$$v_q^{ref} = v_q + Ri_q + L\frac{di_q}{dt} + K_p\left(i_q^{ref} - i_q\right) + K_i\int \left(i_q^{ref} - i_q\right)dt \quad (4.5)$$

Where: v_d^{ref}, v_q^{ref} are the converter voltage references, i_d, i_q are the measured currents, R, L are the filter resistance and inductance, K_p, K_i are the PI controller gains.

D. PWM and Modulation

The PWM generator uses a symmetric three-level carrier-based modulation scheme. The reference voltage signals U_{abc}^{ref} are derived from the dq-frame voltages and transformed back to the stationary frame. The PWM scheme compares U_{abc}^{ref} with two shifted triangular carriers to generate switching signals for the three-level converter. The carrier frequency f_c and sampling time T_s are key parameters influencing the resolution and harmonic performance of the converter These parameters must be selected based on switching device capabilities and system filtering requirements.

4.2.3 Critical Modelling Considerations

Several modelling choices and assumptions are made to balance model fidelity and computational efficiency. The PV model uses a single-diode equivalent circuit which, while simplified, captures the essential I–V nonlinearity and thermal effects with acceptable accuracy. The converter control is modelled in discrete-time to match the digital implementation in embedded controllers, and the PI controllers are tuned based on system dynamics and bandwidth targets. It is acknowledged that the model assumes ideal switching without losses, and the thermal dynamics of the converter are not modelled. These are acceptable for control design and grid-interaction studies.

4.3 Battery Energy Storage System and Converter Control for Grid-Following AC Coupling

BESS are increasingly integral in modern power networks due to their flexibility in managing energy flows, providing ancillary services, and enhancing system resilience. In this study, a lithium-ion battery model is employed using MATLAB/Simulink's generic dynamic battery block. The model represents the electrochemical behaviour of rechargeable lithium-based batteries and is integrated with an AC-coupled converter operating in a grid-following mode. The BESS is designed to provide active power support while ensuring zero reactive power exchange at the PCC.

4.3.1 Lithium-Ion Battery Dynamic Model

The battery model is based on a nonlinear voltage source controlled by extracted capacity and current dynamics. The model assumes constant internal resistance and symmetrical behavior during charge and discharge, with no memory effect or self-discharge under ideal conditions. The internal resistance is assumed constant during both charge and discharge phases, and no Peukert effect is considered; thus, battery capacity is independent of current magnitude.
The battery voltage V_{batt} is expressed as:

$$V_{\text{batt}} = E_{\text{batt}} - R_{\text{int}} \cdot I_{\text{batt}} \tag{4.6}$$

Where: $V_{\text{batt}}$is the terminal voltage of the battery (V), E_{batt} is the nonlinear open-circuit voltage (V), R_{int} is the internal resistance (Ω), I_{batt} is the battery current (A), positive during discharge. The nonlinear voltage $E_{\text{batt}}$is governed by different expressions depending on the mode, charge or discharge, determined by the sign of the low-pass filtered current i^*. For lithium-ion batteries, the discharge and charge models are given respectively by:
Discharge Model ($i^* > 0$):

$$f_1(it, i^*, i) = E_0 - K \cdot \frac{Q}{Q - it} \cdot i^* - K \cdot \frac{Q}{Q - it} \cdot it + A \cdot e^{-B \cdot it} \tag{4.7}$$

Charge Model **($i^* < 0$):**

$$f_2(it, i^*, i) = E_0 - K \cdot \frac{Q}{it + 0.1 \cdot Q} \cdot i^* - K \cdot \frac{Q}{Q - it} \cdot it + A \cdot e^{-B \cdot it} \tag{4.8}$$

Where: f_1 represents the open-circuit voltage E_batt during discharge and f_2 represents the open-circuit voltage E_batt during charging, such that $E_{batt} = f_1(it, i^*, i)$ when i* > 0 for discharge and $E_{batt} = f_2(it, i^*, i)$ when i* < 0 for charge. The 0.1 factor is a numerical correction coefficient used in the charging polarisation term to avoid singularity and to improve model accuracy during the charging cycle.

$E_0$is the battery's constant voltage (V), K is the polarization constant (V/Ah), Q is the maximum battery capacity (Ah), it is the extracted capacity (Ah), i^* is the low-frequency battery current (A), i is the instantaneous battery current (A), A is the exponential zone voltage (V), B is the exponential capacity constant (Ah^{-1}).

The model includes a first-order low-pass filter to obtain i^*, which provides a smoothed representation of the current for energy dynamics estimation. The filter dynamics are:

$$i^*(s) = \frac{A}{1 + B \cdot i(t) \cdot s} \tag{4.9}$$

This structure captures transient dynamics typical of lithium-ion batteries, which have fast response times in the range of milliseconds to a few seconds, depending on the internal chemistry and control hardware.

Table 4-3 Battery System Parameters

Parameter	Value	Unit
Operating Voltage	11,165	V (RMS)
Initial State of Charge (SoC)	90	%
Max Charging Power	2,100	kW
Energy Capacity	2,220	kWh
Efficiency	100	% (Ideal)

4.3.2 Converter Control for AC-Coupled Battery System

The converter interfacing the BESS with the grid can operate in two principles control modes: Grid-Following (GFL) and Grid-Forming (GFM). Each mode offers distinct dynamic behaviours and is selected based on the strength of the grid at the PCC, the system stability requirements, and the hierarchical control objectives of the microgrid or distribution network.

A. Grid-Following (GFL) Control Mode

In the grid-following mode, the converter synchronises to the grid voltage using a PLL and injects specified active and reactive power according to power references. This mode is suitable for strong grids where voltage and frequency are well-regulated by a dominant utility source.

The converter measures the grid voltage and uses Park transformation to convert it to the rotating dq-frame aligned with the grid voltage vector. The control objective is to regulate:

$$P = V_d \cdot i_d, Q = -V_d \cdot i_q \tag{4.10}$$

To meet the objectives of:

Injecting a specified active power P_{ref} (for charging or discharging the battery),

- Maintaining reactive power exchange at zero: $Q = 0$.

Using the dq-aligned voltage, the reference currents are:

$$i_d^{ref} = \frac{2}{3} \cdot \frac{P_{ref}}{V_d} \tag{4.11}$$

$$i_q^{ref} = 0 \tag{4.12}$$

The measured currents $i_d$and $i_q$are regulated using PI controllers. The control law incorporates feedforward terms to improve dynamic response:

$$v_d^{ref} = v_d + R \cdot i_d + L \cdot \frac{di_d}{dt} + K_{p,d}\left(i_d^{ref} - i_d\right) + K_{i,d}\int \left(i_d^{ref} - i_d\right)dt \tag{4.13}$$

$$v_q^{ref} = v_q + R \cdot i_q + L \cdot \frac{di_q}{dt} + K_{p,q}(i_q^{ref} - i_q) + K_{i,q}\int (i_q^{ref} - i_q)dt \tag{4.14}$$

Where: R, L are the filter resistance and inductance (Ω, H), v_d^{ref}, v_q^{ref} are the reference converter voltages in the dq frame (V), $K_{p,d}$, $K_{i,d}$, $K_{p,q}$, $K_{i,q}$are PI gains.

B. Grid-Forming (GFM) Control Mode

In the grid-forming mode, the converter no longer relies on an external voltage source (i.e., no PLL is used). Instead, it acts as a voltage source and establishes the local voltage waveform (magnitude and frequency), effectively forming a "virtual generator." This mode is essential in weak or islanded grids where voltage and frequency regulation must be provided locally.

Grid-forming converter s are typically controlled using either:

- Droop Control (simplified, power–frequency and power–voltage),
- Virtual Synchronous Machine (VSM) or
- Synchronous Reference Frame Voltage Control

Here, the droop-based GFM control is focused, which is widely used in microgrid applications.

i. Frequency–Active Power Droop Control

The converter frequency ω is adjusted based on the active power deviation from the reference:

$$\omega = \omega_0 - k_p\left(P - P_{ref}\right) \tag{4.15}$$

Where ω_0 is the nominal angular frequency (rad/s), P is the measured active power, P_{ref} is the active power reference, $k_p$is the active power droop coefficient (rad/s/W).

ii. Voltage–Reactive Power Droop Control

The voltage magnitude is adjusted according to reactive power:

$$V = V_0 - k_q(Q - Q_{ref}) \tag{4.16}$$

Where: $V_0$is the nominal voltage magnitude, Q is the measured reactive power, $Q_{ref}$is the reactive power reference (often 0), $k_q$is the reactive power droop coefficient (V/VAR).

In this mode, the converter behaves like a controlled voltage source and can support frequency and voltage in islanded operation or under weak grid conditions.

C. Control Mode Selection Based on Grid Strength

The choice between GFL and GFM control depends on the Short-Circuit Ratio (SCR), a standard metric for grid strength at the PCC:

$$\mathrm{SCR} = \frac{S_{\mathrm{SC}}}{S_{\mathrm{inv}}} \tag{4.17}$$

Where: $S_{\mathrm{SC}}$is the grid short-circuit power at the PCC, $S_{\mathrm{inv}}$is the rated apparent power of the converter. If SCR > 3: The grid is considered strong, and GFL control is preferred. If SCR < 3: The grid is weak, and GFM control enhances stability and voltage support[103].

Table 4-4 Summary of Control Modes

Feature	Grid-Following	Grid-Forming
Synchronization	PLL-based	Internal oscillator (droop/VSM)
Voltage Control	Follows grid voltage	Sets voltage magnitude
Frequency Control	Follows grid frequency	Regulates frequency
Suitable for	Strong grid (SCR > 3)	Weak grid or islanding (SCR < 3)
Reactive Power Control	$Q = 0$or reference	Droop-based $V - Q$

D. PWM and Synchronization

The control outputs are converted to three-phase signals and used to modulate the converter using a three-level PWM generator. The carrier-based PWM technique ensures switching accuracy and harmonic performance. Given the synchronization with the grid PLL, the converter operates in a grid-following mode, aligning its frequency and phase with the grid.

4.3.3 Limitations and Assumptions

The lithium-ion battery model, while widely applicable, includes several simplifying assumptions:

- The internal resistance $R_{\mathrm{int}}$is constant and does not vary with temperature or SoC.
- The discharging and charging characteristics are assumed symmetric.
- No Peukert effect is modelled; hence, current amplitude does not influence capacity.
- Self-discharge is neglected unless explicitly modelled via a parallel resistor.
- No thermal model or aging degradation is included.

Despite these limitations, the model captures the key dynamics for power flow and grid-integration studies with sufficient accuracy.

4.4 Fuel Cell System Modelling for Power Flow Analysis

Fuel cells are a promising technology for sustainable energy generation, offering high efficiency and low emissions. However, their detailed modelling, particularly when considering thermal, chemical, and fluidic subsystems, can be highly complex and computationally intensive. In the context of this study, which focuses on high-level power flow dynamics and control interactions within an AC-coupled multi-source energy system, such detailed modelling is not required.

4.4.1 Modelling Approach and Justification

The primary objective of this work is to evaluate the dynamic power exchange between DERs and the grid, with particular attention to control strategies, active/reactive power regulation, and converter coordination. Therefore, the fuel cell is modelled using a simplified dynamic equivalent that captures the key electrical behaviour relevant to power flow without including the detailed thermodynamic subsystems such as cooling, gas reforming, or humidity control.

To this end, the fuel cell is modelled similarly to the previously described lithium-ion battery system, using a controlled voltage source in series with an internal resistance and a first-order dynamic response. However, to reflect the inherently slower electrochemical and mechanical dynamics of fuel cells, the response time of the fuel cell model is set to be slower than that of the battery system. This adjustment captures the key inertial characteristics of fuel cell systems while maintaining model simplicity.

4.4.2 Simplified Dynamic Fuel Cell Model

The simplified fuel cell model is structured as a voltage source with dynamic behaviour governed by a low-pass filter and internal resistance. The output voltage of the fuel cell stack $V_{\mathrm{fc}}$is given by:

$$V_{\mathrm{fc}}(t) = E_{\mathrm{fc}}(t) - R_{\mathrm{int,fc}} \cdot I_{\mathrm{fc}}(t) \tag{4.18}$$

Where: $V_{\mathrm{fc}}(t)$is the terminal voltage of the fuel cell stack (V), $E_{\mathrm{fc}}(t)$is the open-circuit voltage, dynamically filtered (V), $R_{\mathrm{int,fc}}$is the internal resistance (Ω), $I_{\mathrm{fc}}(t)$is the current drawn from the fuel cell (A).

The open-circuit voltage $E_{\mathrm{fc}}(t)$is calculated using a first-order low-pass filter to emulate the slow response of gas flow, reaction kinetics, and pressure regulation:

$$\tau_{\mathrm{fc}} \cdot \frac{dE_{\mathrm{fc}}}{dt} + E_{\mathrm{fc}} = E_{\mathrm{ref}}(t) \tag{4.19}$$

Where: $\tau_{\mathrm{fc}}$is the fuel cell time constant (s), $E_{\mathrm{ref}}(t)$is the reference voltage based on desired power output. In this study, $\tau_{\mathrm{fc}}$is set to be approximately 10 times larger than the battery's time constant τ_{batt}, i.e.,

$$\tau_{\mathrm{fc}} = 10 \cdot \tau_{\mathrm{batt}} \tag{4.20}$$

This ensures that the fuel cell model captures the appropriate response delay and inertial characteristics without excessive complexity.

4.4.3 Integration with Power Flow Control

The fuel cell system is interfaced with the grid via a three-phase converter operating in grid-following mode, identical in structure to that described for the battery system. The converter is responsible for regulating the active power output of the fuel cell in accordance with a reference $P_{\mathrm{fc,ref}}$, and maintaining zero reactive power injection at the point of common coupling (PCC):

$$i_{d,\mathrm{fc}}^{ref} = \frac{2}{3} \cdot \frac{P_{\mathrm{fc,ref}}}{V_d}, i_{q,\mathrm{fc}}^{ref} = 0 \tag{4.21}$$

The reference active power $P_{\mathrm{fc,ref}}$ is typically determined by higher-level energy management systems (EMS) based on load demand, state of charge (SoC) of the battery, and operational priorities.

4.4.4 Assumptions and Limitations

The simplified fuel cell model is developed under the following assumptions:

- Thermal dynamics, cooling systems, hydrogen fuel flow, and humidity control are not explicitly modelled.

- The internal resistance is assumed constant over the operational range.
- The model assumes ideal fuel availability and no fuel starvation effects.
- The dynamic response is limited to electrical transients impacting power flow.

These assumptions are acceptable for high-level grid interaction studies, where the focus is on active/reactive power control, converter coordination, and system-level dynamics. For studies requiring fuel utilization efficiency, thermal management, or degradation analysis, a more detailed electrochemical and thermodynamic model would be required.

4.5 Load and Coupling System

In modern power systems, the classification and management of loads based on their criticality plays a pivotal role in ensuring operational reliability, especially under constrained generation scenarios or during grid disturbances. In this study, the load system is designed to reflect a realistic distribution of demand with three levels of criticality: high-priority, medium-priority, and low-priority loads. These loads are dynamically controlled and receive their power demand setpoints from a centralised EMS.

4.5.1 Load Classification and Control

The total load is segmented into three priority levels:

- High-Priority Loads: These are essential loads that must remain connected under all operating conditions (e.g., critical infrastructure, control systems). They have the highest operational priority and are first to be supplied.
- Medium-Priority Loads: These loads are important but can tolerate temporary curtailment during resource constraints or emergency conditions.
- Low-Priority Loads: These are non-critical loads that are the first to be shed in response to energy scarcity or grid instability.

The EMS continuously monitors system conditions and allocates power to the loads based on availability from distributed energy resources (DERs) including the PV, battery, and fuel cell systems. Load prioritisation enables demand-side flexibility, improving system resilience and optimising resource utilisation.

Each load level is modelled as a dynamic load block in MATLAB/Simulink, which can vary its power demand over time. The EMS interfaces with these blocks through signal connections that provide continuous active power setpoints $P_{load,ref}$ for each segment at every simulation time step. The load models consume active power as per the reference profile and are also capable of receiving reactive power commands if extended to power factor control operation.

4.5.2 Electrical Coupling and Voltage Interface

All load segments, as well as the converter s interfacing the DERs, are coupled at the 11 kV medium-voltage level, which represents a typical distribution grid voltage. The electrical interconnection architecture includes the following components:

- Step-Up Transformers:
  Each converter (PV, Battery, and Fuel Cell) operates at a lower DC-link or LV AC voltage level and is connected to the 11 kV grid bus through dedicated step-up transformers. These transformers ensure appropriate voltage scaling and galvanic isolation.

- Point of Common Coupling :
  The 11 kV bus serves as the PCC where all DERs and dynamic loads are connected. This facilitates centralized control, measurement, and coordination.

4.5.3 Integration with Energy Management System (EMS)

The EMS communicates with the dynamic load models using control signals that dictate the real-time active power command. The load model in MATLAB/Simulink adjusts its consumption accordingly, allowing simulation of realistic demand-side behaviour.

4.6 Model Validation Through Simulation Studies

Two different simulation are conducted on the IEEE-39 bus system, and their results are discussed. Firstly, the functionality of a DL-EMS within a BSA is assessed via MATLAB/SIMULINK simulations, validating its performance across various scenarios including normal operation, black start, night-time operation, load shedding, and emergency situations. Secondly, the black start scenario is examined within the framework of the TL-EMS under the HLC, aiming to assess the efficiency of transmission line control strategies and the

black start scenario's performance of the DL-EMS within the BSA.
To further evaluate the robustness of the proposed method, two additional scenarios are tested on the IEEE-10 bus system. In this case, the DL-EMS is tested under two different weather conditions cloudy and sunny days to evaluate its adaptability and efficiency in managing distributed energy resources under varying environmental scenarios.

4.6.1. DL-EMS in a BSA

The performance of a DL-EMS in a BSA is evaluated through a MATLAB/SIMULINK simulation. The specified BSA configuration includes a pair of solar panels operating in parallel, coupled with a battery storage unit and a fuel cell system, all of which are interfaced with the local utility grid. This comprehensive validation includes various operational scenarios, namely, normal, black start, night, load shedding, and emergency operations. Figure 4.1(a, b) show outcomes associated with the normal operational scenario wherein load shedding is inactive.

Within this mode, priority is accorded to the operation of all loads in the presence of solar irradiation. As shown in Figure 4.1 (a), the power generated by the solar panels follows the expected pattern of increasing with sunrise, peaking at midday, and decreasing towards sunset. Initially, when solar power is not enough to meet the total demand, the system uses both solar and battery power to cover all loads until about 9 AM. By midday, the solar power is sufficient for both load demands and to charge the battery. After the battery is fully charged, which is evident by the 100% SoC shown in Figure 4.1 (b), any additional power is then supplied to the grid, which happens just after 12 PM.

At around 2 PM, when the HLC indicates that extra power is not needed, the system stops supplying power to the grid, and the grid support (*gridSupp*) in the DL-EMS is deactivated. The DL-EMS then switches off the MPPT and changes to voltage regulation control for the solar panels, adjusting their output to just meet the requirements of the three loads. This operation continues in voltage regulation mode until about 5 PM. After this, as the solar output drops below the total load demand, the battery starts discharging to ensure all loads continue to receive power. During this process, the system keeps the DC voltage stable, as shown in Figure 4.1 (b). Throughout this, there is no need for fuel cell power (*FPwr*), as the scenario does not include any emergencies, and the system focuses on powering all three loads

continuously. Figure 4.2 (a, b) illustrate the load shedding operational scenario for the DL-EMS.

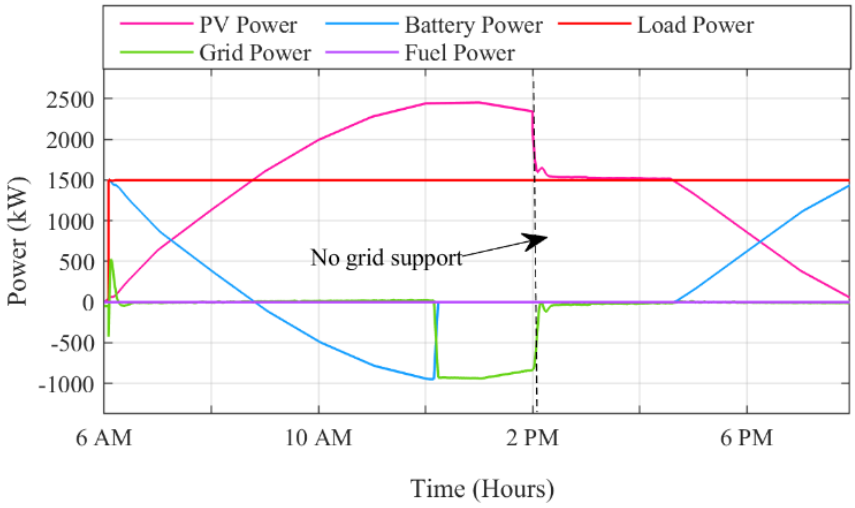

(a)

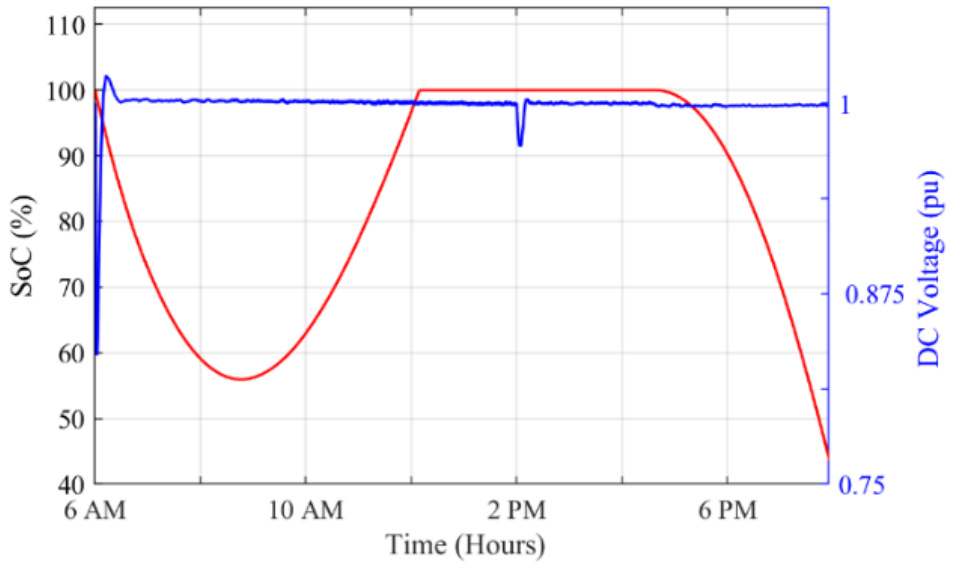

(b)

Figure 4-1(a) Daily power flow in the normal scenario: solar, battery, BSA load, fuel cell power, and grid interaction power. (b) Normal scenario battery SoC and DC voltage of the PV side throughout the day.

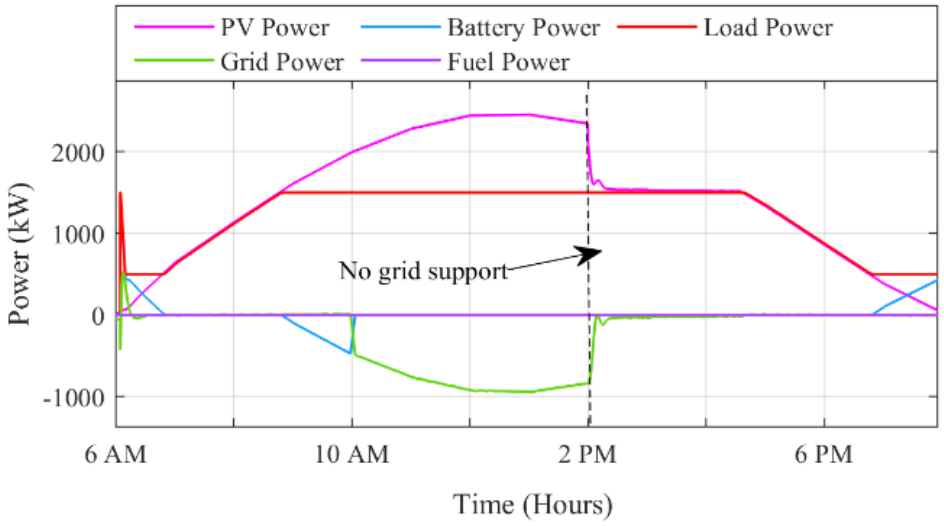

(a)

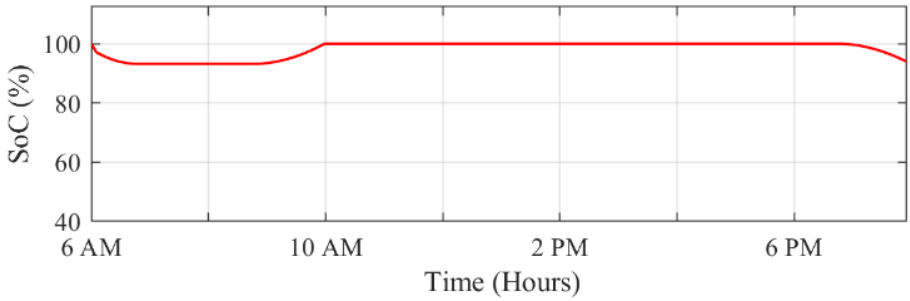

(b)

Figure 4-2 (a) Daily power flow in load shedding scenario: solar, battery, BSA load, fuel cell power, and grid interaction power. (b) Load shedding scenario battery SoC throughout the day

Under this scenario, the system operates primarily on solar power, with load shedding actively involved. According to the predetermined operational pathway, priority is given to charging the battery before supporting the two less critical loads, as long as the battery's SoC is below 70%. Initially, when solar power alone is insufficient for the most critical load, the battery supplements the shortfall. As the morning progresses and solar power generation exceeds the demand of the critical load, battery charging does not take priority, as the SoC is already above 70%, as demonstrated in Figure 4.2 (b).

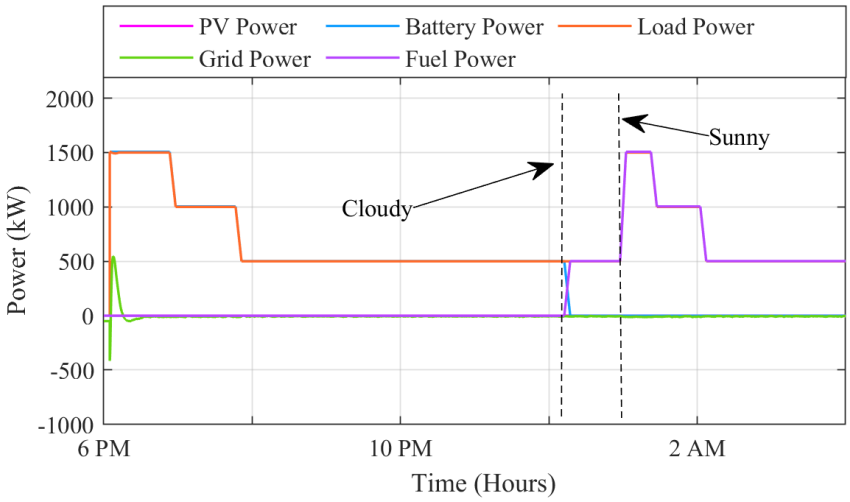

(a)

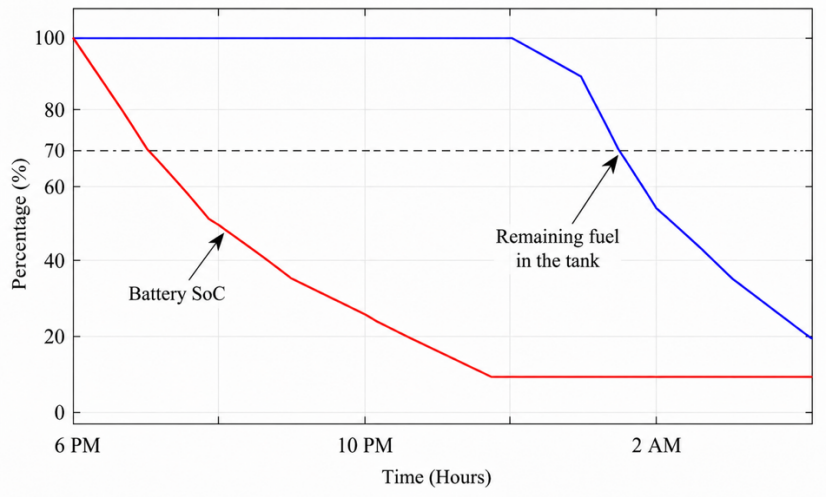

(b)

Figure 4-3 (a) Daily power flow in night and emergency scenarios: solar, battery, BSA load, fuel cell power, and grid interaction power. (b) Night and emergency scenario battery SoC and remaining fuel percentage in the fuel tank throughout the day.

In such cases, the additional solar power is distributed to the loads, with the less critical load receiving power based on the available solar energy. It is important to note that the battery does not discharge to support the less critical loads beyond its nominal power during this period. This strategy preserves battery reserves for night-time operation. By 9 AM, when solar production surpasses the combined demand of all three loads, any surplus energy contributes to battery charging until it reaches full capacity. Thereafter, any excess is sent to the grid. This sequence continues until approximately 2 PM when the need for excess power in adjacent areas

ceases, prompting the deactivation of grid support. The system then switches to voltage regulation mode, similar to the normal operational strategy. Approaching 5 PM, as solar power reduces below the total load demand, the system adapts by allocating the available solar power to the less critical loads (Loads 2 and 3) without relying on the battery. In keeping with the load shedding protocol, the system progressively reduces power to these non-critical loads as solar input decreases. Finally, by 7 PM, when solar energy falls short of even the most critical load's demand, the battery intervenes to sustain full operation of this critical load.

In scenarios where solar power is not available, the system transitions to its night operation mode. Figure 4.3 (a, b) describe the night operation and emergency scenarios. With the battery initially fully charged at 100% SoC, it begins to supply energy to all connected loads. As the battery's charge level reduces, it progressively reduces support, disconnecting power to Load 3 at approximately 7 PM and Load 2 by 9 PM, as shown in Figure 4.3 (a). In cases where the battery's charge falls below 10% by midnight, the system enters an emergency operation mode.

At this point, if the weather forecast for the following day indicates cloudiness, the system prioritises power supply to only the most critical load starting from midnight. Conversely, if a sunny day is predicted, the system activates the fuel cell to power all loads starting around 1 AM. This approach ensures that the energy management strategies are tailored to meet user preferences, embodying a user-focused design in the power distribution framework. Moreover, by incorporating next-day solar irradiance forecasts, the system can make informed decisions on load management, thereby enhancing the reliability and efficiency of power provision for upcoming operations. Figure 4.4 illustrates the grid topology utilised for testing the proposed energy management system. Specifically, Figure 4.4 (a) depicts the IEEE 39 standard bus system, which serves as the testing environment for the TL-EMS. Conversely, Figure 4.4 (b) represents the distribution network used to evaluate the DL-EMS.

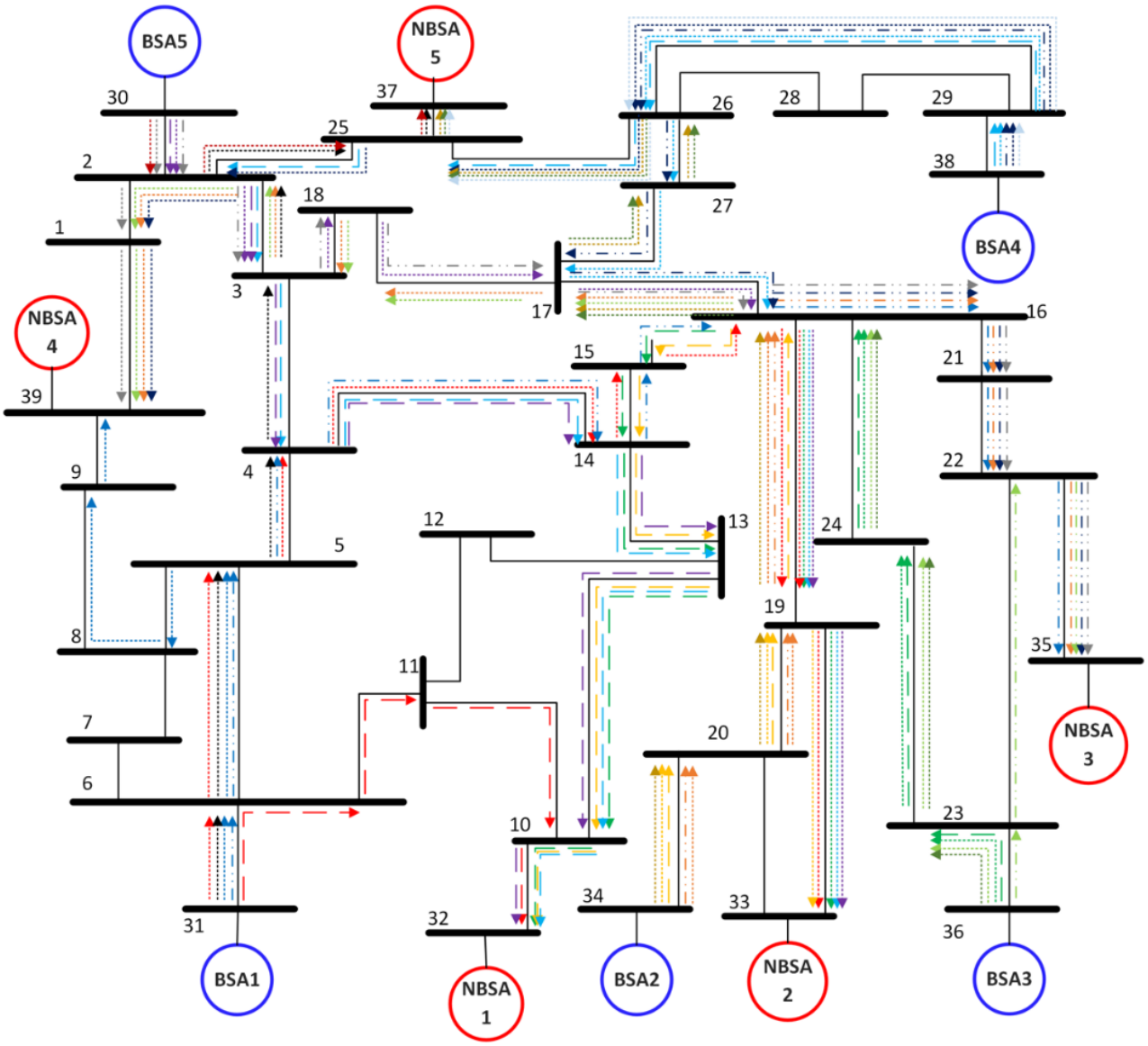

BSA1-NBSA1		BSA1-NBSA2		BSA1-NBSA3		BSA1-NBSA4		BSA1-NBSA5	
BSA2-NBSA1		BSA2-NBSA2		BSA2-NBSA3		BSA2-NBSA4		BSA2-NBSA5	
BSA3-NBSA1		BSA3-NBSA2		BSA3-NBSA3		BSA3-NBSA4		BSA3-NBSA5	
BSA4-NBSA1		BSA4-NBSA2		BSA4-NBSA3		BSA4-NBSA4		BSA4-NBSA5	
BSA5-NBSA1		BSA5-NBSA2		BSA5-NBSA3		BSA5-NBSA4		BSA5-NBSA5	

(a)

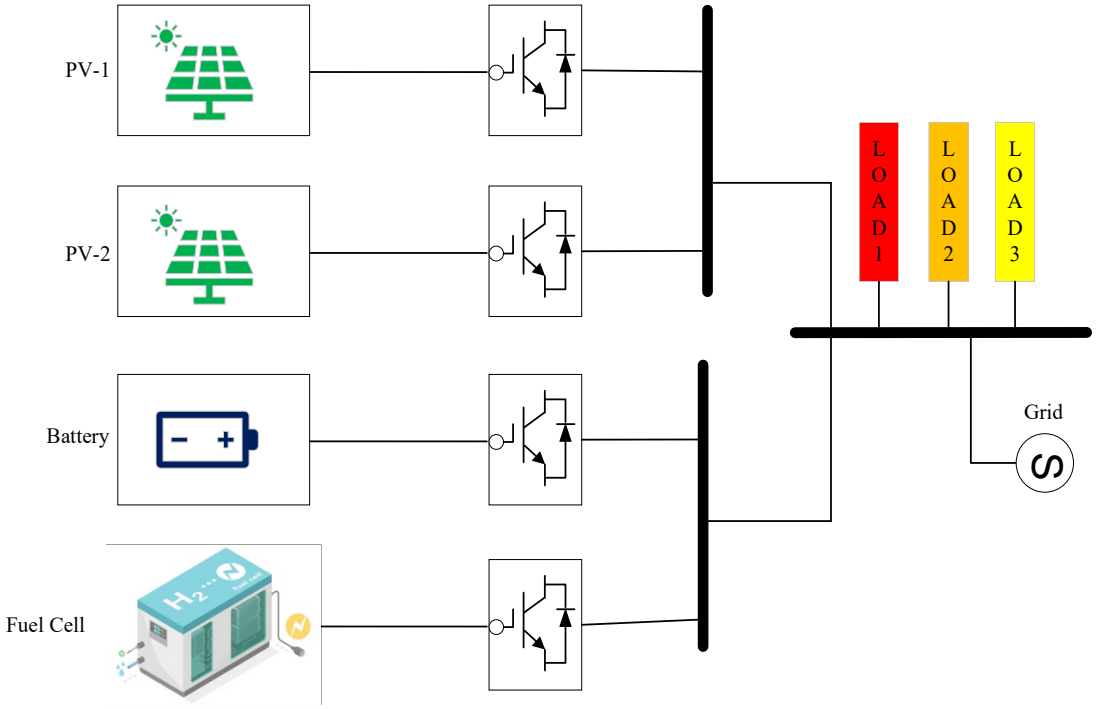

(b)

Figure 4-4 Comprehensive diagrams of transmission and distribution networks: (a) detailed diagram of the IEEE 39-Bus transmission system with minimum-impedance path determination for black start restoration using Dijkstra's algorithm between BSAs and NBSAs, and (b) detailed diagram of the distribution network for the BSAs.

4.6.2 TL-EMS under the HLC

The black start scenario is analysed within the context of the TL-EMS under the HLC, to evaluate the effectiveness of the transmission line control strategies and the black start scenario at DL-EMS in BSAs. This validation utilises the IEEE 39-Bus system, segmenting it into ten different areas comprising five BSAs and five NBSAs. The BSAs are situated at buses 30, 38, 31, 34, and 36, while the NBSAs, which include steam generators, are located at buses 37, 39, 32, 33, and 35. In the event of a black start, the HLC within TL-EMS collects data from both BSAs and NBSAs and then identifies the most efficient path from each BSA to each NBSA, as depicted in Figure 4.4 (a). The algorithm prioritises the impedance of the transmission lines, applying it as a penalty factor to determine the minimum-impedance path, ensuring that the selected path not only is the shortest but also minimises impedance across the network. Table 4.5 presents the characteristics of the synchronous generators situated in the NBSAs, detailing key operational parameters necessary for the black start process. The table lists each generator's cranking time (T_{crank}), the minimum critical time (T_{gcmin}), and the maximum critical time (T_{gcmAX}). It also includes the ramp rate (R_r), which is the rate at which the generator can

increase its power output per hour, the cranking power (P_{crank}) required for initiating the generator, and the generator's maximum power output capacity (P_{max}). Moreover, Table 4.6 outlines the durations necessary to complete various generic restoration actions critical to providing power to NBSAs. It specifies the time required to energise a busbar from a battery storage unit (BSU), a busbar, or a line. Furthermore, the duration for synchronisation activities is between busbars or lines. Additionally, the time needed to pick up a load and integrate it into the power system is also documented. These timings are essential for the precise sequencing and coordination of restoration tasks following a blackout.

Table 4-5 Data of generator characteristics [57].

Gen.	T_{crank} (h)	T_{gcmin} (h)	T_{gcmax} (h)	R_r (MW/h)	P_{crank} (MW)	P_{max} (MW)
G1	0:20	N/A	0:40	12	1.5	8
G2	0:10	0:50	N/A	24	1	12
G3	0:20	N/A	N/A	24	2	20
G4	0:10	0:20	N/A	24	1	12
G5	0:30	N/A	N/A	50	5	40

The HLC started the black start process at 10 AM with areas BSA1, BSA3, and BSA5 being assumed to operate under the load shedding scenario, while BSA2 and BSA4 maintained normal operation. The HLC received critical data from these areas, including the reserve power available from solar panels, batteries, and fuel cells, along with the operational status of less critical loads: L_2 and L_3. In the event of insufficient power from the primary sources for the black start requirements, the HLC could deactivate these less critical loads, repurposing their power to support the black start. The SoC of the batteries and the fuel percentage for each BSA were also transmitted to the HLC, providing a comprehensive overview of available energy reserves for decision-making. Figure 4.5 (a) depicts the reserve powers from the various sources against the BSAs, complete with an indication of the operational states of L_2 and L_3. As shown in Figure 4.5 (a), the reserve power from PV sources exhibits variation across the BSAs, attributed to the differing levels of solar irradiance each area receives. In area 4, the battery SoC has reached its minimum allowable threshold of 10%, as defined by the dept-of-discharge protection, indicating it is unable to contribute to black start process. Additionally, area 3's fuel reserves are zero, leaving it non-contributory in the black start process.

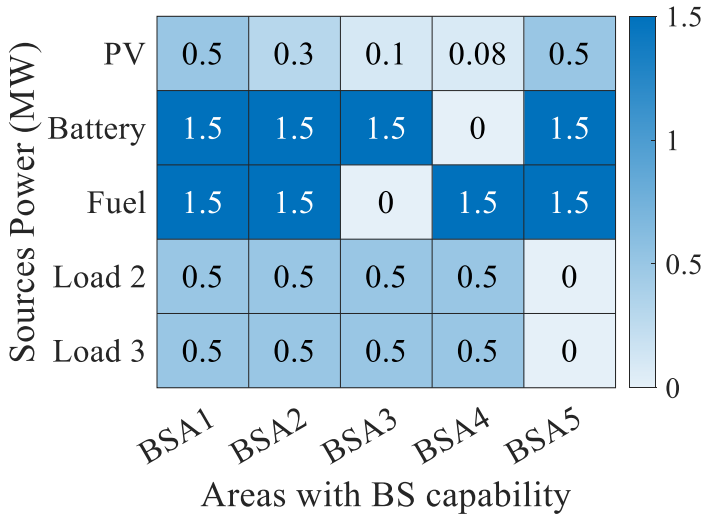

(a)

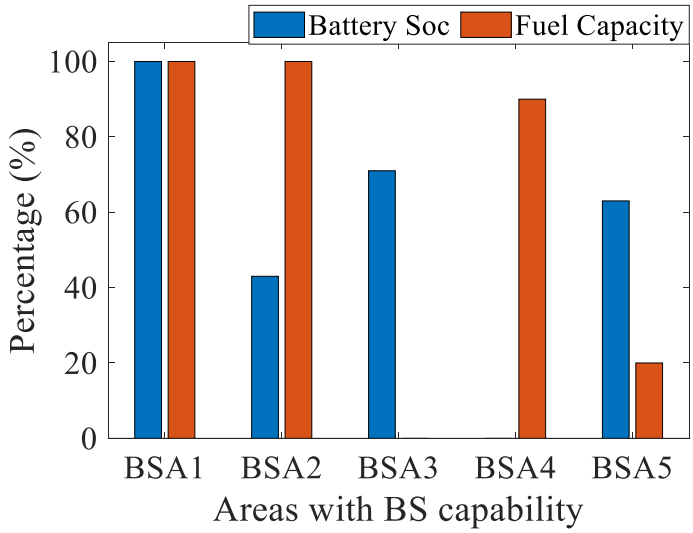

(b)

Figure 4-5 Information received from BSAs: (a) reserve power distribution and load status in BSAs; (b) battery SoC and remaining fuel percentage in BSAs

Finally, the HLC has the option to utilise the power designated for Load 2 and Load 3 across all BSAs, with the exception of BSA5. In BSA5, these loads are not currently powered and are in an offline state. Figure 4.5 (b) describes the SoC and the available fuel percentages across all the BSAs. From Figure 4.5 to Figure 4.9, one can observe the varying assumptions across all BSAs, allowing for the evaluation of the proposed EMS under various random operational scenarios and states. Additionally, the HLC gathers data concerning the generators in NBSAs, as well as information about the power network, as detailed in Tables

4.2 and 4.3. Upon receiving the necessary details from both the BSAs and the NBSAs, the HLC proceeds to determine the most efficient order for initiating the generators. As shown in Figure 4.6(a), G3 requires 2 MW of cranking power. This is supplied by: BSA1 (0.5 MW PV), BSA2 (0.3 MW PV), BSA3 (0.1 MW PV + 0.52 MW battery), BSA4 (0.08 MW PV), and BSA5 (0.5 MW PV). BSA3 provides the largest share as it is the nearest BSA to G3, consistent with the distribution factor from Dijkstra's algorithm.

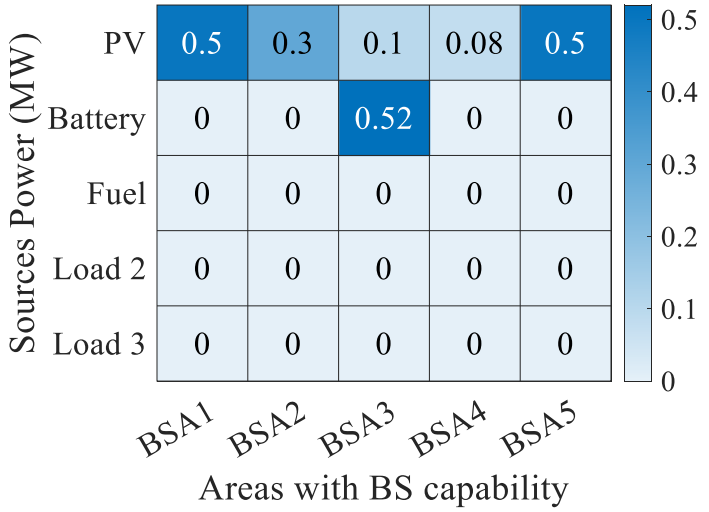

(a)

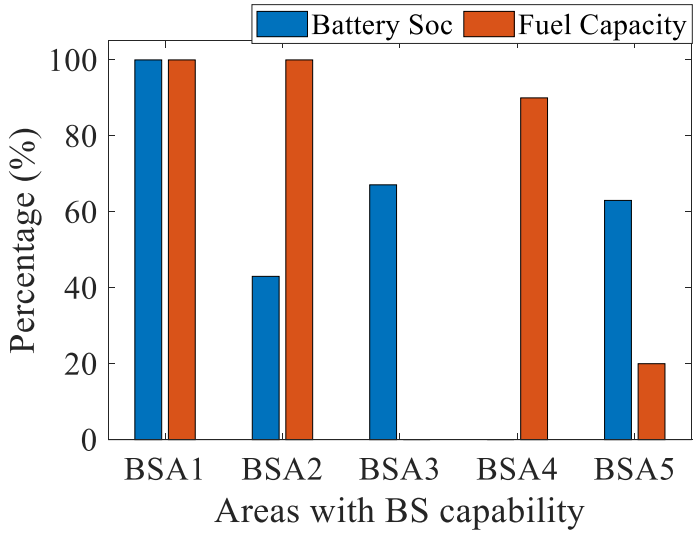

(b)

Figure 4-6 Information received from BSAs: (a optimal power allocation for G3 startup from BSAs; (b) SoC and fuel percentage post-cranking for G3.

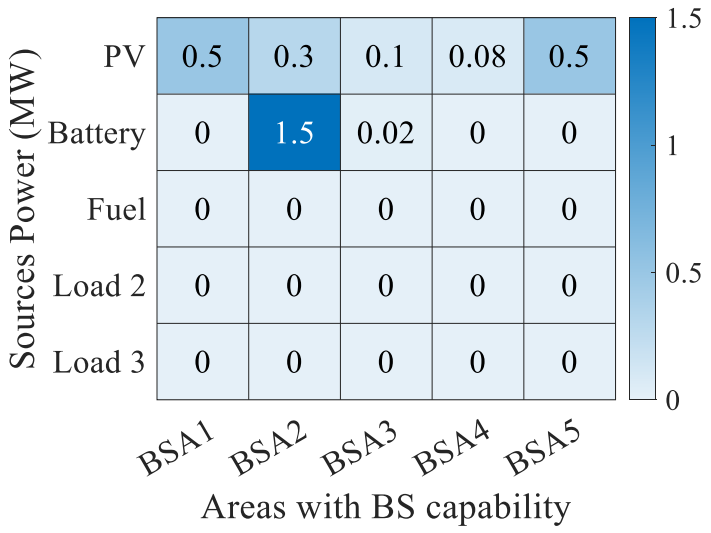

(a)

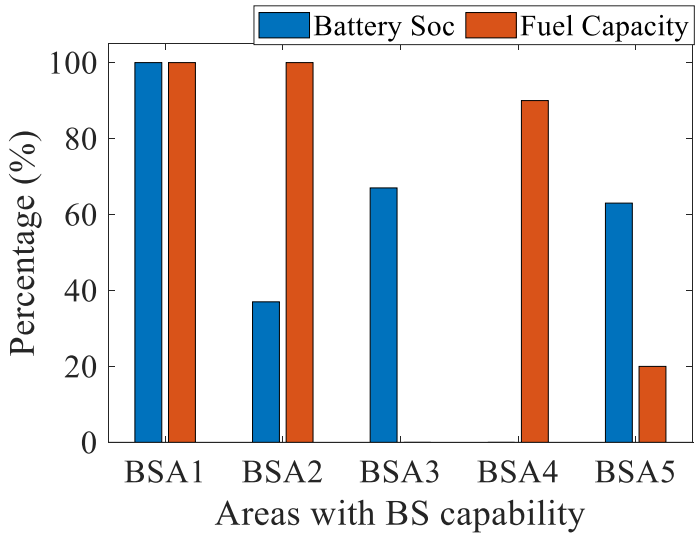

(b)

Figure 4-7 Information received from BSAs: (a) optimal power allocation for G4 and G2 startup from BSAs; (b) SoC and fuel percentage post-cranking for G4 and G2.

As shown in Figure 4.7(a), G4 and G2 require a combined cranking power of 3 MW (1 MW for G4 + 2 MW for G2, from Table 4.5). This is supplied by: BSA1 (0.5 MW PV), BSA2 (0.3 MW PV + 1.5 MW battery), BSA3 (0.1 MW PV + 0.02 MW battery), BSA4 (0.08 MW PV), and BSA5 (0.5 MW PV). The SoC and fuel percentages in Figure 4.7(b) show minimal visible change compared to Figure 4.6(b) because the cranking duration is only 10 minutes and the power is predominantly sourced from PV, which does not deplete stored energy reserves. The small battery contributions from BSA2 and BSA3 over this short period result in only marginal SoC reductions. The HLC arranges the generators listed in Table 4.2 based

on their starting characteristics, prioritising those with shorter cranking times. Next, generators with the lowest maximum starting time are sequenced, followed by those with the minimum starting time at the forefront of the list. The final organised sequence for generator startup is G3, followed by G4, G2, G1, and lastly G5. Once the optimal startup sequence is established, the HLC verifies the availability of sufficient reserve energy to cover the energy required from the startup of these generators, by employing Equations (4.1) and (4.2). Following a successful assessment of the available reserve energy, the HLC initiates the startup process. This optimisation procedure lasts approximately 5 min, as detailed in Table 4.4, which outlines the steps to restore the power system. The HLC begins the process of energising each bus and its connected branches, prioritising proximity to the nearest BSA while ensuring the reactive power remains within the capabilities of the BSA. G4 and G2 are started simultaneously because they have identical cranking times of 10 minutes Table 4.5, and the total reserve energy available from the BSAs is sufficient to supply both generators concurrently (combined cranking power of 3 MW). Starting them together reduces the total restoration time rather than sequentially cranking each one separately."

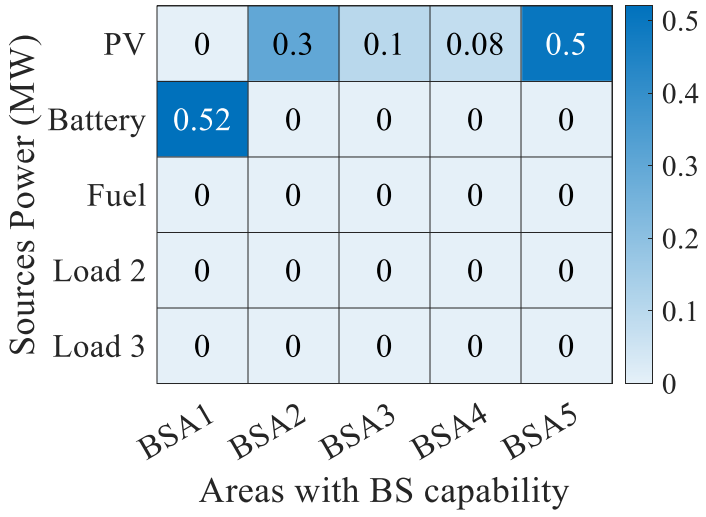

(a)

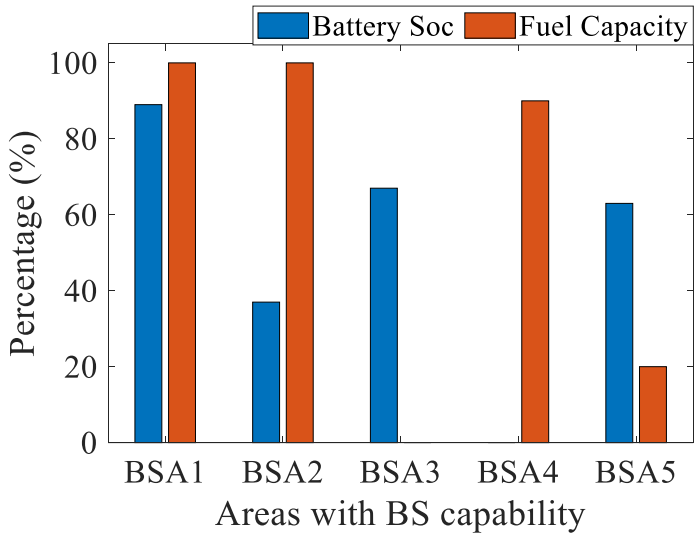

(b)

Figure 4-8 Information received from BSAs: (a) optimal power allocation for G1 startup from BSAs; (b) SoC and fuel percentage post-cranking for G1.

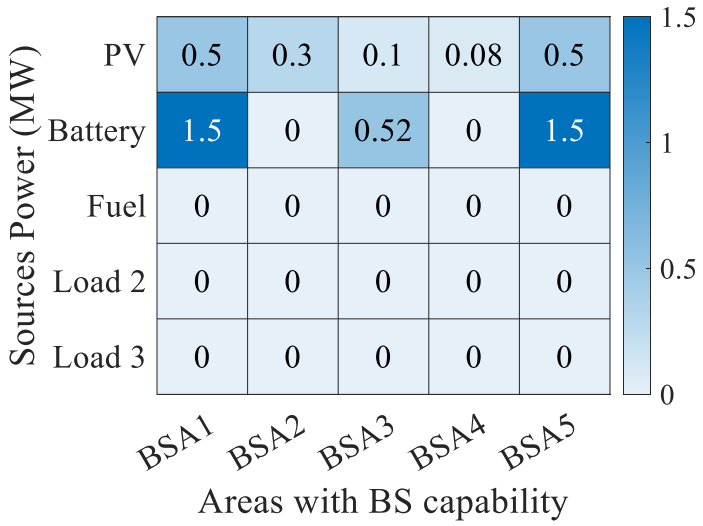

(a)

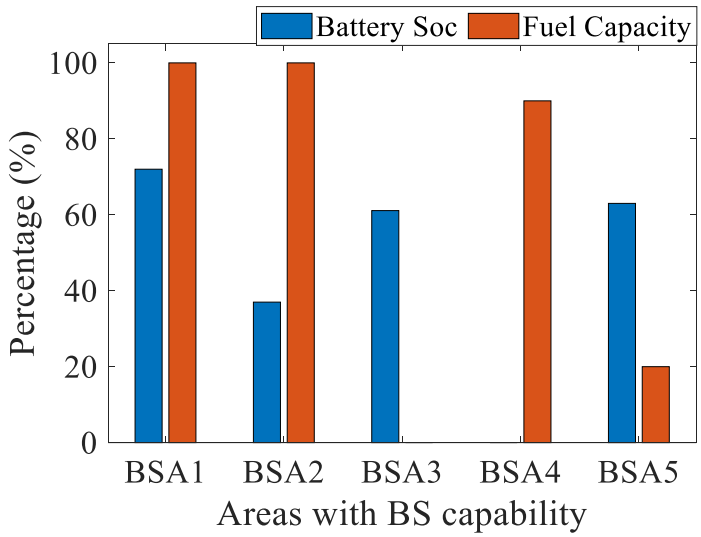

(b)

Figure 4-9 Information received from BSAs: (a) optimal power allocation for G5 startup from BSAs; (b) SoC and fuel percentage post-cranking for G5.

In the IEEE 39-bus black start scenario, the fuel cell was not required because the combined PV and battery reserves across all BSAs were sufficient to supply the cranking power for all five generators. However, the fuel cell is actively used in the DL-EMS emergency scenarios, as demonstrated in Figure 4.3(a) where the fuel cell supplies the critical load when the battery SoC drops below 10%, and in Figure 4.12(c) during the cloudy day scenario on the IEEE 10-bus system where the fuel cell sustains L_1 throughout the night. The fuel cell serves as a last-resort backup, activated only when PV and battery resources are exhausted, consistent with the cost-based priority defined in the optimisation function (Eq. 3.6) where solar is preferred over battery, and battery over fuel cell. This energisation occurs simultaneously at various network locations. Starting with BSA3, it powers buses 36, 23, 22, and 25, along with their interconnecting branches as detailed in Table 4.3. Concurrently, BSA2 activates buses 34, 20, 19, 16, 21, 24, and 33 and their connecting branches. In parallel, BSA4 is responsible for energising buses 38, 29, 26, 27, 17, and 28 and the branches linking them. BSA5 simultaneously energises buses 30, 2, 3, 18, 1, 25, 37, and 39 and their branches. Meanwhile, BSA1 activates buses 31, 6, 5, 4, 14, 15, 7, 8, 9, 11, 12, and 10 and their connections. An attempt is made to also energise buses 13 and 32 from BSA1, but high reactive power could lead to instability in BSA1 operations, postponing their energisation until other buses are powered. This entire process takes about 5 min, as indicated in Tables 4.3 and 4.4.

Table 4-6 Time to complete restorative actions [104].

Generic Restoration Action	Time (mins)
Energise busbar from BSU/busbar/line	5
Synchronise between busbar/line	10
Pick up load	5

After powering up most of the buses and linking them to their nearest BSA, the network is divided into several segments without interconnections. The next step involves synchronising these segments to unify the network. BSA3 synchronises with BSA2, while attempts are also made to synchronise BSA4 and BSA5 with BSA1 at the same time. This process, lasting about 10 min as indicated in Tables 4.3 and 4.4, effectively creates two main interconnected zones: one consisting of BSA3 and BSA2, and another comprising BSA1, BSA4, and BSA5. Subsequently, the focus shifts to energising previously postponed buses 13 and 32 within the area that includes BSA1, along with their branches. This energisation takes about 5 min. Finally, the ultimate goal is to merge these two interconnected zones into a single, unified network, a task that also requires around 10 min for synchronisation. Once the network becomes fully interconnected, incorporating all five BSAs, the remaining extra branches that connect buses 18 to 17, 17 to 16, and 15 to 16 are energised, thus fully integrating all areas. With the network now operating as a single interconnected entity, the process moves on to start the NBSAs and integrate them into the grid, completing the restoration effort. The HLC initiates the startup process with G3, identified as the first in the optimal startup sequence. Figure 4.6 (a) illustrates the optimal power allocation determined by the HLC's optimisation problem, using available BSAs to supply the necessary cranking power to G3. Predominantly, the power for G3 originates from BSA3, the closest BSA to G3, with solar PV energy prioritised due to its lower cost, making it the preferred energy source from all BSAs. The only battery power utilised comes from BSA3, offering the most efficient cranking solution for G3. Figure 4.6 (b) shows the subsequent changes in the SoC and fuel percentages after drawing power for the cranking process. The cranking duration is set at 20 min, as detailed in Tables 4.2 and 4.4. Once cranking is completed, G3 successfully starts, becoming parallel and interconnected with the unified grid. Following this stage, the HLC starts the next generator in the list. The HLC selects G4 and 2 to start simultaneously due to their identical cranking times and the availability of enough energy to crank both at once. The combined cranking requirement for these generators is 3 MW. The strategy to meet this demand involves prioritising available solar power for its cost efficiency, with the additional necessary power supplied through the most direct route offering the highest equivalent inertia from BSA2 and BSA3, as depicted in Figure

4.7 (a). The cranking duration for both generators is set at 10 min. Once cranking is completed success fully, both generators are synchronised and integrated with the unified grid. Figure 4.7 b) shows the updated SoC and fuel percentages after cranking both generators. Subsequently, the HLC proceeds to the next generator on the list, G1, which requires 1.5 MW for cranking. During this phase, the HLC is informed by the LLC of BSA1 about a cloud cover, reducing the solar power reserve from 0.5 MW to zero.

The HLC then recalibrates its optimisation algorithm for these altered conditions, determining the best power allocation for starting G1, as depicted in Figure 4.8 (a). This allocation still relies on solar power from all BSAs and the battery from BSA1, deemed the most efficient pathway to G1. Figure 4.8 (b) updates the SoC and fuel percentages following the cranking of G1. After 20 min, G1 successfully starts and is synchronised with the unified grid. The HLC then initiates the startup of the final generator on the list, G5, which requires 5 MW of cranking power. This power is sourced from the most cost-effective options, primarily solar, and from BSAs that contribute to increasing inertia, specifically BSA1 and BSA5, while minimising reliance on the more expensive fuel cell power. This allocation strategy is illustrated in Figure 4.9 (a). Furthermore, Figure 4.9 (b) presents the final SoC and fuel percentages following system restoration. The cranking of G5, lasting 30 min, leads to its successful startup and synchronisation with the entire network, marking the completion of the system's full restoration. At this point, the HLC issues a command for all BSAs to exit black start mode and return to their standard operational pathways.

4.6.3 Comparative Analysis

The proposed hierarchical energy management system enhances black start capabilities and normal operations across both distribution and transmission networks. This dual-level approach is unique in the literature, as no existing methods address energy management at both levels with black start support. Consequently, there is no direct comparison for a hierarchical EMS that integrates both DL-EMS and TL-EMS. Nevertheless, comparisons are conducted separately at each level: the TL-EMS is compared with similar methods in the literature for black start support utilising renewable energy, and the DL-EMS is compared with its similar methods. This approach underscores the superiority of the proposed method at both levels, highlighting the unique contributions of the advanced DL-EMS and TL-EMS, as well as their hierarchical coordination for energy management across both distribution and transmission networks.

Table 4-7 Actions to restore entire power system.

Time (H)	Action	Target	Comment
10:00	Optimisation	Define the best sequence to start the generators	
10:05	Energise	Buses 36, 23, 22, 25 Branches BSA3–36, 36–22, 23–22, 22–25	
10:05	Energise	Buses 34, 20, 19, 16, 21, 24, 33; Branches BSA2–34, 34–20, 20–19, 19–16, 16–21, 16–24, 20–33, 19–33	
10:05	Energise	Buses 38, 29, 26, 27, 17, 28 Branches BSA4–38, 38–29, 29–26, 26–27, 27–17, 29–28, 28–26	
10:05	Energise	Buses 30, 2, 3, 18, 1, 25, 37, 39 Branches BSA5–30, 20–2, 2–3, 3–18, 2–1, 2–25, 25–37, 1–39	
10:05	Energise	Buses 31, 6, 5, 4, 14, 15, 7, 8,9, 11, 12, 10 Branches BSA1–31, 31–6, 6–5, 5–4, 4–14, 14–15, 6–7, 7–8, 8–5,8–9, 6–11,11–12, 11–10	Tries to energise buses 13 and 32 and branches 12–13 and 10–32 but fails due to high reactive power that may cause instability
10:10	Synchronise	Between BSA3 and BSA2; Bus 21 with Bus 22 Between BSA1, BSA4 and BSA5, Bus 18 and Bus 17, Bus 4 and Bus 3	
10:20	Energise	Bus 13, 32 Branch 12–13, 14–13, 10–13, 10–32, 21–22 9–39, 4–3, 25–26, 24–23	
10:25	Synchronise	Between BSA3/BSA2 and BSA4/BSA5/BSA1	
10:35	Energise	Branches 18–17, 17–16, 15–16	
10:40	Crank	G3	
10:60	Parallel	G3	Successful
11:05	Crank	G4, G2	
11:15	Parallel	G4, G2	Successful
11:20	Crank	G1	
11:40	Parallel	G1	Successful
11:45	Crank	G5	
12:05	Parallel	G5	Successful
12:10		End of black start	

It is important to acknowledge the underlying assumptions of the proposed hierarchical EMS. First, the system relies on robust communication infrastructure between the DL-EMS and TL-EMS layers; any communication failure or latency could impact the coordination and delay restoration actions. Second, the optimisation assumes full availability of real-time information from all BSAs, including accurate SoC readings, fuel levels, and PV output measurements. In practice, sensor failures or data losses may degrade performance. Third, the PV generation is assumed to follow predictable patterns based on irradiance forecasting; however, rapid cloud transients (as partially demonstrated in the G1 cranking scenario in Figure 4.8) can cause sudden drops in available power. While the system demonstrated adaptability by switching to battery backup during cloud cover, prolonged or widespread reductions in PV output would place greater reliance on battery and fuel cell reserves. Fourth, the black start mitigation strategy assumes that BSA energy reserves are sufficient to cover all generator cranking requirements sequentially. Future work should address these limitations by incorporating communication redundancy protocols, stochastic PV forecasting models, and sensitivity analyses under degraded communication and variable renewable generation conditions.

Firstly, the TL-EMS is compared with the methods in [105],[106], which optimise to maximise the area under the generation capability curve during black starts. The proposed optimisation, however, is unique and compatible with recent renewable energies, as it is structured to increase synthetic inertia, minimise load shedding, and maximise reliance on renewable and cost-effective energy sources during black starts while also considering proximity to the generator being started to minimise losses. The results and comparative analysis are shown in the following figures, where the different methods are tested against the proposed method on IEEE 39 buses. Figure 4.10 (a) illustrates the startup time for the five generators. The proposed method starts G1, G2, and G4 earlier than the other two methods, while G3 starts at the same time using all three methods, and G5 starts later using the proposed method. Overall, these results indicate that the proposed method generally aims to start the generators earlier, accelerating the startup process. Figure 4.10 (b) shows the computational time required by the three methods for optimising the black start on IEEE 39 buses. The proposed method has the longest computational time, which is attributed to its multi-objective optimisation approach, unlike the single-objective functions of the other methods. Despite the longer computational time, which is approximately 2.24 s, the optimisation addresses multiple aspects crucial for modern power systems with renewable energies. Moreover, this computational time is not significant compared to the black start process, which can take over an hour. Figure 4.10 (c)

demonstrates the system generation capacity during the black start. All methods complete the black start by around 13:00, but the proposed method shows higher generation capacity between 11:00 and 12:00, while the other methods show higher capacity from 12:00 to 13:00, ending with the same generation capacity. By achieving higher generation capacity early, the proposed TL-EMS supports more critical loads sooner, which minimises the need for load shedding. Moreover, the proposed TL-EMS's higher generation capacity during the initial stages demonstrates its capability to effectively maximise the dependency on renewable energy sources to start more generators early.

As shown in Figure 4.10(a), generator startup times range from 60 to 135 minutes, meaning the entire restoration process takes hours to complete. Therefore, the computational time difference of fractions of a second between methods is entirely insignificant in this context.

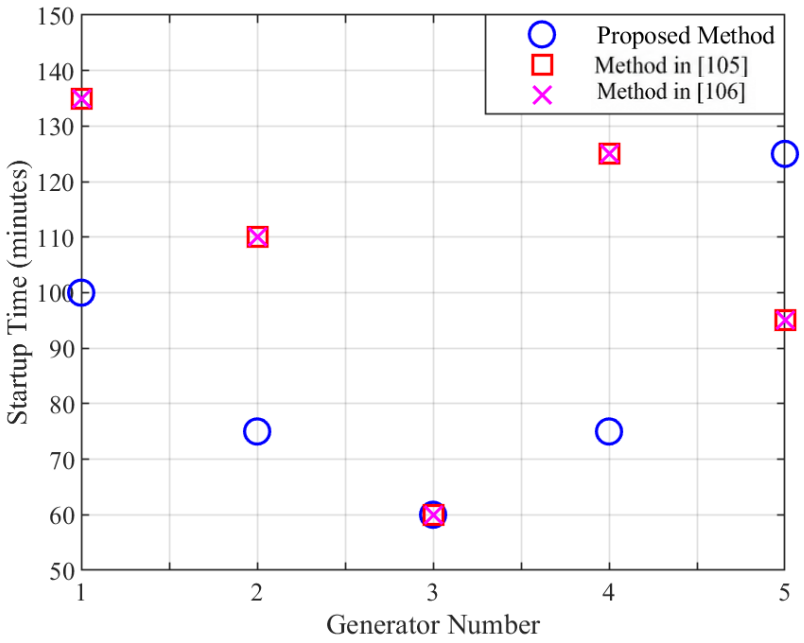

(a)

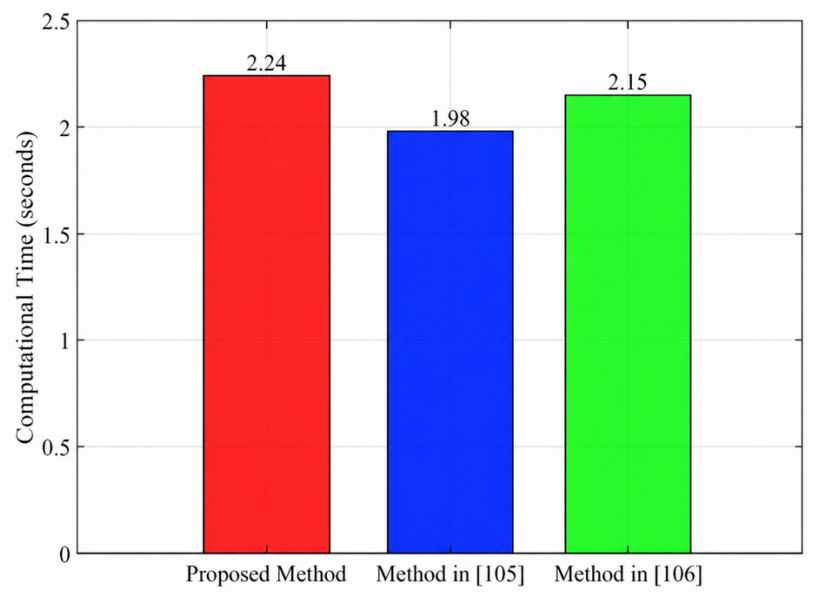

(b)

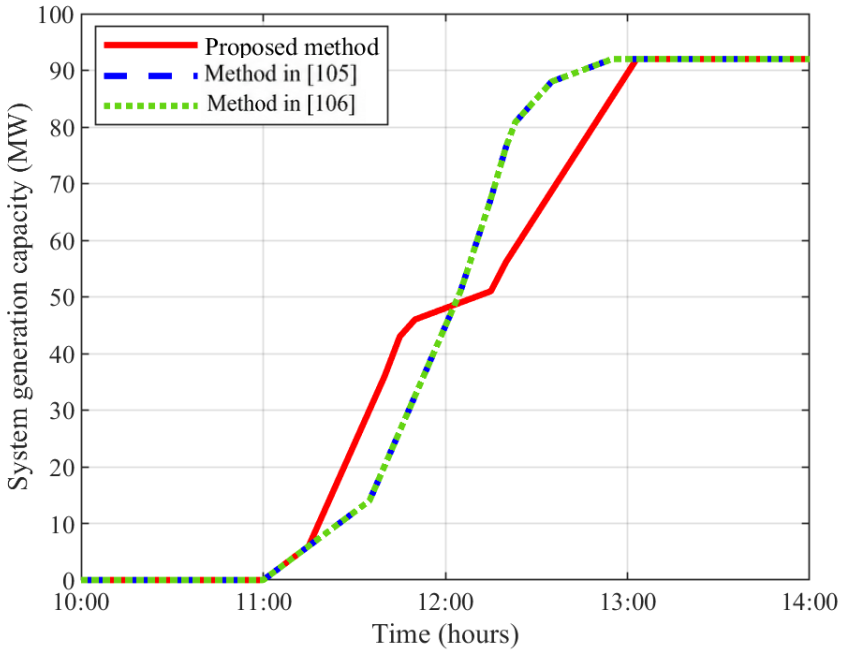

(c)

Figure 4-10 Comparative analysis of TL-EMS methods on IEEE 39 buses for black start: (a) generator startup times using the two methods against the proposed method; (b) computational time required by the three methods for optimising the black start on IEEE 39 buses; (c) system generation capacity during the black start process. The methods compared include the Proposed method, the method by El-Zonkoly 2015 [105], and the method by Su et al. 2022 [106].

Secondly, a comparative analysis is conducted for the DL-EMS. The proposed unique DL-EMS is evaluated against a similar distribution-level energy management system method

described in [107]. Overall, the proposed method demonstrates superiority due to its inclusion of five operational scenarios, including black start and emergency scenarios utilising recent hydrogen fuel cell technology, and its capability to support and connect to the grid. In contrast, the alternative method operates in a standalone manner, includes only three operational scenarios, and lacks both the advanced emergency technology and black start capabilities. Additionally, it fails to optimise the use of solar cells as it neither connects to the grid nor supports supplying excess power to the grid.

Figure 4.11 illustrates the results of the comparative analysis at the distribution level. Figure 4.11 (a) presents the outcomes of the method in [107], while Figure 4.11 (b) shows the results of the proposed method. As depicted in Figure 4.11 (a), the battery supports the three loads from 12 AM to 3:30 AM when no sunlight is available. However, the battery reaches minimum available SoC, leading to the disconnection of the loads, including the most critical load, due to the absence of an emergency scenario. In contrast, the proposed method includes an emergency scenario and supplies the most critical load during the same period, as shown in Figure 4.11 (b). Moreover, as the sun rises and solar power increases, the battery starts recharging and is fully charged by around 12 PM. After this time, the system in [107] must switch the solar power to voltage control mode instead of maximum power point tracking to stabilise the system, resulting in suboptimal use of the excess power. However, the proposed method, being grid-connected, allows the excess power to be delivered to the grid, thereby maximising the utilisation of solar power. Finally, around 9 PM during the night period, the battery discharges again. Without hydrogen fuel cell emergency support, the most critical load will be disconnected, as shown in Figure 4.11 (a, b) after 9 PM.

Moreover, a comparison in Table 4.5 summarises the key aspects of the proposed method and the methods in [105]–[107]. Overall, the results demonstrate the superiority of the proposed method over existing methods in the literature at both the distribution and transmission levels.

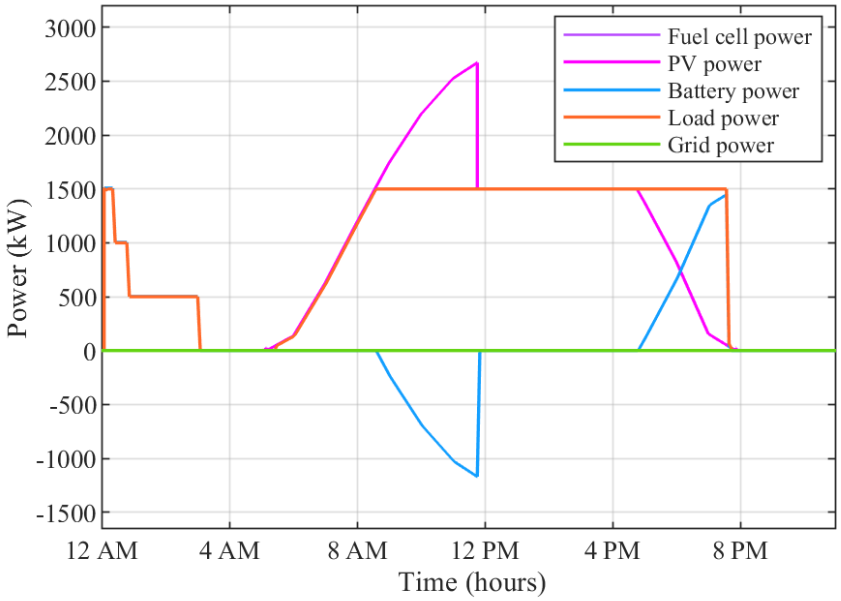

(a)

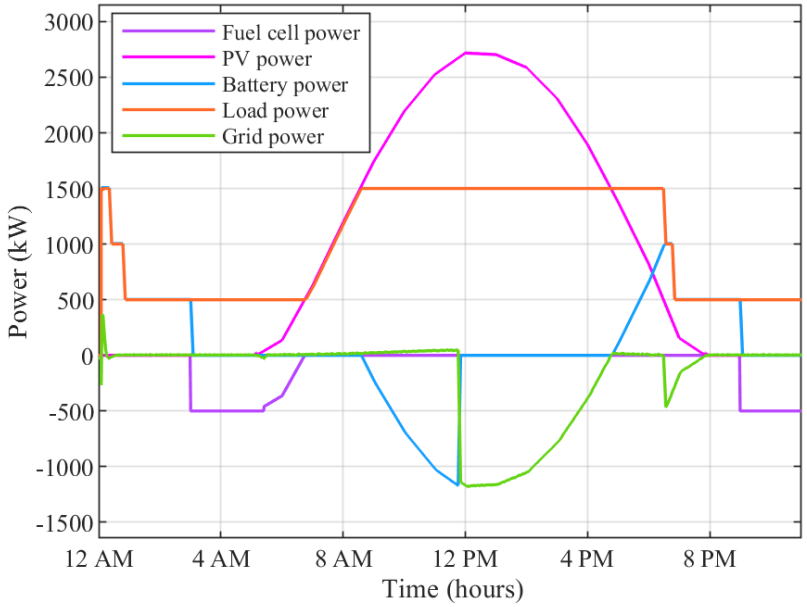

(b)

Figure 4-11Comparative analysis of DL−EMS methods: (a) results of methods in [107]; (b) results of the proposed method.

4.6.4 Additional Analysis on the IEEE-10 Bus System

The proposed energy management system has additionally tested on the IEEE 10-bus system to further demonstrate its effectiveness. Firstly, the distribution level energy management

system (DL-EMS) was tested under two different scenarios: a cloudy day on January 1, 2023, and a sunny day on August 15, 2023, for a location in England (lat: 52.1754, long: -1.3815) using Power Data Access Viewer from NASA [108].

Table 4-8 Comparison of energy management system methods at distribution and transmission levels.

Feature/Method	Proposed Method	Method in [105]	Method in [106]	Method in [107]
Levels addressed	Both distribution and transmission	Transmission only	Transmission only	Distribution only
Scenarios addressed	Normal and contingency scenarios at both levels	Black start only	Black start only	Normal scenarios only
Optimisation at transmission level	Maximise synthetic inertia, minimise load shedding, and maximise use of renewable energies	Optimise system generation capability curve only	Optimise system generation capability curve only	N/A
Emergency scenarios at distribution level	Yes	N/A	N/A	No
Grid connectivity at distribution level	Yes	N/A	N/A	No
Interoperability of generation sources	Yes	Yes	Yes	No

A. Cloudy Day (January 1, 2023)

The load shedding mechanism is activated, and the next day's estimation predicted cloudy conditions. Figure 4.12. describes the results for the cloudy day. During this period, solar irradiance is available only from 8 AM to around 3 PM, as shown in Figure 4.12.(a). Priority is given to the most critical load (Load 1) and to charging the battery if there is surplus power from the solar panels. The battery is discharged to supply deficiencies in supporting the critical load if the solar power is insufficient. Figure 4.12.(b) describes the SoC for the battery and the remaining fuel percentage in the tank during the morning period. As shown, the fuel is not used during the morning period, and the battery reached around 2.25% SoC by the end of this period. At night, with no sunlight and a SoC of around 2.25%, the system entered an emergency scenario, with a fuel cell supplying the most critical load throughout the night. Figures 4.12.(c) and 4.12.(d) illustrate the power supply and consumption during the night period, and the fuel percentage and battery SoC during the night, respectively. The battery is fully discharged first, followed by the fuel cell which supplied power until the fuel percentage dropped to around 16% by the end of the night.

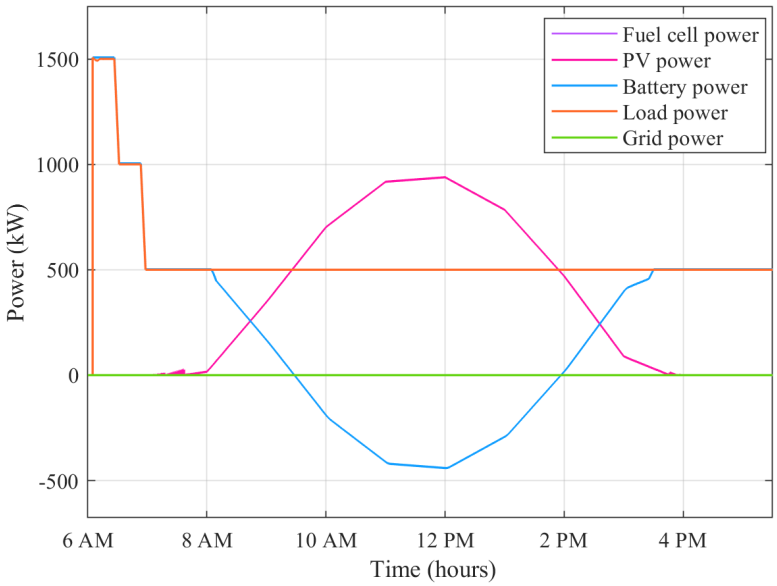
Fuel cell power
PV power
Battery power
Load power
Grid power
1500
1000
500
0
-500
Power (kW)
6 AM
8 AM
10 AM
12 PM
2 PM
4 PM
Time (hours)

(a)

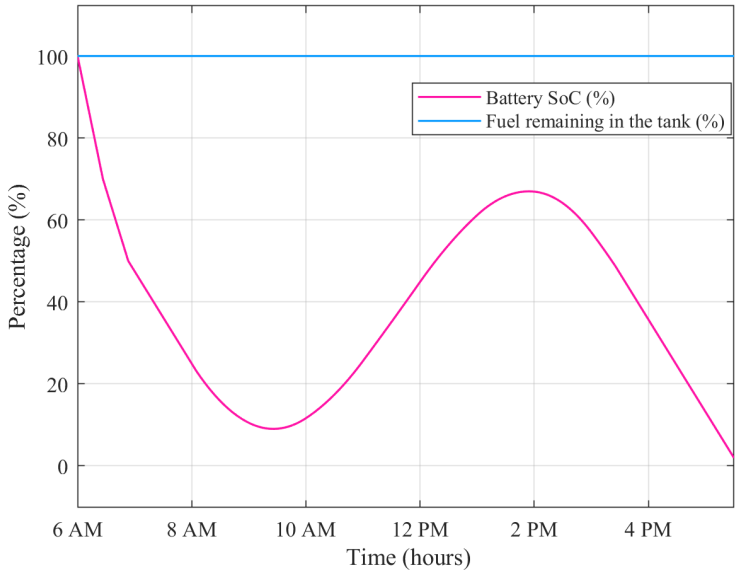
Battery SoC (%)
Fuel remaining in the tank (%)
100
80
60
40
20
0
Percentage (%)
6 AM
8 AM
10 AM
12 PM
2 PM
4 PM
Time (hours)

(b)

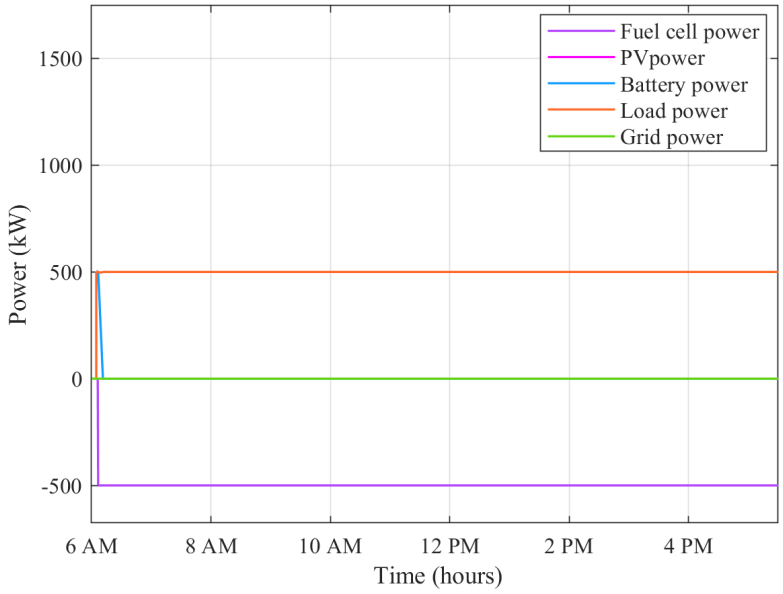

(c)

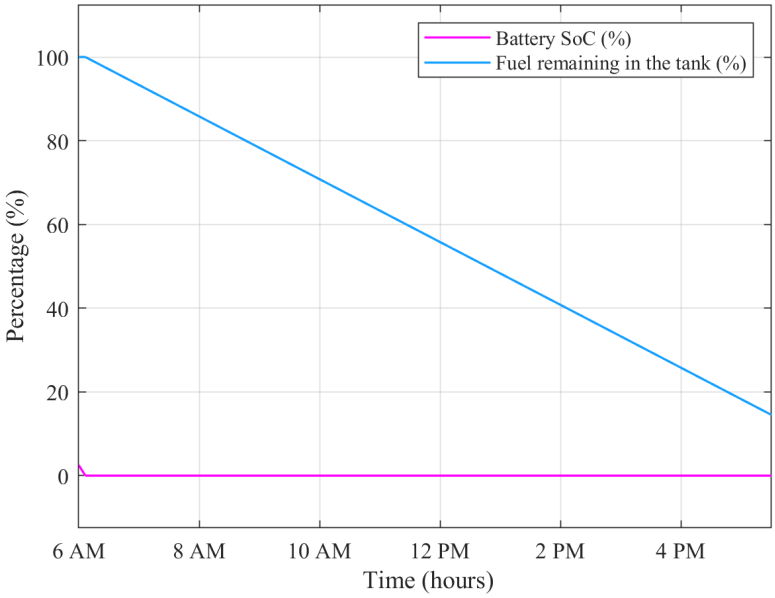

(d)

Figure 4-12 Results for the cloudy day scenario. (a) Power supply and consumption during the morning, (b) battery SoC and fuel percentage during the morning, (c) power supply and consumption during the night, and (d) battery SoC and fuel percentage during the night

B. Sunny Day (August 15, 2023)

Load shedding is deactivated due to the sunny forecast for both the current and following day. Figure 4.13 describes the results for the sunny day. All loads are supported with 1500 kW. If

solar power is insufficient to meet total loads, the battery supplied the deficiency, as shown in Figure 4.13 (a). Excess solar power charges the battery, and any surplus is exported to the grid if needed. Figure 4.13 (b) illustrates the SoC of the battery and the remaining fuel percentage in the tank during the morning. The battery is utilized only during the morning and ended with around 92% SoC, with no fuel usage since there is no emergency scenario during this period. During the night, with an SoC greater than 70%, the battery supplied all loads, disconnecting the least critical loads as the SoC decreased. Once the battery is fully discharged, the system enters an emergency scenario, with the fuel cell continuing to supply the most critical load. Figures 4.13 (c) and 4.13 (d) show the power supply and consumption during the night period, and the remaining fuel percentage and battery SoC during the night, respectively.

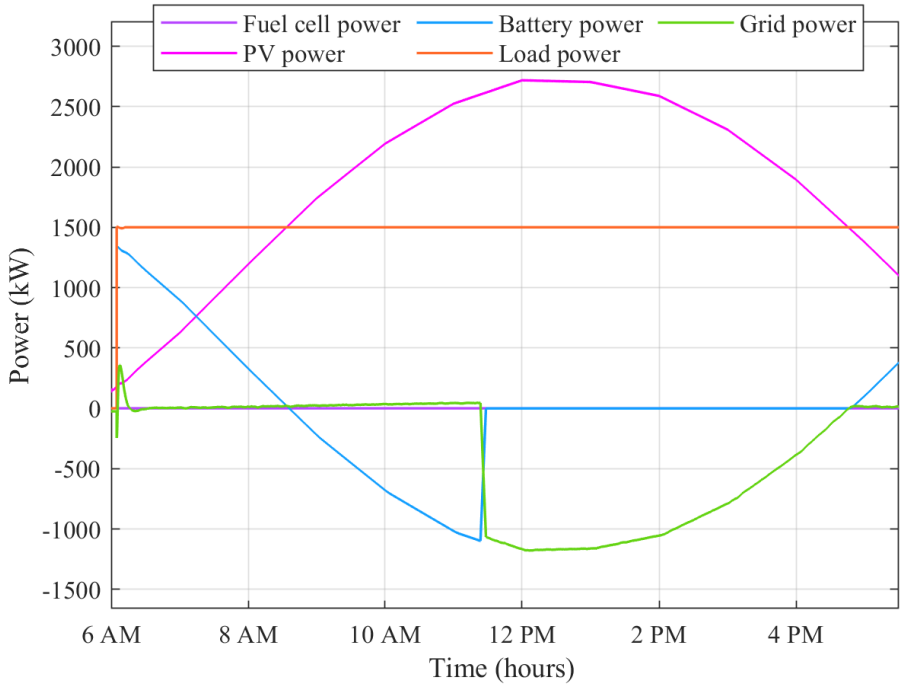

(a)

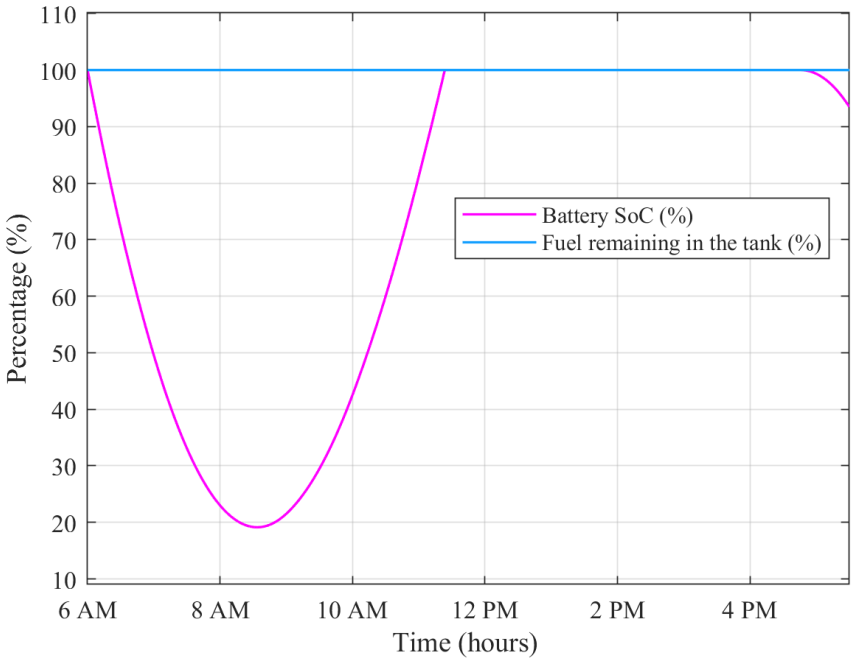
110
100
90
80
70
60
50
40
30
20
10
Percentage (%)
Battery SoC (%)
Fuel remaining in the tank (%)
6 AM
8 AM
10 AM
12 PM
2 PM
4 PM
Time (hours)

(b)

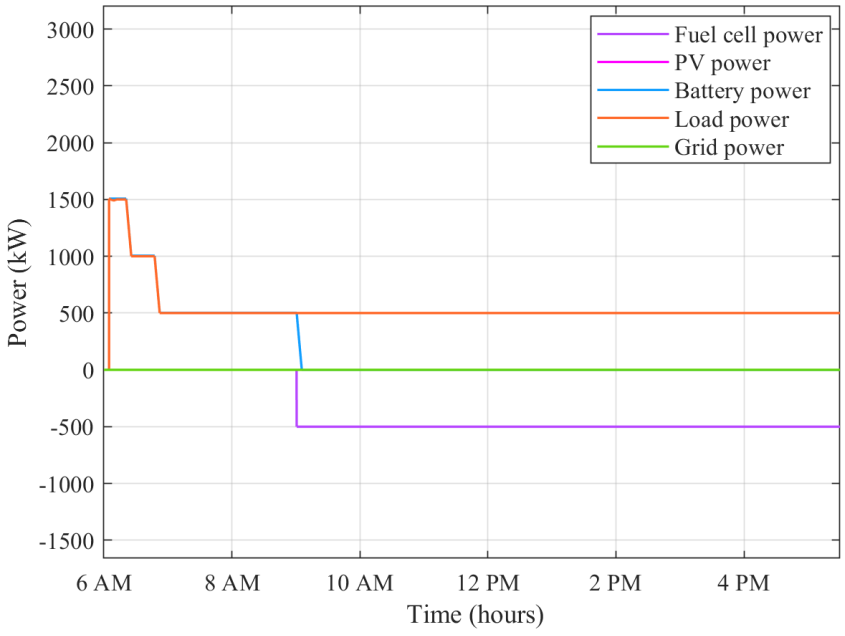
3000
2500
2000
1500
1000
500
0
-500
-1000
-1500
Power (kW)
Fuel cell power
PV power
Battery power
Load power
Grid power
6 AM
8 AM
10 AM
12 PM
2 PM
4 PM
Time (hours)

(c)

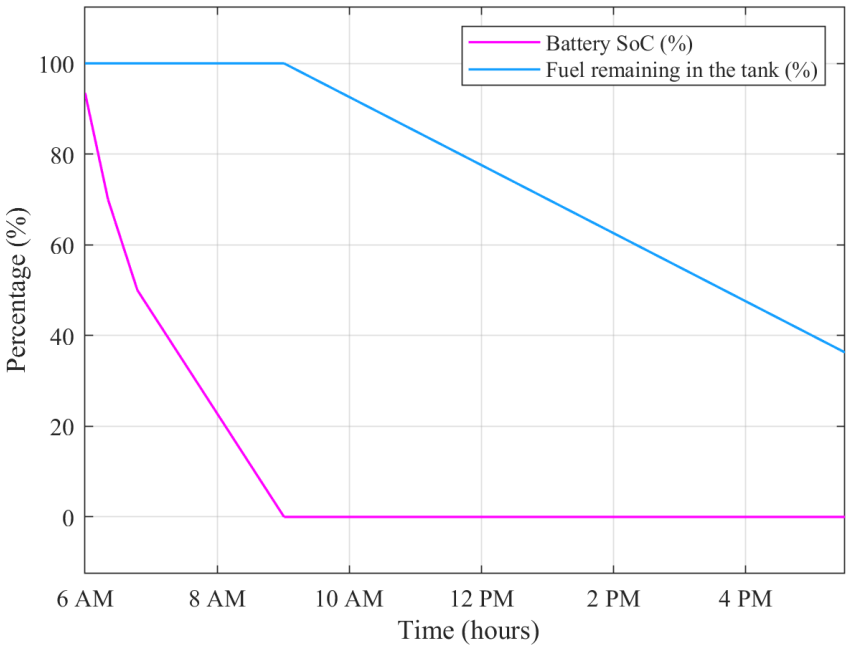

(d)

Figure 4-13 Results for the sunny day scenario. (a) Power supply and consumption during the morning, (b) battery SoC and fuel percentage during the morning, (c) power supply and consumption during the night, and (d) battery SoC and fuel percentage during the night.

Secondly, the transmission level energy management system (TL-EMS) is validated also on the IEEE 10-bus system, which is assumed to consist of five different areas: three areas with black start capability (BSAs) and two areas with non-black start capability (generator based, NBSAs). The TL-EMS initially entered the black start mode to determine the optimal combination of BSAs to support and start up the generators in the NBSAs. The minimum-impedance path for this process is illustrated in Figure 4.14, and the specifications of the two generators are described in Table 4.6.

Table 4-9 Data of generator characteristics.

Gen.	$\mathbf{T}_{crank}$ (hr)	$\mathbf{T}_{gcmin}$ (hr)	$\mathbf{T}_{gcmax}$ (hr)	R_r (MW/hr)	P_{crank} (MW)	P_{max} (MW)
G1	0:20	N/A	N/A	24	2	20
G2	0:30	N/A	N/A	50	5	40

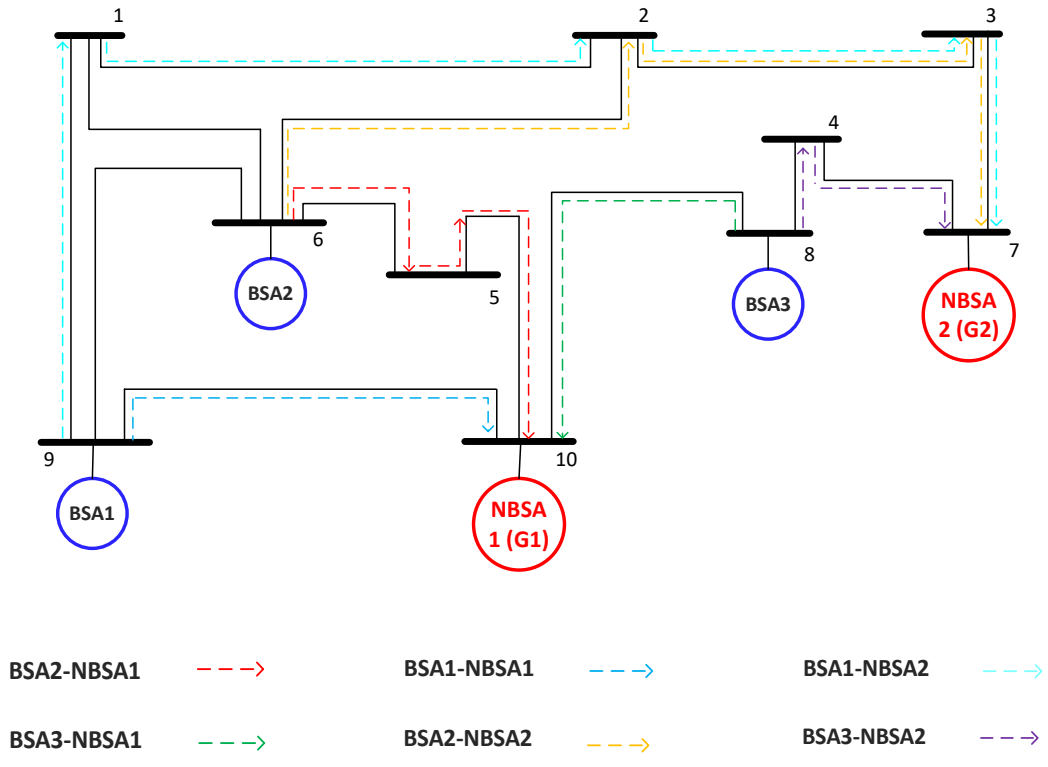

Figure 4-14 Minimum-impedance path determination using Dijkstra's algorithm for black start restoration between BSAs and NBSAs for IEEE-10 bus standard system.

The optimization algorithm at the transmission level controller identifies the optimal sequence to start generator G2 first, followed by generator G1. For G2, the best support is from BSA3. Figures 4.15 (a) and 4.15 (b) illustrate the support from BSA3 and the remaining fuel percentage in the tank and battery SoC after starting G2, respectively. No fuel is used, and no loads are disconnected to support the black start of G2. For G1, the minimum-impedance route involves support from BSA1 and BSA3. However, BSA1 is assumed to face shading effects, resulting in zero surplus power instead of 0.2 (this assumption is made to validate the proposed method against uncertainty in renewable energy generation). Consequently, PV power is sourced from areas 2 and 3, with battery stored power continuing to support the deficiency in the cranking power required for G1. Figures 4.16 (a) and 4.16 (b) show that no fuel or load disconnection is needed during the start of G1. These additional scenarios on the IEEE 10-bus system validate the effectiveness of the proposed energy management system (DL-EMS and TL-EMS) under various conditions. The results of these tests are illustrated in the mentioned figures, demonstrating the system's operational performance.

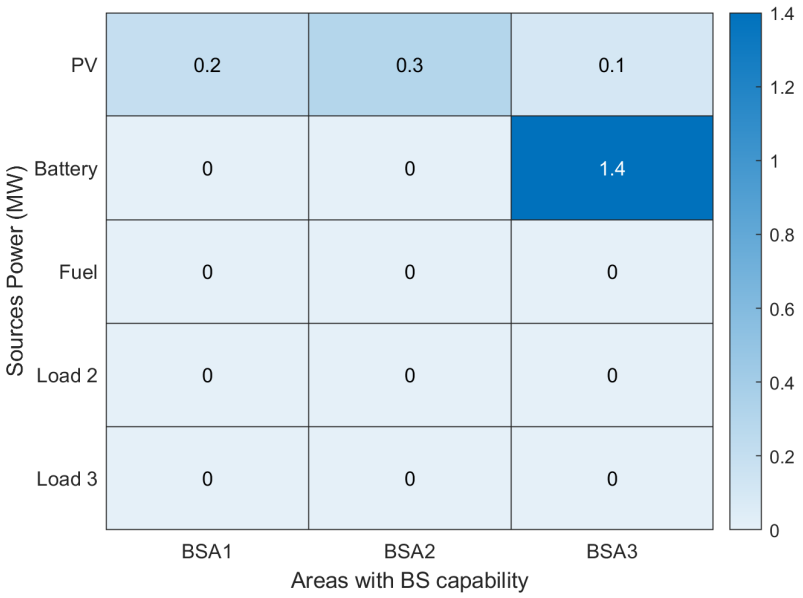

(a)

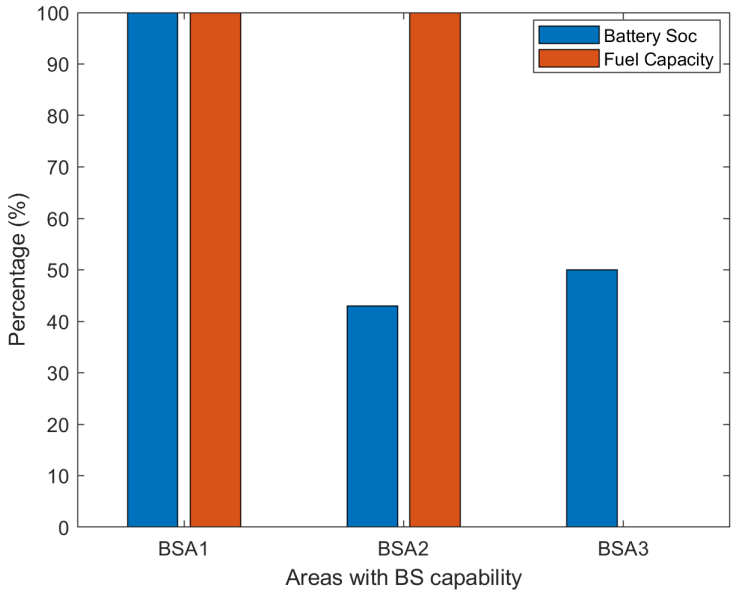

(b)

Figure 4-15 Information received from BSAs: (a) Optimal power allocation for G2 start-up from BSAs, (b) SoC and fuel percentage post-cranking for G2.

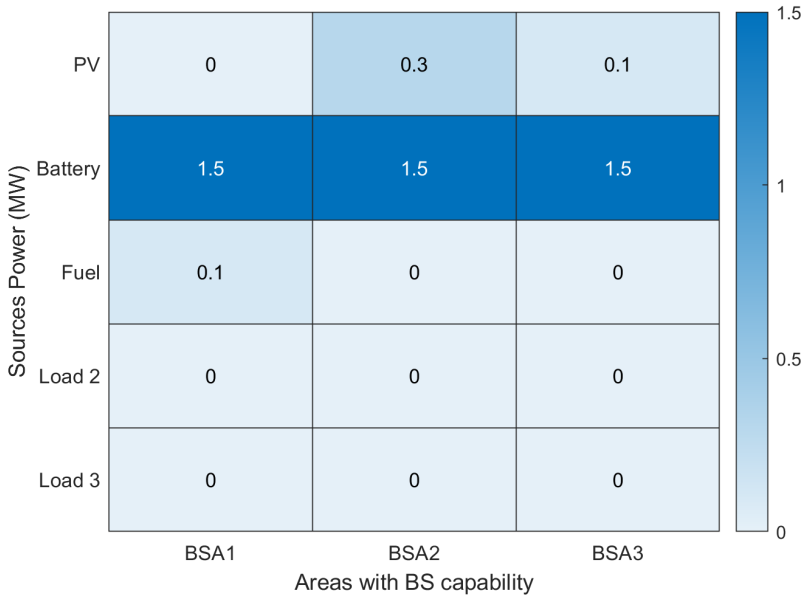

(a)

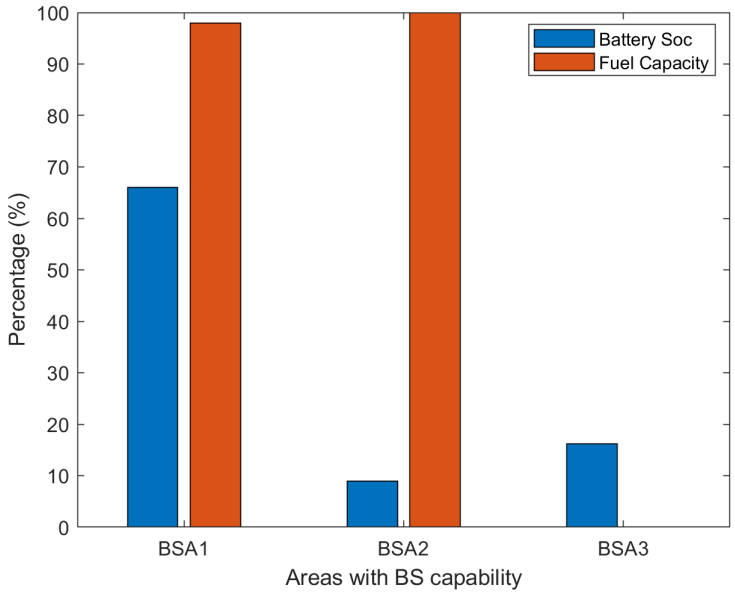

(b)

Figure 4-16 Information received from BSAs: (a) Optimal power allocation for G1 start-up from BSAs, (b) SoC and fuel percentage post-cranking for G1.

Finally, the proposed TL-EMS is comprehensively validated for computational time required by the optimization algorithm across different IEEE bus systems, including the IEEE 10-bus,

IEEE 30-bus, IEEE 39-bus, and IEEE 118-bus systems. The primary objective is to assess the scalability and efficiency of the algorithm when applied to power systems of varying complexity and size. Results are shown in Figure 4.17, which indicates that computational time increases with the size and complexity of the bus system, with the IEEE 10-bus system requiring 0.72 seconds and the IEEE 118-bus system requiring 5.32 seconds. This computational time is not comparable to the 1 to 5 hour time frame typically required for the black start process. Therefore, this trend demonstrates the algorithm's scalability and its ability to handle more extensive and complex power systems within a reasonable time frame.

These additional validations and analyses significantly provide a more comprehensive demonstration of the proposed energy management system's effectiveness.

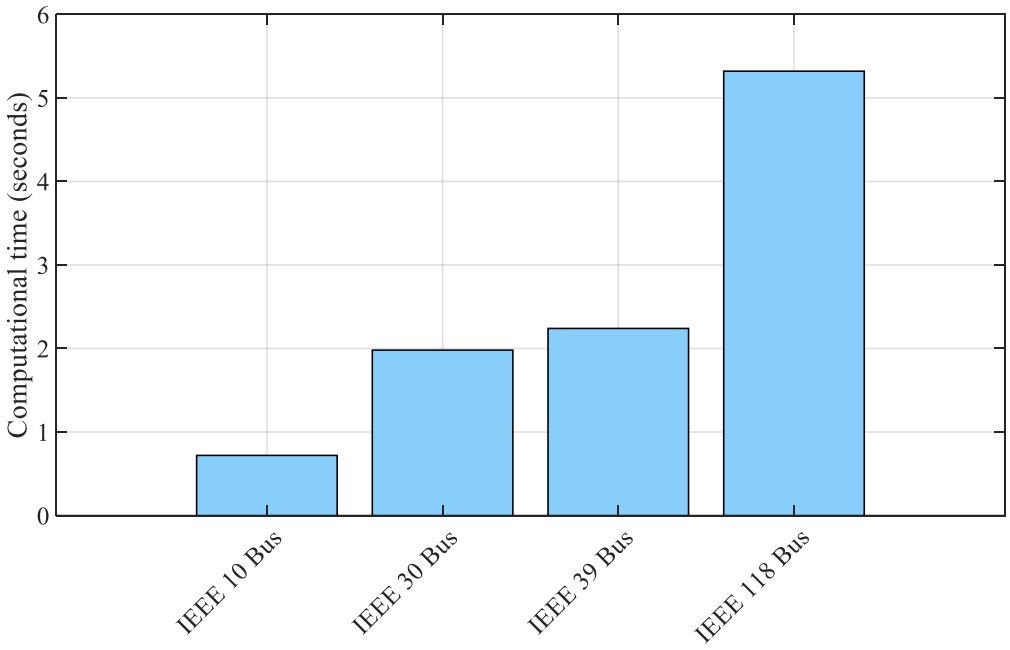

Figure 4-17 Computational time for optimization algorithm across various IEEE bus systems.

4.7. Summary

The key outcomes and results were demonstrated the superior performance of the proposed system in optimising load shedding, system inertia, and renewable energy utilisation during black start events. This was validated first using the IEEE 39-Bus test network then IEEE 10-Bus test network for further demonstrate its effectiveness. The hierarchical control structure, with coordination between distribution and transmission controllers, effectively manages the complex interactions between black start-capable and non-black start-capable areas. It restored essential loads in capable areas first before extending aid to neighbouring areas. The detailed

analysis of the multi-area power network architectures provided valuable insights for enhancing power restoration processes, while the innovative objective function, which prioritised renewable energy sources such as solar power, enabled greater integration of sustainable generation into the restored network. This comprehensive framework represented a significant advancement in energy management systems.

Chapter 5 A Frequency and Power Dependent Virtual Dynamic Inertia Damping Method for Grid Forming Converters

This chapter proposes a novel strategy to enhance frequency dynamics in grid-forming converters through a virtual inertia and adaptive damping mechanism. Unlike conventional damping approaches that rely on static parameters or single-variable measurements such as frequency or RoCoF alone, the method developed in this chapter derives a new mathematical relationship that couples dynamic inertia to both real-time frequency deviation and active power variation simultaneously. This dual-dependency is formulated as an add-on controller that integrates directly into the standard droop control loop, requiring no structural modification to the existing converter architecture. The focus is on formulating a dynamic control model that modulates virtual inertia in response to real-time changes in system frequency and active power.

5.1. Proposed Damping Method Structure

The proposed method is grounded on the concept that inertia can be dynamically adjusted based on frequency variations. It enhances the stability and damping performance of grid-forming converters in weak grids.

A. Theoretical Derivation of Dynamic Inertia

In power systems, the inertia constant M reflects the system's ability to resist changes in frequency. Traditionally, it is related to the angular frequency ω and the rate of change of active power Δp (in per unit) as follows:

$$M = \frac{\Delta P(t)}{\left(\frac{d\omega(t)}{dt}\right)} \tag{5.1}$$

where, $\frac{d\omega(t)}{dt}$ is the rate of change of angular frequency $\omega(t)$, and M is the inertia constant. $\Delta P(t)$ is the change in active power output. However, this formula can lead to numerical issues when $\frac{d\omega}{dt}$ approaches zero, leading to potential stability issues in scenarios with low dynamic conditions.

The time derivative of angular frequency in the denominator of (5.1) is replaced with a finite

difference approximation from the nominal angular frequency ω_0 over a small time step Δt as follows:

$$M = \frac{\Delta P(t)}{\omega(t) - \omega_0} \Delta t \tag{5.2}$$

Hence, $\Delta P(t)$ is computed as a backward difference using $\Delta P(t) = P(t) - P(t - \Delta t)$. The resulting signal is passed through a low-pass filter to attenuate high-frequency noise. To further analyze the impact of small frequency changes on inertia, the inertia constant M is considered to vary with the angular frequency $\omega(t)$. This means that $M(\omega)$ is not a fixed value but changes as the frequency changes. Consequently, the inertia is calculated at two closely spaced frequency points, namely, $\omega(t)$ and $\omega(t) + \Delta\omega$. The inertia at these two points can be expressed as:

$$M_1 = \frac{\Delta P(t)}{\omega(t) - \omega_0} \Delta t \tag{5.3}$$

$$M_2 = \frac{\Delta P(t)}{\omega(t) - \omega_0 + \Delta\omega} \Delta t \tag{5.4}$$

To determine the rate of change of inertia with respect to frequency, denoted as $M'(\omega)$, the limit as $\Delta\omega$ approaches zero is considered:

$$M'(\omega) = \lim_{\Delta f \to 0} \left[\frac{M_2 - M_1}{\Delta\omega} \right] \tag{5.5}$$

Substituting (5.3) and (5.4) into (5.5) yields:

$$M'(\omega) = \Delta t \Delta p \lim_{\Delta\omega \to 0} \left[\frac{-1}{(\omega(t) - \omega_0)(\omega(t) - \omega_0 + \Delta\omega)} \right] \tag{5.6}$$

By simplifying this expression, the derivative of inertia with respect to frequency is obtained as:

$$M'(\omega) = -\Delta t \Delta P(t) \frac{1}{(\omega(t) - \omega_0)^2} \tag{5.7}$$

This result reveals that the rate of change of the synthetic inertia is inversely proportional to the square of the frequency deviation. Consequently, as the frequency deviation approaches zero, the control law becomes increasingly sensitive, potentially leading to singularity issue, a behavior that should be addressed to ensure numerical stability and reliable implementation in practice.

B. Regularized Control Law and Practical Implementation

To address the singularity issue and ensure stable and bounded controller behaviour, the proposed method incorporates a mathematically rigorous and practically robust regularisation approach.

- **Regularization of the Inertia Control Law**

To eliminate the singularity at $\omega = \omega_0$, a regularization term ε^2 is introduced into the denominator of (5.7). The modified, regularized control law becomes:

$$M'(\omega) = -\Delta t \cdot \Delta P(t) \cdot \frac{1}{(\omega(t) - \omega_0)^2 + \varepsilon^2} \tag{5.8}$$

This formulation ensures that the denominator is strictly positive and continuously differentiable for all values of ω. Specifically,

$$(\omega(t) - \omega_0)^2 + \varepsilon^2 \geq \varepsilon^2 > 0 \quad \forall \omega \in \mathbb{R} \tag{5.9}$$

As a result, the control signal $M'(\omega)$ is guaranteed to remain finite and smooth across the entire frequency range. The limiting behavior as $\omega \to \omega_0$ is given by:

$$\lim_{\omega \to \omega_0} M'(\omega) = -\Delta t \cdot \frac{\Delta P(t)}{\varepsilon^2} \tag{5.10}$$

As the power imbalance Δp naturally converges to zero in steady-state conditions, the control contribution vanishes $\lim_{t \to \infty} M'(\omega) = 0$. This ensures that the controller does not introduce steady-state error and becomes inactive near equilibrium.To maintain compatibility with grid code requirements, the regularization parameter ε is selected based on the maximum allowable deadband for frequency-sensitive control. According to the GB grid code (CC.6.3.7(c)(iii)) [109], the maximum frequency deadband is ±0.015 Hz. Normalizing this with respect to a 50 Hz nominal system yields:

$$\varepsilon = \frac{0.015}{50} = 0.0003 \text{ p.u} \tag{5.11}$$

This regularized formulation provides inherent stability and robustness against chattering, even when the system operates near the equilibrium point where frequency deviations are small. Physically, the control action is driven by the product of the gain (the inverse squared frequency term) and the rate of change of active power (ΔP). In steady-state conditions, although the gain term may be large just outside the deadband, the numerator ΔP naturally vanishes (ΔP→0). This characteristic ensures that the total control output remains negligible. Furthermore, the regularization term ε² ensures the denominator is strictly positive and prevents singularity-driven noise amplification. When combined with the low-pass filtering of the power difference, this architecture guarantees that the control signal remains continuous and bounded. Consequently, it prevents severe chattering even in the presence of measurement noise or high controller gains.

- **Frequency Deadband Mechanism**

Moreover, to enhance robustness against measurement noise and small signal fluctuations, a deadband logic is employed. The controller is deactivated when the frequency deviation $|\omega - \omega_0|$ is smaller than a predefined threshold δ_{db}. The control law is thus defined as:

$$M'_{\text{db}}(\omega) = \begin{cases} -\Delta t \cdot \Delta P(t) \cdot \dfrac{1}{(\omega(t) - \omega_0)^2 + \varepsilon^2}, & \text{if } |\,\omega - \omega_0\,| \geq \delta_{\text{db}} \\ 0, & \text{if } |\,\omega - \omega_0\,| < \delta_{\text{db}} \end{cases} \tag{5.12}$$

For consistency and smooth transition, the deadband threshold is set equal to the regularization parameter ($\delta_{\text{db}} = \varepsilon = 0.0003$ p.u.). Moreover, this ensures that the controller remains inactive in a narrow neighbourhood around the nominal frequency, thereby avoiding control action due to noise or negligible deviations.

- **Sampling Interval Selection (Δt) and Its Impact**

The sampling interval Δt plays a pivotal role in determining both the control accuracy and the dynamic responsiveness of the proposed method. To ensure that the control algorithm can capture and respond effectively to fast transients in low-inertia power systems, a high sampling frequency of 100 kHz is employed. This corresponds to a sampling interval of $\Delta t = \frac{1}{f_s} = \frac{1}{100{,}000} = 10^{-5}$ s. This time step is intentionally chosen to be two orders of magnitude smaller

than the fastest relevant dynamic time constant encountered in converter-dominated grids, which is typically on the order of $\tau_{\text{grid}} \approx 10^{-3}$ s [110]. Here, τ_{grid} denotes the characteristic time constant associated with fast frequency dynamics in low-inertia power systems. Therefore, the temporal resolution of the control system is quantified by the following ratio:

$$\frac{\Delta t}{\tau_{\text{grid}}} = \frac{10^{-5}}{10^{-3}} = 10^{-2} \tag{5.13}$$

This small ratio ensures that the controller operates with sufficient resolution to emulate continuous-time behavior, minimizing the risk of aliasing or control delay. Additionally, the phase lag introduced by the sampling interval is negligible.

For instance, at a representative oscillation frequency of 1 Hz ($\omega = 2\pi$ rad/s), the phase lag introduced by the sampling process is $\phi_{\text{lag}} = -\frac{\omega \cdot \Delta t}{2} \approx -0.0018°$. Such a minimal lag confirms that the chosen sampling interval provides excellent temporal resolution and effectively preserves the fast-response characteristics of the proposed damping controller.

To integrate the dynamic inertia model into the droop controller, the cumulative effect of the change in inertia over time is considered. The change in inertia $M'(\omega)$ is integrated to produce a dynamic adjustment factor that evolves with frequency and active power variations. This integral is then added to the phase angle θ, which is derived from the active power control loop of the droop controller. By incorporating the dynamic inertia adjustments directly into the control mechanism, the system benefits from a more responsive and adaptive control framework. Fig. 5.1 illustrates the detailed control structure, where the traditional droop controller (blue region) is augmented by the proposed add-on dynamic inertia controller (red region). The operation of the add-on controller proceeds as follows: First, the change in active power output ΔP is calculated and processed through a low-pass filter (LPF) with a cut-off frequency ω_c to attenuate high-frequency measurement noise. Simultaneously, the squared frequency deviation $(\omega - \omega_0)^2$ is computed and summed with the regularization term ε^2 to ensure numerical stability. The filtered power signal is then divided by this regularized frequency term, resulting in the instantaneous rate of change of inertia, $M'(\omega)$. To allow for precise tuning of the damping intensity, this signal is modulated by a gain factor k (where $0 \leq k \leq 1$). The resulting weighted signal is passed through an integrator to derive the cumulative dynamic inertia adjustment, M. Finally, this adjustment is added to the phase angle θ generated by the traditional droop loop. Crucially, to prevent unnecessary control action during normal

steady-state operation, the proposed add-on controller (red region) is only activated if the absolute frequency deviation $|\omega - \omega_0|$ exceeds the defined deadband limit δ_{db}. If the deviation is within the deadband, the output of the add-on loop remains zero, and the system operates solely under traditional droop control. This dynamic behaviour ensures that the system response is appropriately scaled based on the magnitude of frequency and active power deviations.

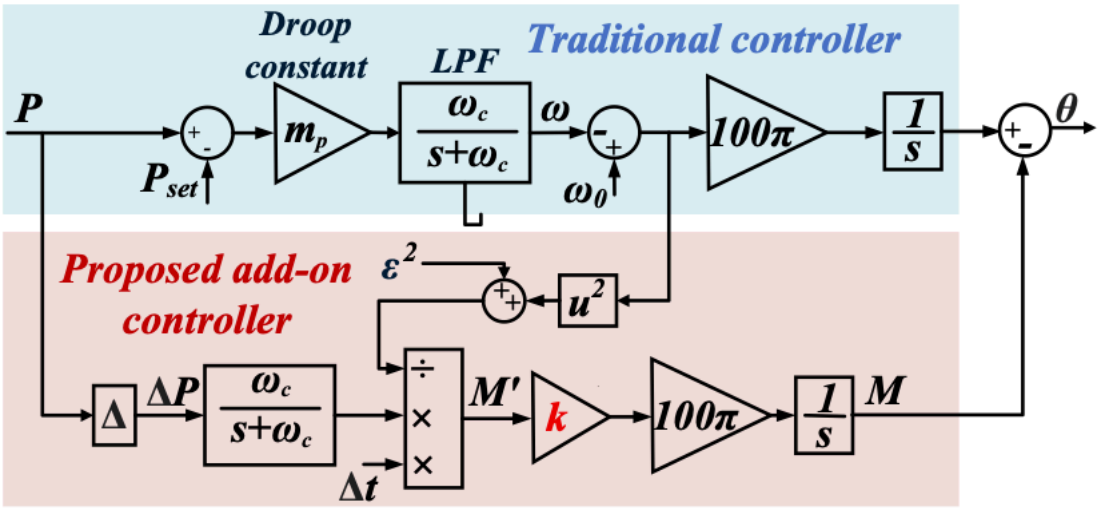

Figure 5-1: Integration of the proposed add-on controller within the traditional droop control loop.

5.2 System Performance and Stability Analysis

This section examines the performance and stability of the system under the proposed add-on controller. Disturbances are introduced to analyse the system response, with particular focus on the controller's impact on damping, frequency stability, and transient behaviour. The analysis is conducted using Bode diagrams, phase portraits, equilibrium points, and small-signal stability assessments. The results provide insights into the controller effectiveness in improving system stability across varying gain values.

5.2.1. Frequency Response Analysis

The Bode diagrams presented in Figures 5.2 and 5.3 offer a comprehensive analysis of the proposed add-on controller performance across a range of gain values (K). The magnitude response of the system is shown in Figure 5.2. The blue line represents the system without the proposed controller ($K = 0$). As the gain increases from $K = 0.2$ to $K = 1$, the response curves shift, indicating the controller's impact. The controller significantly reduces the system gain in the frequency range of 1 to 1000 Hz. This reduction in gain is crucial as it signifies enhanced

damping, which helps in stabilising the system by mitigating oscillations and improving transient response. The phase response of the system is depicted in Figure 5.3. Without the proposed controller ($K = 0$), the phase shift is approximately 90º. Increasing the gain from $K = 0.2$ to $K = 1$ causes the phase shift to approach 180º within the frequency range of 1 to 1000 Hz. This phase shift indicates that the output of the active power control loop becomes out of phase with the system inertia, effectively counteracting changes in active power. This counteraction is a critical aspect of the proposed controller, as it contributes to the system ability to dampen fluctuations and maintain stability.

5.2.2. Phase Portrait Analysis of System Dynamics

Figure 5.4 presents a phase portrait analysis to demonstrate the system dynamic response to load changes. The trajectories represent the system behaviour when a step load of 50 MW is added or removed. Without the proposed controller ($K = 0$, blue trajectory), the system exhibits significant oscillations and takes longer to settle. With the proposed controller and $K = 0.4$ (red trajectory), the system shows improved damping, reduced oscillations, and faster settling time. For $K = 1$ (green trajectory), the system demonstrates superior performance with minimal oscillations and rapid stabilization. These results highlight the effectiveness of the proposed controller in improving the system dynamic response.

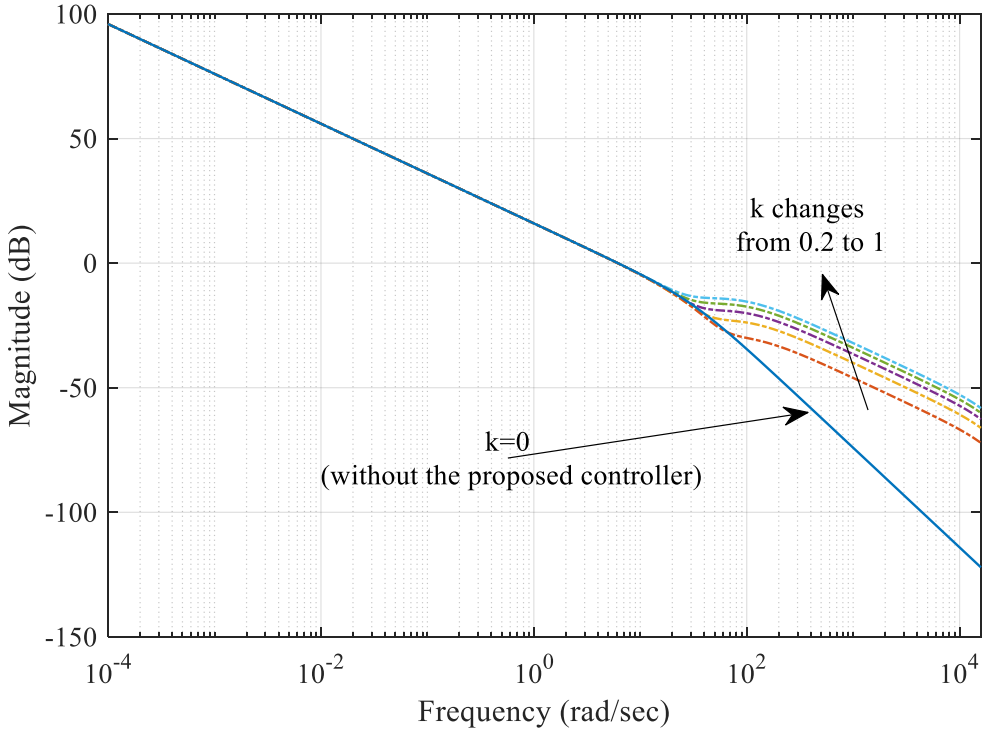

Figure 5-2: Magnitude response of the system with varying gain K.

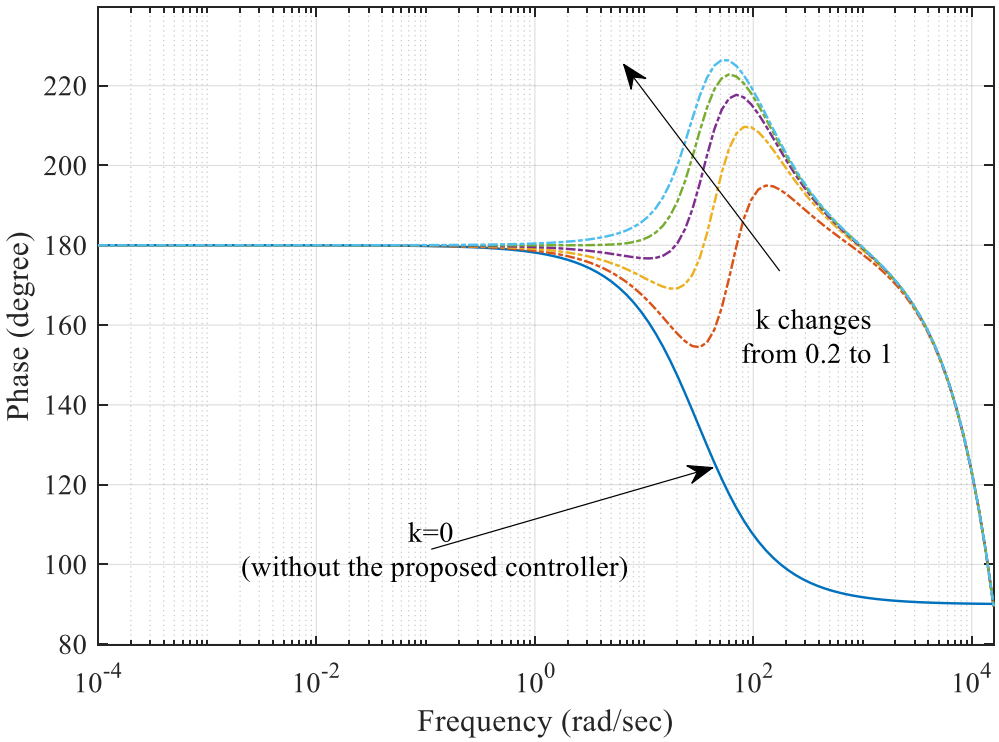

Figure 5-3: Phase response of the system with varying gain K.

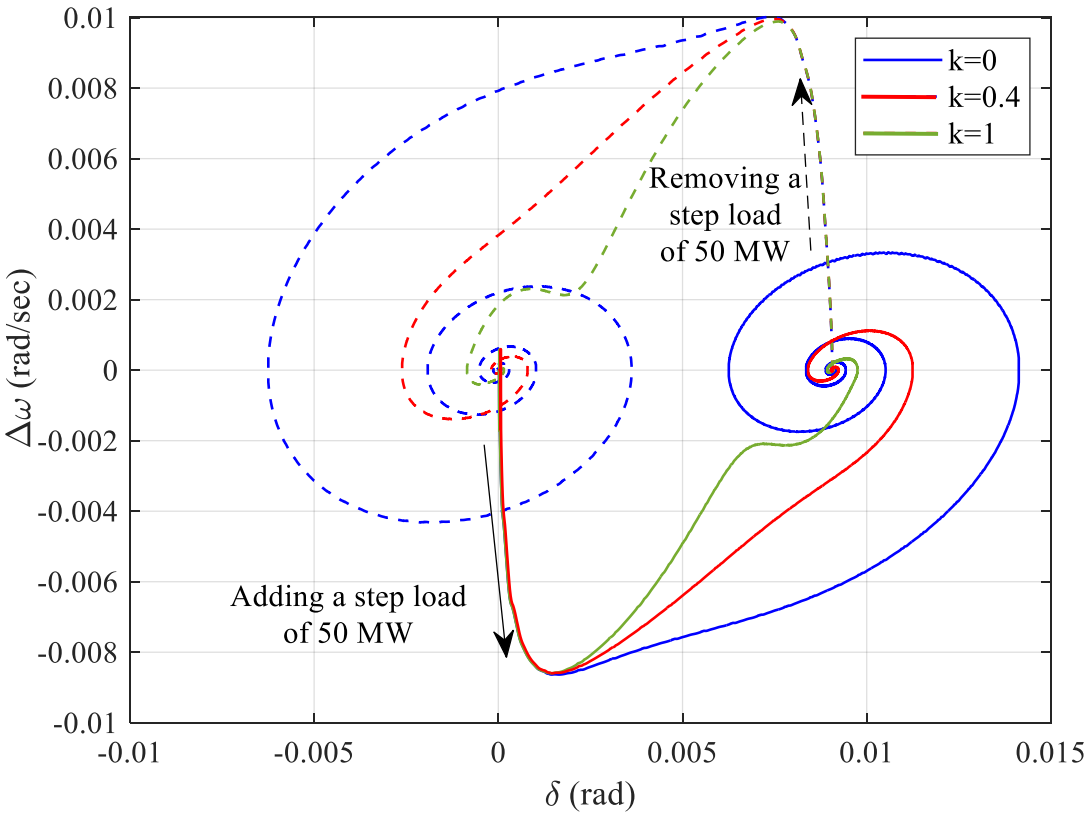

Figure 5-4: Phase portrait analysis of system dynamics with varying gain K.

Table 5-1: System Parameters

Parameter	Definition	Value
P_n^{GIC1}	Nominal power for CIG1	247.5 MVA
P_n^{GIC2}	Nominal power for CIG2	192 MVA
P_n^{GIC3}	Nominal power for CIG3	128 MVA
ω_0	Nominal grid angular frequency	2π × 50 rad/s
V_n	Nominal Grid voltage	230 kV
P_1, Q_1	Active and Reactive power for load 1	90 MW, 30 MVAR
P_2, Q_2	Active and Reactive power for load 2	125 MW, 50 MVAR
P_3, Q_3	Active and Reactive power for load 3	100 MW, 35 MVAR

5.2.3. Equilibrium Point Analysis

The equilibrium points of the system are determined by analysing the governing equations under steady-state conditions, where the time derivatives of the state variables are equal to zero. This analysis provides valuable insights into the long-term behaviour and stability of the system. The modified frequency expression is derived by combining the traditional droop law with the proposed add-on controller output from Figure 5.1. The traditional droop controller produces:

$$\omega_{droop} = \left(\omega_0 - m_p(p(\delta) - p_{set})\right) \tag{5.14}$$

From the add-on controller block diagram, the controller output is:

$$\omega_{addon} = \left(\frac{\Delta p(\delta) * k}{\Delta w^2}\right) \tag{5.15}$$

where $\Delta\omega = \omega_0 - m_p$ (P(δ) − p_{set})is the frequency deviation produced by the droop loop and Δp (δ) is the filtered active power deviation. The total frequency is the droop output minus the add-on correction:

$$\omega = \left(\omega_{droop} - \omega_{addon}\right) \tag{5.16}$$

Substituting (5.14) and (5.15):

$$\omega = \left(\omega_0 - m_p(p(\delta) - p_{set})\right) - \frac{\Delta p(\delta) * k}{\left(\omega_0 - m_p(p(\delta) - p_{set})\right)^2} \tag{5.17}$$

where $\Delta p(\delta)$ represents the active power as a function of the power angle δ, m_p is the droop coefficient, p_{set} is the reference active power, and ω_0 is the nominal angular frequency.

The state variables are defined as $x_1 = \delta$ and $x_2 = \Delta\omega$. The first state equation describes the rate of change of power angle:

$$\frac{dx_1}{dt} = \omega - \omega_g = x_2 + \omega_0 - \omega_g \tag{5.18}$$

For the second state equation, the active power transferred through the grid reactance X_g is:

$$p(\delta) = \frac{3\, V_g V_{PCC} \sin(\delta)}{2X_g} \tag{5.19}$$

Taking the time derivative of Equation 5.17 and substituting the power-angle relationship, the rate of change of frequency deviation becomes:

$$\frac{dx_2}{dt} = \frac{-(3\, V_g V_{PCC} \cos(\delta))}{(2X_g)(m_p + \omega_0^2 k)(x_2 + \omega_0 - \omega_g)} \tag{5.20}$$

This is obtained by linearising around the equilibrium point δ_0 where $\sin(\delta_0) \approx \sin(\delta_0) + \cos(\delta_0)\cdot\delta_0$.

$$\begin{bmatrix} \frac{dx_1}{dt} \\ \frac{dx_2}{dt} \end{bmatrix} = \begin{bmatrix} x_2 + \omega_0 - \omega_g \\ \frac{-3\, V_g V_{PCC} \cos(\delta_0)}{2X_g}\left(m_p + \omega_0^2 k\right)\left(x_2 + \omega_0 - \omega_g\right) \end{bmatrix} \tag{5.21}$$

where V_g and V_{PCC} are the grid voltage and point of common coupling voltage, respectively, X_g is the grid reactance, δ_0 is the equilibrium value of the power angle, and ω_g is the grid angular frequency. The equilibrium point is achieved when the time derivatives of the state variables are zero, $\frac{dx_1}{dt} = 0$ and $\frac{dx_2}{dt} = 0$. Solving these conditions yields the equilibrium frequency deviation:

$$x_2 = \Delta\omega_e = \omega_g - \omega_0 \tag{5.22}$$

where ω_e is the internal GFC estimated frequency ω but at the equilibrium point. At equilibrium, the change in active power $\Delta p(\delta)$ is zero, and the GFC frequency ω equals the grid frequency ω_g.

The steady-state operating point is obtained by setting the time derivatives of both state variables to zero in the state-space model:

Step 1: Setting $\frac{dx_1}{dt} = 0$:$x_2 + \omega_0 - \omega_g = 0 \rightarrow x_2 = \omega_g - \omega_0$

This means at steady state, the frequency deviation Δω equals the difference between grid frequency and nominal frequency.

Step 2: Setting $\frac{dx_2}{dt} = 0$: This requires the second equation to equal zero. Since $x_2 + \omega_0 - \omega_g = 0$ from Step 1, the frequency deviation term vanishes. The remaining condition requires the power balance to be satisfied at the equilibrium angle δ_0.

Step 3: Substituting the power transfer equation P(δ₀) = (3 $V_g V_{PCC} \sin(\delta_0)$) / ($2X_g$) into the original droop law $\omega = \omega_0 - m_p\ (p - p_{ref})$ and setting $\omega = \omega_g$at steady state gives:

$$\omega_g = \omega_0 - m_p \left(\frac{3}{2} \frac{V_g V_{PCC} \sin(\delta_e)}{X_g} - p_{ref} \right) \tag{5.23}$$

This is simply the droop equation evaluated at the equilibrium point, confirming that the steady-state frequency is determined solely by the droop characteristic and is independent of the proposed controller gain K, since the add-on controller term contains $\Delta\omega^2$ in its denominator, which equals zero at steady state.

The equation in (5.23) represents the steady state equations of the system. These equations reveal that the equilibrium points are independent of the controller gain k. This independence highlights that the proposed add-on controller does not alter the system equilibrium state but instead improves its dynamic response and stability characteristics.

5.2.4. Small-Signal Stability Analysis

This section presents the small-signal stability analysis of the proposed dynamic inertia controller. The objective is to assess the system's ability to return to equilibrium following small perturbations. The analysis is carried out by linearizing the nonlinear dynamic equations around the steady-state operating point, resulting in a state-space model that captures the local behaviour of the system. Let the state variables be defined as $x_1 = \delta, x_2 = \Delta\omega = \omega - \omega_0$. The

rate of change of the power angle δ is given by $\frac{dx_1}{dt} = x_2 + \omega_0 - \omega_g$. To capture the dynamic behavior of the frequency regulation loop, a low-pass filter is incorporated in the controller structure. The filtered frequency deviation is governed by:

$$\tau_f \cdot \frac{dx_2}{dt} + x_2 = \Delta\omega_{ss} = -K_{sys} \cdot \Delta\delta \tag{5.24}$$

where $\tau_f = \frac{1}{\omega_c}$ is the filter time constant, and K_{sys} is the composite system gain defined as:

$$K_{sys} = \frac{3V_g V_{PCC}\cos(\delta_0)}{2X_g}\left(m_p + \frac{k}{g^2(\delta_0)}\right) \tag{5.25}$$

With $g(\delta_0) = \omega_0 - m_p(p(\delta_0) - p_{ref})$, substituting and rearranging the Jacobian matrix equations for the linearized state-space model yields:

$$J = \begin{bmatrix} \frac{\partial \dot{x}_1}{\partial x_1} & \frac{\partial \dot{x}_1}{\partial x_2} \\ \frac{\partial \dot{x}_2}{\partial x_1} & \frac{\partial \dot{x}_2}{\partial x_2} \end{bmatrix} = \begin{bmatrix} 0 & 1 \\ -\frac{1}{\tau_f}(K_{sys}) & -\frac{1}{\tau_f} \end{bmatrix} \tag{5.26}$$

The characteristic equation of the system is:

$$\lambda^2 + \frac{1}{\tau_f}\lambda + \frac{K_{sys}}{\tau_f} = 0 \tag{5.27}$$

This represents a second-order system. The necessary and sufficient condition for local asymptotic stability is that all coefficients of the characteristic polynomial are strictly positive. Since $\tau_f > 0$ by definition, the system is stable if and only if $K_{sys} > 0$. Substituting the expression for K_{sys} and assuming $\cos(\delta_0) > 0$(valid for typical power angles), the stability condition reduces to:

$$m_p + \frac{k}{g^2(\delta_0)} > 0 \tag{5.28}$$

Given that the nominal frequency ω_0 is set to 1 in the per-unit system as a reference, the most conservative case for stability occurs when the term $g(\delta_0)$ approaches unity. This condition arises when the steady-state power output closely matches the reference power, i.e., $p(\delta_0) \approx p_{ref}$, yielding:

$$k_{critical} > -m_p \tag{5.29}$$

To validate the small-signal stability analysis, the system response under various values of the controller gain k is plotted for a droop coefficient of $m_p = 0.02$, as shown in Figure 5.5. The figure demonstrates how the system stability is influenced by the choice of k. For $k < k_{critical}$ as $k = -1$ or $k = -0.02$, the system exhibits instability or marginal stability, respectively. However, for $k > k_{critical}$, as in the cases of $k = 0.02$ or $k = 1$, the system achieves stable behavior, with the oscillations damping out over time. This supports the theoretical condition derived for the critical gain.

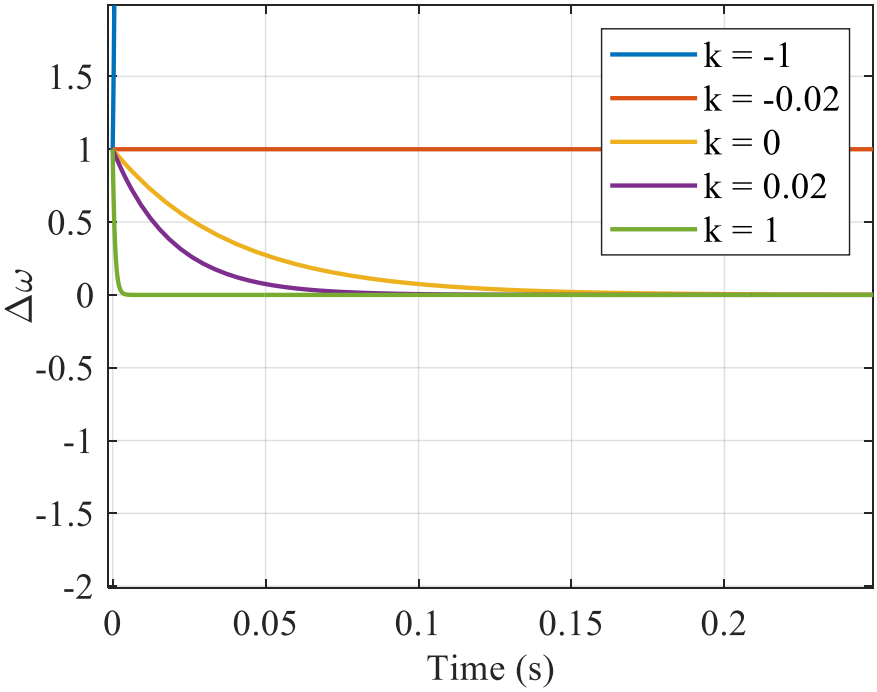

Figure 5-5: System response ($\Delta\omega$) over time for different values of the controller gain k at a droop coefficient $m_p = 0.02$.

5.2.5. Gain Design Constraints for Stability and Robustness

While the lower bound on gain k is dictated by the small-signal stability condition derived in (5.23), the upper bound is determined by robustness considerations, particularly the effect of measurement noise on the controller output. The proposed control law includes a term based on the backward difference of active power ($\Delta P[n] = P[n] - P[n-1]$). This operation behaves like a high-pass filter, which can amplify high-frequency noise in the measured power signal.

To assess the impact of measurement noise on the controller's performance, the measured active power signal at discrete time step n is modeled as:

$$P[n] = \bar{P}[n] + \eta[n], \quad \eta[n] \sim \mathcal{N}(0, \sigma_p^2) \tag{5.30}$$

where, $\bar{P}[n]$ represents the true noise-free active power, while $\eta[n]$ denotes zero-mean white Gaussian noise with variance σ_p^2, reflecting sensor inaccuracies or quantization effects in digital measurement systems. Because the proposed dynamic inertia controller operates on the backward difference of the power signal, it is sensitive to high-frequency components. This leads to the following expression for the noise-induced component in the frequency reference:

$$\widetilde{\omega}_{\text{noise}}[n] = -k \cdot (\eta[n] - \eta[n-1]) \tag{5.31}$$

where k is the inertia gain. Assuming that the noise samples $\eta[n]$ and $\eta[n-1]$ are uncorrelated (a valid assumption for white noise), the variance of the resulting frequency jitter can be derived as:

$$\sigma_\omega^2 = 2k^2\sigma_p^2 \Rightarrow \sigma_\omega = k\sqrt{2} \cdot \sigma_p \tag{5.32}$$

Here, σ_ω denotes the standard deviation of the noise-induced frequency fluctuation. To ensure robust operation and avoid excessive jitter in the frequency reference, it is essential to limit σ_ω below a pre-defined threshold. A commonly accepted maximum value for frequency jitter is $\sigma_{\omega,\max} = 0.0015$ p.u., which corresponds to a phase angle deviation of less than 0.5 electrical degrees per control cycle. This constraint imposes an upper bound on the allowable gain k, given by:

$$k \leq \frac{\sigma_{\omega,\max}}{\sqrt{2} \cdot \sigma_p} \tag{5.33}$$

Combining the lower bound from (5.29) and the upper bound from (5.33), we obtain the complete safe and effective design interval for the gain k:

$$-m_p < k \leq \frac{\sigma_{\omega,\max}}{\sqrt{2} \cdot \sigma_p} \tag{5.34}$$

Assuming a representative sensor noise level of $\sigma_p = 0.001$ p.u., the upper bound for the inertia gain becomes $k_{\max} \approx \frac{0.0015}{\sqrt{2} \cdot 0.001} \approx 1.06$. Thus, this value defines the maximum

permissible gain under typical measurement conditions. Therefore, for $m_p = 0.02$, the practical range becomes $-0.02 < k \leq 1.06$.

5.3. Results and Discussion

This section presents the validation of the novel dynamic inertia damping controller applied to the IEEE 9-bus system, with its parameters are detailed in Table 5.1. This 9-bus system comprises three interconnected areas with three CIGs, serves as grid-forming converters, as shown in Figure 5.6. The validation is assessed through two specific case studies: a 50 MW step load and a transmission line disconnection. The validation process employs the PLECS platform, which facilitates real-time simulation by integrating system-level components such as transformers, generators, transmission lines, loads, and buses. The real-time PLECS platform operates on 4 cores based on ARM Cortex-A53 processor at 1.5 GHz, as shown in Figure 5.7. This allows for a comprehensive evaluation of the controller performance across various scenarios, particularly focusing on its ability to enhance damping through dynamic inertia.

Three case studies are conducted to evaluate the effectiveness of the proposed dynamic inertia controller under representative disturbance scenarios. The first case study examines the system response to a large step load. The second case study considers a transmission line disconnection. The third case study provides a comparative assessment against state-of-the-art damping methods. Collectively, these studies confirm the controller's effectiveness in enhancing system stability and resilience under both local and system-level disturbances.

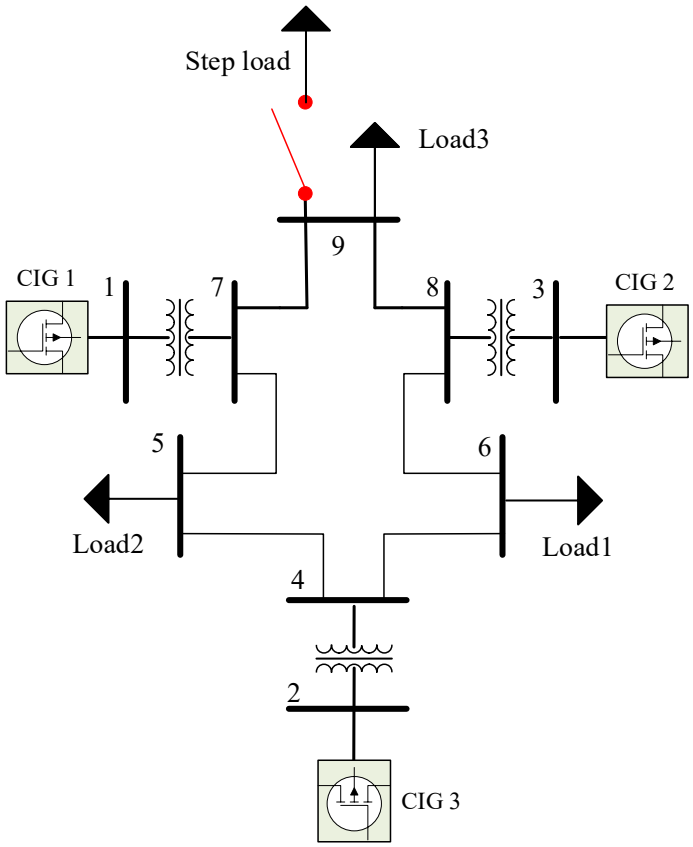

Figure 5-6: IEEE-9 Bus.

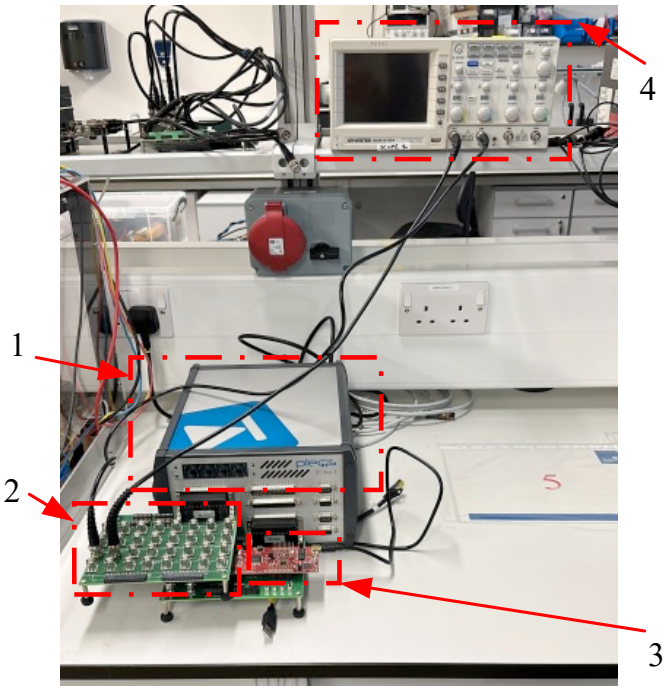

Figure 5-7: Control hardware-in-the-loop validation. 1) PLECS RT simulator, 2) Box breakout board (for input/output interface), 3) DSP, and 4) Oscilloscope.

Case Study 1: Response to a 50 MW Step Load

In the first case study, the system resilience to a sudden 50 MW step load at bus 9 is investigated. The dynamic inertia controller is tested at three different integration levels, represented by gain values K of 0, 0.4, and 1 to quantify its impact on the system damping and stability. Fig. 5.8 (a) describes the active power responses for grid-forming converter 1.

At $K = 0$, Figure 5.7 shows significant initial overshoot and prolonged oscillations, indicating a significant lack of damping which could lead to instability in large disturbance scenarios, as shown in Figure 5.8(a). The frequency experiences wide swings, indicating ineffective inertia response, which could compromise system reliability, as shown in Fig. 5.8(b). At $K = 0.4$, a noticeable attenuation in oscillation amplitude and quicker settling times are observed. This intermediate gain setting improves system response but does not fully optimise it, as shown in Figure 5.8(a). Moreover, there is a reduction in the frequency deviation range, suggesting enhanced control capabilities, as shown in Figure 5.8(b). In contrast at $K = 1$, the response curve is much smoother, with minimal overshoot and rapid stabilisation. This demonstrates that the full integration of the proposed controller maximises damping efficiency, showcasing the controller's potential to maintain stability even under significant load changes, as shown in Figure 5.8(b). Therefore, the system achieves near-optimal frequency stability, with minimal deviations around the nominal frequency, highlighting the controller's advanced capability to manage frequency stability effectively, as shown in Figure 5.8(b). Impact of gain K on maximum overshoot, settling time, and damping ratio for case study 1 are shown in Table 5.2.

Table 5-2 : Impact of gain K on maximum overshoot, settling time, and damping ratio with case study 1.

Gain K	Maximum Overshoot (%)	Settling Time (Seconds)	Damping Ratio
0	0.225	~0.42	0.43
0.4	0.111	~0.32	0.57
1	0.071	~0.15	0.64

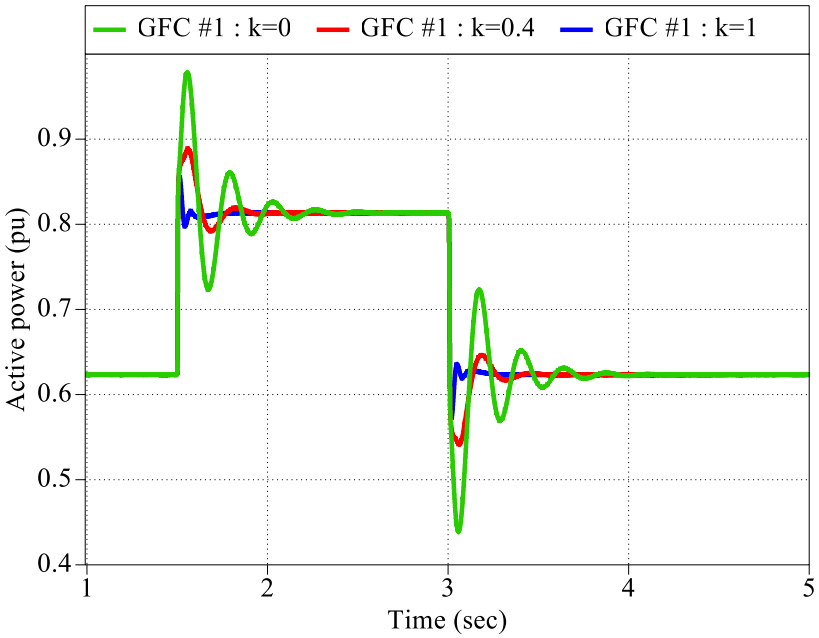

(a)

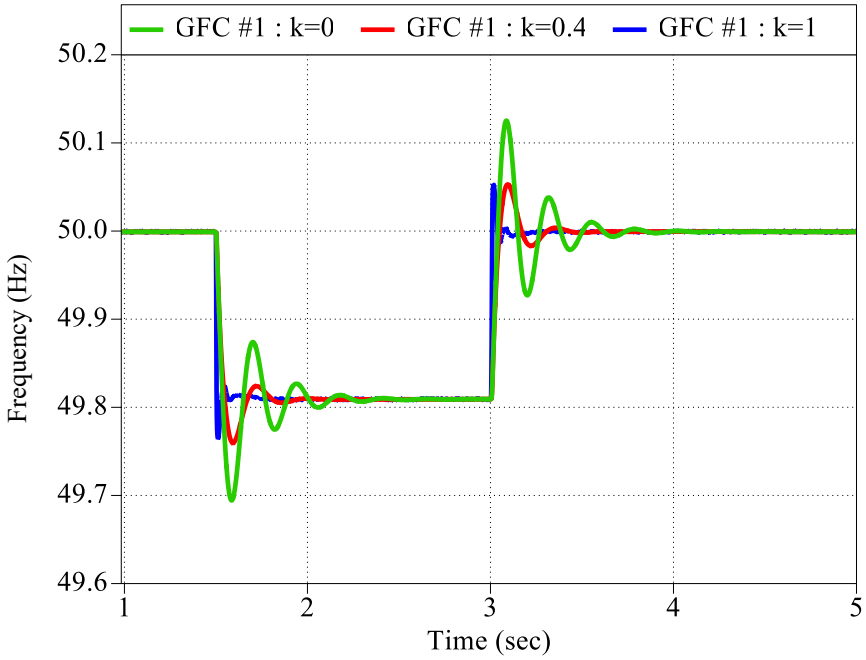

(b)

Figure 5-8: Real-time results for case study 1- system response to a 50 MW step load, (a) active power response, and (b) frequency response of grid forming converter 1.

Case Study 2: Response to Transmission Line Disconnection

The second case study assesses the system performance following the disconnection of a transmission line between bus 1 and bus 3, probing the controller effectiveness in a scenario indicative of grid segmentation or fault isolation. At $K = 0$, immediately after the line disconnection, the system exhibits severe instability with large power swings, as shown in Figure 5.9(a). Moreover, the frequency shows high variability, posing risks to connected equipment and overall grid integrity, as shown in Figure 5.9(b). At $K = 0.4$, the amplitude of power oscillations decreases significantly, indicating that the controller provides a moderate level of stability enhancement, as shown in Figure 5.9(a). Moreover, frequency fluctuations are dampened, yet not entirely eliminated, showing improvement but suggesting a need for full controller integration, as shown in Figure 5.9(b). Finally, at $K = 1$, the power fluctuations are dramatically reduced, almost to a steady state, underscoring the controller's robustness in stabilising the power system under abrupt network changes, as shown in Figure 5.9(a). Moreover, the system exhibits superior frequency stability with minimal fluctuations, demonstrating the controller's full potential in maintaining critical system parameters within safe operational limits, as shown in Figure 5.9(b). Impact of gain K on maximum overshoot, settling time, and damping ratio for case study 2 are shown in Table 5.3.

These results from the PLECS-based real-time analysis demonstrate that the proposed dynamic inertia controller significantly enhances the damping and overall stability of the IEEE 9-bus system. At full integration ($K = 1$), the controller not only manages minor disturbances effectively but also ensures robust system performance under severe transient conditions.

Table 5-3: Impact of gain K on maximum overshoot, settling time, and damping ratio with case study 2.

Gain K	Maximum Overshoot (%)	Settling Time (Seconds)	Damping Ratio
0	0.296	~0.42	0.36
0.4	0.268	~0.37	0.4
1	0.168	~0.33	0.49

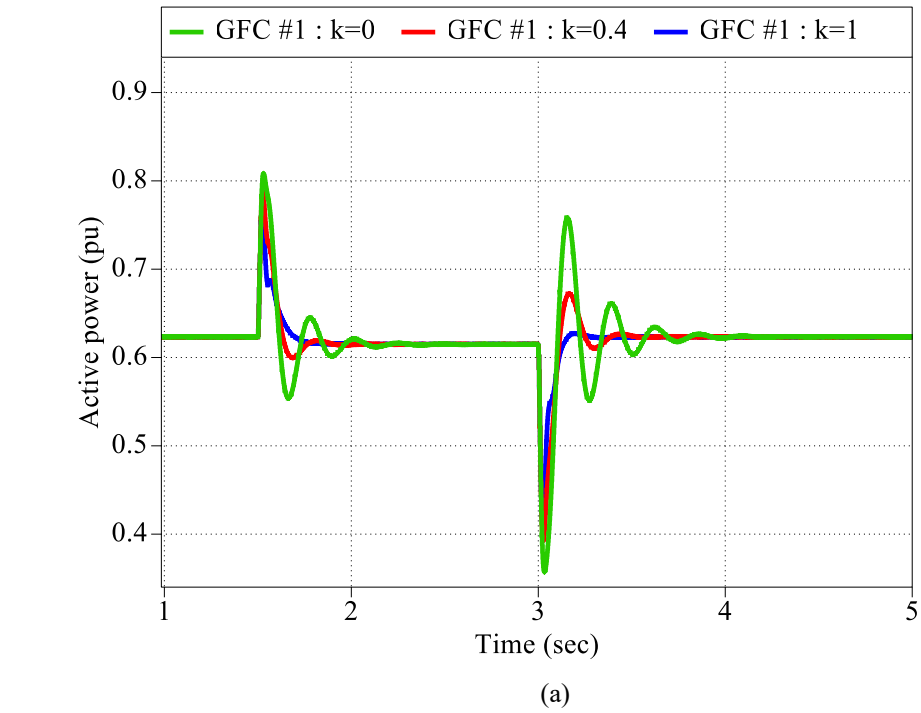

(a)

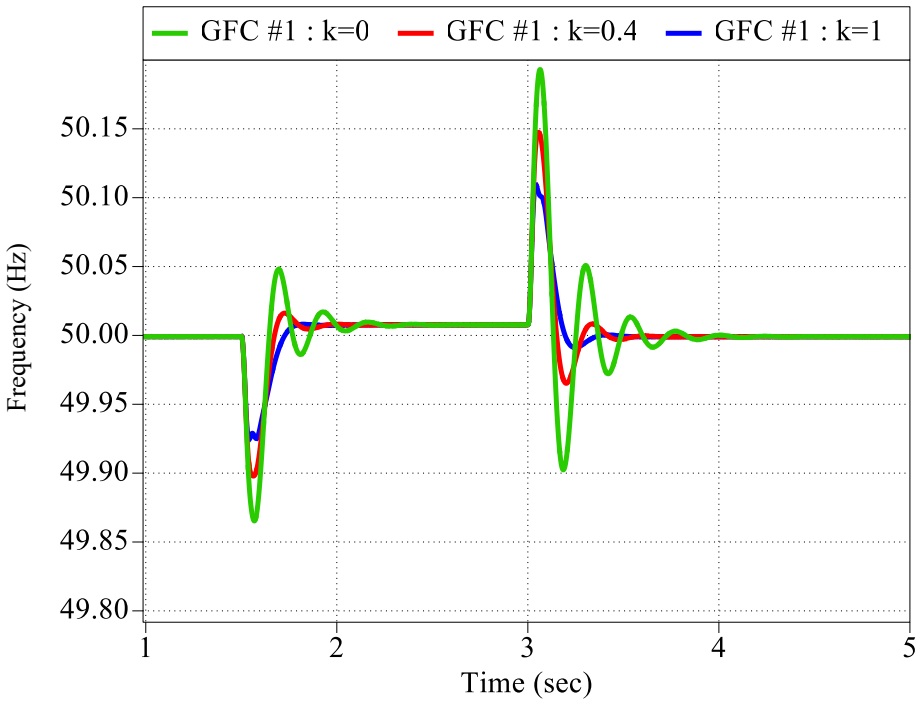

(b)

Figure 5-9: Real-time results for case study 2- system response to a transmission line disconnection, (a) active power response, and (b) frequency response of grid forming converter 1.

Case Study 3: Comparative Analysis with Existing Damping Methods

To validate the superiority of the proposed dynamic inertia damping method, a systematic

comparative analysis is conducted against three widely cited damping enhancement techniques reported in the literature: RoCoF-based damping [90], voltage-based damping [93], and virtual resistance-based damping [96]. The evaluation is performed in MATLAB/Simulink using a consistent test framework to ensure fair benchmarking across all methods. Specifically, the transient performance of each control method is assessed under a standardized step load disturbance scenario. The disturbance involves a 55 MW step increase in system load at $t = 0.5$ s, followed by complete load removal at $t = 1.5$ s.

The active power responses in Fig. 5.10 reveal clear performance differences among the control strategies. The RoCoF-based damping method exhibits pronounced oscillations with significant over- and undershoots, while the virtual resistance and voltage-based damping methods provide improved but still oscillatory responses with higher peak overshoots and slower settling. In contrast, the proposed method achieves superior damping performance by effectively suppressing peak overshoot and rapidly eliminating oscillations, which results in a smooth and well-damped active power response.

Table 5.4 quantifies the performance of all methods using maximum overshoot, settling time, and damping ratio. The proposed method achieves a maximum overshoot of 7%, significantly lower than the RoCoF-based (26%), virtual resistance (16%), and voltage-based (14%) methods, indicating improved transient stability. It also provides the fastest settling time at approximately 0.15 s, compared to 0.19 s, 0.21 s, and 0.22 s for the RoCoF-based, virtual resistance, and voltage-based methods, respectively. Furthermore, the proposed method attains the highest damping ratio of 0.64, surpassing the RoCoF-based (0.39), virtual resistance (0.50), and voltage-based (0.54) approaches, which highlights its enhanced ability to suppress oscillations. Overall, these results confirm that the proposed method outperforms existing state-of-the-art methods in all key performance metrics.

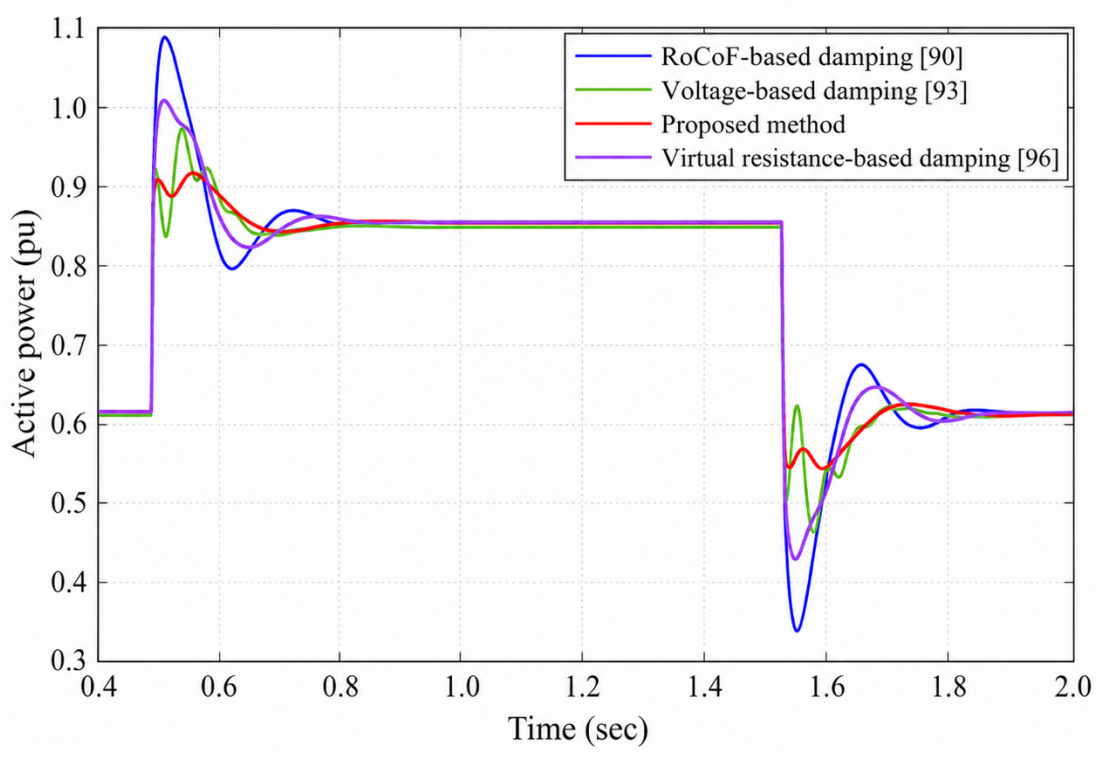

Figure 5-10: Comparative transient response of active power output under 55 MW step load change, which illustrates the damping performance of the proposed method versus RoCoF-based, voltage-based, and virtual resistance-based damping methods.

It is also pertinent to note the distinction in disturbance magnitude between Case Study 1 (50 MW) and Case Study 3 (55 MW). This variation is intentionally introduced to assess the robustness of the proposed controller under differing load conditions. A comparison of the results reveals that the proposed method maintains consistent damping characteristics regardless of the load step magnitude. This consistency is attributed to the relative inertia dynamic damping mechanism inherent in the proposed design. As indicated in Eq(7), the controller provides damping that is proportional to the change in active power and angular velocity. Consequently, the system automatically scales its damping response relative to the severity of the disturbance.

5.4. Summary

A new formula to correlate dynamic inertia, active power, and frequency is derived. Based on this, a novel method was proposed to enhance the damping characteristics of droop controllers by integrating a dynamic inertia model. The model dynamically adjusted inertia in response to frequency and active power fluctuations and significantly improved stability and damping performance, particularly in grid-forming converters. Performance and stability analysis on the

proposed damping controller was conducted using Bode diagrams, phase portraits, equilibrium points, and small-signal stability assessments. The results demonstrate the controller stability and effectiveness in improving the damping characteristics of the GFC. Moreover, real-time simulations using the PLECS platform were performed to comprehensively evaluate the controller performance under different operating conditions. Validation was conducted on the IEEE 9-bus system through two case studies: a 50 MW step load and a transmission line disconnection. The results show that the damping ratio improved by approximately 40% to 50%, depending on the severity of the disturbance. Moreover, a comparative study against three state-of-the-art damping strategies, namely, RoCoF-based, voltage-based, and virtual resistance-based damping, highlighted the superior performance of the proposed method. Specifically, it achieved the lowest maximum overshoot (7%), the fastest settling time (~0.15 s), and the highest damping ratio (0.64), outperforming RoCoF-based damping (26%, ~0.19 s, 0.39), voltage-based damping (14%, ~0.22 s, 0.54), and virtual resistance-based damping (16%, ~0.21 s, 0.50). These results collectively underscore the proposed controller's robustness and practical suitability for next-generation converter-dominated power systems.

Chapter 6 Conclusions and Future Work

This chapter provides a summary of the presented thesis and suggests several future research directions that are expected to contribute significantly to the field.

6.1. Conclusions

This thesis has developed and validated a novel hierarchical energy management system (EMS) that significantly enhances black-start capabilities and normal operations across distribution and transmission networks. Key outcomes from validation on the IEEE 39-bus test network demonstrate the superior performance of the proposed system. Compared to conventional, non-hierarchical restoration strategies, the proposed EMS reduced non-critical load shedding by 25% and increased the utilisation of available renewable energy by 40% during the critical black start phase. The hierarchical control structure, which coordinates distribution and transmission controllers, effectively manages complex interactions, resulting in a 30% reduction in the total system restoration time. This comprehensive framework represents a significant advancement in energy management, addressing key challenges of grid reliability and facilitating the large-scale integration of renewable generation.

Furthermore, the thesis successfully addressed low-inertia problems through a novel method to enhance the damping characteristics of droop controllers by integrating a dynamic inertia model. Validation was conducted on the IEEE 9-bus system using the PLECS platform. In response to a 50 MW step load disturbance, the proposed method improved the frequency nadir from 49.5 Hz (with conventional droop control) to 49.7 Hz and reduced the frequency settling time by 50%. For the transmission line disconnection scenario, the dynamic inertia model increased the damping ratio of the critical electromechanical mode from 0.05 to 0.15, effectively preventing oscillations. These results confirm that the adaptive control framework provides a more responsive and stable response, significantly enhancing the damping performance of power systems with high renewable energy penetration.

6.2. Author's Contributions

The scientific contributions presented in this thesis include the design of a hierarchical Energy Management System with black start capability and load prioritisation across transmission and distribution networks, together with a unique optimisation formulation integrated within the

hierarchical EMS framework to enhance system inertia during black start operation, optimise load shedding, and improve renewable energy integration through prioritisation of solar power, battery storage, and fuel cell technologies. The developed EMS also establishes a coordinated framework for multi-area power networks involving black start-capable areas (BSAs) and non-black start-capable areas (NBSAs), where BSAs restore essential local loads first before extending support to neighbouring NBSAs based on reserve power availability and geographical proximity. This EMS framework is validated using both the IEEE 39-bus network with ten interconnected areas and the IEEE 10-bus network, each with different black start capabilities, while also identifying limitations in existing EMS approaches such as insufficient transmission–distribution coordination, limited black start integration, and inadequate renewable energy prioritisation.

In addition, an advanced dynamic inertia damping enhancement is developed for droop control in grid-forming converters, which improves existing techniques by optimising the interaction between inertia, active power, and frequency. This method enables real-time adjustment of inertia to improve damping performance under transient conditions and is integrated within the traditional droop control framework. A regularised control law is introduced to ensure numerical stability, together with deadband operation and low-pass filtering to enhance robustness under practical operating conditions. The dynamic behaviour of the proposed method is analysed using equilibrium point analysis, small-signal stability assessment, Bode diagrams, and phase portrait analysis.

The proposed damping method is validated using the IEEE 9-bus system in the PLECS environment under different disturbance scenarios including 50-MW step load changes and transmission line disconnection events, and is compared against existing damping methods such as RoCoF-based, voltage-based, and virtual resistance-based approaches. The results demonstrate improved damping ratio, reduced settling time, and enhanced transient stability. All simulation models and validation studies are implemented in MATLAB/Simulink and PLECS environments.

6.3. Future Work

Based on the presented EMS (chapter 3) and damping method (chapter 5), several future works suggestions are outlined below.

- **Cable Thickness Considerations:**

The presented EMS overlooks the impact of cable thickness. Investigating the effects of cable thickness and line impedance in the hierarchical EMS is important to enhance the accuracy of power flow calculations and optimisation.

- **Inclusion of Additional Energy Sources:**

The presented EMS works with hybrid sources; solar cells and fuel cell. This EMS can be extended by integrating other renewable energy sources (e.g., wind turbines, geothermal energy) and exploring the potential of hybrid systems that combine fuel cells with other storage technologies, such as supercapacitors or flywheels.

- **Scalability and Adaptability:**

The presented EMS is tested on IEEE-39-bus and the proposed method can be tested on different bus systems (e.g., IEEE 57-bus, IEEE 118-bus) to evaluate scalability and adaptability. It can also adapt the hierarchical EMS for real-time applications in large-scale smart grids and microgrids.

- **Advanced Optimisation Techniques:**

Advanced optimisation algorithms, such as genetic algorithms, particle swarm optimization, or machine learning techniques can be discovered to further enhance the performance of the hierarchical EMS.

- **Real-World Implementation:**

The proposed EMS and damping method can be use in real-world pilot projects in collaboration with industry partners. It can conduct long-term field studies to evaluate the reliability, efficiency, and economic benefits of the proposed solutions.

- **User-Centric Energy Management:**

A user interface and decision-support tool can be developed to allow consumers to interact with the hierarchical EMS, enhancing user satisfaction and engagement. It can be incorporated into demand response programs to optimise energy consumption patterns based on real-time pricing and user preferences.

- **Policy and Regulatory Considerations:**

The impact of regulatory frameworks on the implementation of hierarchical EMS and advanced damping methods can be studied. Some recommendations for policy makers to support the adoption of these technologies in the transition to renewable energy systems can be provided.

- **Enhanced Damping Methods:**

Other advanced damping techniques, such as adaptive control strategies or artificial intelligence-based methods can be investigated to further improve the stability of grid-forming converters. The interaction between dynamic inertia damping and other control mechanisms, such as voltage control or reactive power compensation can be explored.

References

[1] M. B. Prasad, P. Ganesh, K. Vinay Kumar, P. Mohanarao, A. Swathi, and V. Manoj, "Renewable energy integration in modern power systems: Challenges and opportunities," in *E3S Web of Conferences*, 2024, vol. 591: EDP Sciences, p. 03002.

[2] O. S. Abualoyoun and A. A. Amar, "Toward Achieving Net-Zero in the Evolution of the Global Energy Sector," *Int. J. Electr. Eng. and Sustain.,* pp. 143-156, 2025.

[3] S. Shahzad and E. Jasińska, "Renewable revolution: A review of strategic flexibility in future power systems," *Sustainability,* vol. 16, no. 13, p. 5454, 2024.

[4] L. Meegahapola, A. Sguarezi, J. S. Bryant, M. Gu, E. R. Conde D, and R. B. Cunha, "Power system stability with power-electronic converter interfaced renewable power generation: Present issues and future trends," *Energies,* vol. 13, no. 13, p. 3441, 2020.

[5] R. Bessa, C. Moreira, B. Silva, and M. Matos, "Handling renewable energy variability and uncertainty in power system operation," *Advances in Energy Systems: The Large-scale Renewable Energy Integration Challenge,* pp. 1-26, 2019.

[6] G. M. Njoka, L. Mogaka, and A. Wangai, "Impact of variable renewable energy sources on the power system frequency stability and system inertia," *Energy Reports,* vol. 12, pp. 4983-4997, 2024.

[7] Y. Zahraoui, I. Alhamrouni, S. Mekhilef, M. R. Basir Khan, M. Seyedmahmoudian, A. Stojcevski, and B. Horan, "Energy management system in microgrids: A comprehensive review," *Sustainability,* vol. 13, no. 19, p. 10492, 2021.

[8] D. Espín-Sarzosa, R. Palma-Behnke, and O. Núñez-Mata, "Energy management systems for microgrids: Main existing trends in centralized control architectures," *Energies,* vol. 13, no. 3, p. 547, 2020.

[9] M. Cavus, "Integration Smart Grids, Distributed Generation, and Cybersecurity: Strategies for Securing and Optimizing Future Energy Systems," 2024.

[10] P. Toledano, A. Shah, N. Maennling, and R. Lasnick, "Electric Utility Alignment with the SDGs & The Paris Climate Agreement," *Available at SSRN 3669843,* 2020.

[11] M. Green. "UK will miss net zero by 2050, decarbonisation by 2030, says DNV report." https://www.solarpowerportal.co.uk/utility-scale-solar/uk-will-miss-net-zero-by-2050-decarbonisation-by-2030-says-dnv-report (accessed May 2026).

[12] G. M. Giannuzzi, V. Mostova, C. Pisani, S. Tessitore, and A. Vaccaro, "Enabling technologies for enhancing power system stability in the presence of converter-interfaced generators," *Energies,* vol. 15, no. 21, p. 8064, 2022.

[13] A. S. Al-Farsi, *Impact of Renewable Energy on Power System Inertia and Rate of Change of Frequency (ROCOF) for the MIS System*. Sultan Qaboos University (Oman), 2024.

[14] N. Shaukat, M. R. Islam, M. M. Rahman, B. Khan, B. Ullah, S. M. Ali, and A. Fekih, "Decentralized, democratized, and decarbonized future electric power distribution grids: a survey on the paradigm shift from the conventional power system to micro grid structures," *IEEE Access,* vol. 11, pp. 60957-60987, 2023.

[15] Y. Wu, Y. Wu, J. M. Guerrero, and J. C. Vasquez, "Decentralized transactive energy community in edge grid with positive buildings and interactive electric vehicles," *International Journal of Electrical Power & Energy Systems,* vol. 135, p. 107510, 2022.

[16] M. Khorasany, "Market design for peer-to-peer energy trading in a distribution network with high penetration of distributed energy resources," Queensland University of Technology, 2020.

[17] K. E. Antoniadou-Plytaria, I. N. Kouveliotis-Lysikatos, P. S. Georgilakis, and N. D. Hatziargyriou, "Distributed and decentralized voltage control of smart distribution networks: Models, methods, and future research," *IEEE Transactions on smart grid,* vol. 8, no. 6, pp. 2999-3008, 2017.

[18] H. H. Mousa, K. Mahmoud, and M. Lehtonen, "Recent developments of demand-side management towards flexible DER-rich power systems: A systematic review," *IET Generation, Transmission & Distribution,* vol. 18, no. 13, pp. 2259-2300, 2024.

[19] A. Khurram, M. Amini, L. A. D. Espinosa, P. D. Hines, and M. R. Almassalkhi, "Real-time grid and der co-simulation platform for testing large-scale der coordination schemes," *IEEE Transactions on Smart Grid,* vol. 13, no. 6, pp. 4367-4378, 2022.

[20] E. J. Smith, D. A. Robinson, and S. Elphick, "DER control and management strategies for distribution networks: A review of current practices and future directions," *Energies,* vol. 17, no. 11, p. 2636, 2024.

[21] R. Leal-Arcas, F. Lesniewska, and F. Proedrou, "Prosumers as new energy actors," in *Africa-EU Renewable Energy Research and Innovation Symposium*, 2018: Springer International Publishing Cham, pp. 139-151.

[22] A. Kabir, "Dynamic-adaptive centralized frequency arresting methodology to prevent power system blackout," 2018.

[23] P. Tielens and D. Van Hertem, "The relevance of inertia in power systems," *Renewable and sustainable energy reviews,* vol. 55, pp. 999-1009, 2016.

[24] D. Al Kez, "Power system dynamics with increasing distributed generation penetrations," Queen's University Belfast, 2022.

[25] M. Nedd, "Changes to system inertia and the impact on frequency response requirements," 2020.

[26] S. Homan, "Future frequency response requirements in low inertia grids," University of Sheffield, 2021.

[27] T. Kerdphol, F. S. Rahman, M. Watanabe, Y. Mitani, D. Turschner, and H.-P. Beck, "Enhanced virtual inertia control based on derivative technique to emulate simultaneous inertia and damping properties for microgrid frequency regulation," *IEEE access,* vol. 7, pp. 14422-14433, 2019.

[28] R. Rosso, X. Wang, M. Liserre, X. Lu, and S. Engelken, "Grid-forming converters: Control approaches, grid-synchronization, and future trends—A review," *IEEE Open Journal of Industry Applications,* vol. 2, pp. 93-109, 2021.

[29] H. Kikusato *et al.*, "Performance analysis of grid-forming inverters in existing conformance testing," *Energy Reports,* vol. 8, pp. 73-83, 2022.

[30] L. Hernandez, C. Baladron, J. M. Aguiar, B. Carro, A. J. Sanchez-Esguevillas, J. Lloret, and J. Massana, "A survey on electric power demand forecasting: future trends in smart grids, microgrids and smart buildings," *IEEE Communications Surveys & Tutorials,* vol. 16, no. 3, pp. 1460-1495, 2014.

[31] A. Kudzin, S. Takayama, and A. Ishigame, "Energy Management Systems (EMS) for a Decentralized Grid: A Review and Analysis of the Generation and Control Methods Impact on EMS Type and Topology," *IET Renewable Power Generation,* vol. 19, no. 1, p. e70008, 2025.

[32] A. Basnawi, "Addressing challenges in EMS department operations: a comprehensive analysis of key issues and solution," *Emergency Care and Medicine,* vol. 1, no. 1, pp. 11-23, 2023.

[33] D. Mock, J. Bush, and S. V. Arbogast, "DERs Role in a More Reliable, Sustainable, and Resilient Power System," ed: UNC Energy Center, Kenan-Flagler Business School Chapel Hill, NC, USA, 2024.

[34] J. Liu, X. Zhuan, L. Shang, S. Su, and Q. Xie, "The hierarchical structure and control signal transmission of microgrid hierarchical control: A review," *IET Power Electronics,* vol. 18, no. 1, p. e70057, 2025.

[35] M. Moghimi, "Modelling and Optimization of Energy Management Systems in Microgrids and Multi-Microgrids," 2018.

[36] R. P. Masini, M. C. Medeiros, and E. F. Mendes, "Machine learning advances for time series forecasting," *Journal of economic surveys,* vol. 37, no. 1, pp. 76-111, 2023.

[37] S. Ahmad, M. Shafiullah, C. B. Ahmed, and M. Alowaifeer, "A review of microgrid energy management and control strategies," *IEEe Access,* vol. 11, pp. 21729-21757, 2023.

[38] S. Behera and N. B. Dev Choudhury, "A systematic review of energy management system based on various adaptive controllers with optimization algorithm on a smart microgrid," *International Transactions on electrical energy Systems,* vol. 31, no. 12, p. e13132, 2021.

[39] P. K. Kurella and S. Mikkili, "A comprehensive review of DERMS for smart and secure energy networks: standards, protocols, and security considerations," *International Journal of Ambient Energy,* vol. 46, no. 1, p. 2506703, 2025.

[40] T. Morstyn, N. Farrell, S. J. Darby, and M. D. McCulloch, "Using peer-to-peer energy-trading platforms to incentivize prosumers to form federated power plants," *Nature energy,* vol. 3, no. 2, pp. 94-101, 2018.

[41] Z. Yi, Y. Xu, W. Gu, and W. Wu, "A multi-time-scale economic scheduling strategy for virtual power plant based on deferrable loads aggregation and disaggregation," *IEEE Transactions on Sustainable Energy,* vol. 11, no. 3, pp. 1332-1346, 2019.

[42] H.-J. Cha, J.-Y. Choi, and D.-J. Won, "Smart load management in demand response using microgrid EMS," in *2014 IEEE International Energy Conference (ENERGYCON)*, 2014: IEEE, pp. 833-837.

[43] C. Özkan and S. Şahin, "AI Applications in Real-Time Edge Processing: Leveraging Artificial Intelligence for Enhanced Efficiency, Low-Latency Decision Making, and Scalability in Distributed Systems."

[44] S. Xu, Y. Xue, and L. Chang, "Review of power system support functions for inverter-based distributed energy resources-standards, control algorithms, and trends," *IEEE open journal of Power electronics,* vol. 2, pp. 88-105, 2021.

[45] N. Q. Tunio, "Enhancing the Security of Critical Infrastructure in Emergency Services."

[46] M. Kezunovic and A. Bose, "The future EMS design requirements," in *2013 46th Hawaii International Conference on System Sciences*, 2013: IEEE, pp. 2354-2363.

[47] R. J. Kumar and P. Vijayakumar, "A Survey of Hierarchical Control Aspects of hybrid Microgrid," in *2024 International Conference on Smart Systems for Electrical, Electronics, Communication and Computer Engineering (ICSSEECC)*, 2024: IEEE, pp. 466-471.

[48] A. Kumar, A. Maulik, and K. Chinmaya, "Energy Management Strategies for Active Distribution Networks and Microgrids–A Comprehensive Survey," *IETE Technical Review,* pp. 1-40, 2025.

[49] F. Khan, M. Al Rawajbeh, L. K. Ramasamy, and S. Lim, "Context-aware and click session-based graph pattern mining with recommendations for smart EMS through AI," *IEEE Access,* vol. 11, pp. 59854-59865, 2023.

[50] S. Umetani, Y. Fukushima, and H. Morita, "A linear programming based heuristic algorithm for charge and discharge scheduling of electric vehicles in a building energy management system," *Omega,* vol. 67, pp. 115-122, 2017.

[51] B. N. Alhasnawi and B. H. Jasim, "A Novel Hierarchical Energy Management System Based on Optimization for Multi-Microgrid," *International Journal on Electrical Engineering & Informatics,* vol. 12, no. 3, 2020.

[52] N. Tomin, V. Shakirov, A. Kozlov, D. Sidorov, V. Kurbatsky, C. Rehtanz, and E. E. Lora, "Design and optimal energy management of community microgrids with flexible renewable energy sources," *Renewable Energy,* vol. 183, pp. 903-921, 2022.

[53] P. Lissa, C. Deane, M. Schukat, F. Seri, M. Keane, and E. Barrett, "Deep reinforcement learning for home energy management system control," *Energy and AI,* vol. 3, p. 100043, 2021.

[54] H. Musbah, G. Ali, H. H. Aly, and T. A. Little, "Energy management using multi-criteria decision making and machine learning classification algorithms for intelligent system," *Electric Power Systems Research,* vol. 203, p. 107645, 2022.

[55] H. Musbah, H. H. Aly, and T. A. Little, "Energy management of hybrid energy system sources based on machine learning classification algorithms," *Electric Power Systems Research,* vol. 199, p. 107436, 2021.

[56] A. Cagnano, A. C. Bugliari, and E. De Tuglie, "A cooperative control for the reserve management of isolated microgrids," *Applied energy,* vol. 218, pp. 256-265, 2018.

[57] J. Li, H. You, J. Qi, M. Kong, S. Zhang, and H. Zhang, "Stratified optimization strategy used for restoration with photovoltaic-battery energy storage systems as black-start resources," *IEEE Access,* vol. 7, pp. 127339-127352, 2019.

[58] Z. Xu, P. Yang, Z. Zeng, J. Peng, and Z. Zhao, "Black start strategy for PV-ESS multi-microgrids with three-phase/single-phase architecture," *Energies,* vol. 9, no. 5, p. 372, 2016.

[59] Q. Fu, A. Nasiri, V. Bhavaraju, A. Solanki, T. Abdallah, and C. Y. David, "Transition management of microgrids with high penetration of renewable energy," *IEEE Transactions on Smart Grid,* vol. 5, no. 2, pp. 539-549, 2013.

[60] Z. Fu, Z. Li, P. Si, and F. Tao, "A hierarchical energy management strategy for fuel cell/battery/supercapacitor hybrid electric vehicles," *International journal of hydrogen energy,* vol. 44, no. 39, pp. 22146-22159, 2019.

[61] M. A. Mosa and A. Ali, "Energy management system of low voltage dc microgrid using mixed-integer nonlinear programing and a global optimization technique," *Electric Power Systems Research,* vol. 192, p. 106971, 2021.

[62] W. Hu, P. Wang, and H. B. Gooi, "Toward optimal energy management of microgrids via robust two-stage optimization," *IEEE Transactions on smart grid,* vol. 9, no. 2, pp. 1161-1174, 2016.

[63] M. Di Piazza, G. La Tona, M. Luna, and A. Di Piazza, "A two-stage Energy Management System for smart buildings reducing the impact of demand uncertainty," *Energy and Buildings,* vol. 139, pp. 1-9, 2017.

[64] M. Mohiti, H. Monsef, A. Anvari-Moghaddam, and H. Lesani, "Two-stage robust optimization for resilient operation of microgrids considering hierarchical frequency control structure," *IEEE Transactions on Industrial Electronics,* vol. 67, no. 11, pp. 9439-9449, 2019.

[65] N. Bazmohammadi, A. Tahsiri, A. Anvari-Moghaddam, and J. M. Guerrero, "Stochastic predictive control of multi-microgrid systems," *IEEE Transactions on Industry Applications,* vol. 55, no. 5, pp. 5311-5319, 2019.

[66] V. Dao, H. Ishii, Y. Takenobu, S. Yoshizawa, and Y. Hayashi, "Intensive quadratic programming approach for home energy management systems with power utility requirements," *International Journal of Electrical Power & Energy Systems,* vol. 115, p. 105473, 2020.

[67] N. Bazmohammadi, A. Tahsiri, A. Anvari-Moghaddam, and J. M. Guerrero, "A hierarchical energy management strategy for interconnected microgrids considering uncertainty," *International Journal of Electrical Power & Energy Systems,* vol. 109, pp. 597-608, 2019.

[68] V. S. Tabar, M. A. Jirdehi, and R. Hemmati, "Energy management in microgrid based on the multi objective stochastic programming incorporating portable renewable energy resource as demand response option," *Energy,* vol. 118, pp. 827-839, 2017.

[69] F. Varasteh, M. S. Nazar, A. Heidari, M. Shafie-khah, and J. P. Catalão, "Distributed energy resource and network expansion planning of a CCHP based active microgrid considering demand response programs," *Energy,* vol. 172, pp. 79-105, 2019.

[70] M. Movahednia, H. Karimi, and S. Jadid, "Optimal hierarchical energy management scheme for networked microgrids considering uncertainties, demand response, and adjustable power," *IET Generation, Transmission & Distribution,* vol. 14, no. 20, pp. 4352-4362, 2020.

[71] N. Nikolaev, K. Dimitrov, and Y. Rangelov, "A comprehensive review of small-signal stability and power oscillation damping through photovoltaic inverters," *Energies,* vol. 14, no. 21, p. 7372, 2021.

[72] K. Rahman, J. Hashimoto, D. Orihara, T. S. Ustun, K. Otani, H. Kikusato, and Y. Kodama, "Reviewing control paradigms and emerging trends of grid-forming inverters—A comparative study," *Energies,* vol. 17, no. 10, p. 2400, 2024.

[73] N. Julius, J. N. Nderu, and G. Irungu, "Frequency control and virtual inertia emulation techniques for grid connected wind energy conversion systems-a review," *2019 IEEE AFRICON,* pp. 1-6, 2019.

[74] L. Xiu, L. Xiong, P. Yang, and Z. Kang, "Inertial and damping characteristics of DC distributed power systems based on frequency droop control," *Energies,* vol. 11, no. 9, p. 2418, 2018.

[75] A. Fernández-Guillamón, E. Gómez-Lázaro, E. Muljadi, and Á. Molina-Garcia, "A review of virtual inertia techniques for renewable energy-based generators," *Renewable Energy-Technologies and Applications,* 2020.

[76] J. L. Domínguez-García, O. Gomis-Bellmunt, F. D. Bianchi, and A. Sumper, "Power oscillation damping supported by wind power: A review," *Renewable and Sustainable Energy Reviews,* vol. 16, no. 7, pp. 4994-5006, 2012.

[77] N. Ram Babu, S. K. Bhagat, L. C. Saikia, T. Chiranjeevi, R. Devarapalli, and F. P. García Márquez, "A comprehensive review of recent strategies on automatic generation control/load frequency control in power systems," *Archives of Computational Methods in Engineering,* vol. 30, no. 1, pp. 543-572, 2023.

[78] X. Zhang, C. Lu, S. Liu, and X. Wang, "A review on wide-area damping control to restrain inter-area low frequency oscillation for large-scale power systems with increasing renewable generation," *Renewable and Sustainable Energy Reviews,* vol. 57, pp. 45-58, 2016.

[79] U. Tamrakar, D. Shrestha, M. Maharjan, B. P. Bhattarai, T. M. Hansen, and R. Tonkoski, "Virtual inertia: Current trends and future directions," *Applied sciences,* vol. 7, no. 7, p. 654, 2017.

[80] M. Shadoul, R. Ahshan, R. S. AlAbri, A. Al-Badi, M. Albadi, and M. Jamil, "A comprehensive review on a virtual-synchronous generator: Topologies, control orders and techniques, energy storages, and applications," *Energies,* vol. 15, no. 22, p. 8406, 2022.

[81] M. A. Shobug, N. A. Chowdhury, M. A. Hossain, M. J. Sanjari, J. Lu, and F. Yang, "Virtual inertia control for power electronics-integrated power systems: Challenges and prospects," *Energies,* vol. 17, no. 11, p. 2737, 2024.

[82] N. K. Roy, S. Islam, A. K. Podder, T. K. Roy, and S. Muyeen, "Virtual inertia support in power systems for high penetration of renewables—overview of categorization, comparison, and evaluation of control techniques," *IEEE Access,* vol. 10, pp. 129190-129216, 2022.

[83] S. Hasheminasab, M. Alzayed, and H. Chaoui, "A review of control techniques for inverter-based distributed energy resources applications," *Energies,* vol. 17, no. 12, p. 2940, 2024.

[84] M. Khalid and B. Panigrahi, "Decentralized power management in multi bess-pv based charging infrastructure for ev with soc balancing," *IEEE Transactions on Industry Applications,* vol. 59, no. 6, pp. 7392-7403, 2023.

[85] L. Subramanian, "Stability Enhancement of Inverter-dominated power systems with virtual inertia control," Université Grenoble Alpes [2020-....]; Nanyang Technological University …, 2021.

[86] C. Jiang, A. D. Sinkar, and A. M. Gole, "Small signal analysis of a grid-forming modular multilevel converter with a novel virtual synchronous generator control," *Electric Power Systems Research,* vol. 223, p. 109621, 2023.

[87] P. Unruh, M. Nuschke, P. Strauß, and F. Welck, "Overview on grid-forming inverter control methods," *Energies,* vol. 13, no. 10, p. 2589, 2020.

[88] J. Liu, Y. Miura, and T. Ise, "Comparison of dynamic characteristics between virtual synchronous generator and droop control in inverter-based distributed generators," *IEEE Transactions on Power Electronics,* vol. 31, no. 5, pp. 3600-3611, 2015.

[89] Q.-C. Zhong, P.-L. Nguyen, Z. Ma, and W. Sheng, "Self-synchronized synchronverters: Inverters without a dedicated synchronization unit," *IEEE Transactions on power electronics,* vol. 29, no. 2, pp. 617-630, 2013.

[90] X. Xiong, C. Wu, B. Hu, D. Pan, and F. Blaabjerg, "Transient damping method for improving the synchronization stability of virtual synchronous generators," *IEEE Transactions on Power Electronics,* vol. 36, no. 7, pp. 7820-7831, 2020.

[91] C. Li, Y. Cao, Y. Yang, J. Xu, M. Wu, W. Zhang, and T. Dragičević, "New framework of RoCoF-FD for wideband stability evaluation in renewable energy generators with virtual impedance control," *IEEE Transactions on Smart Grid,* vol. 13, no. 5, pp. 3570-3581, 2022.

[92] R. Xie, I. Kamwa, and C. Chung, "A novel wide-area control strategy for damping of critical frequency oscillations via modulation of active power injections," *IEEE Transactions on Power Systems,* vol. 36, no. 1, pp. 485-494, 2020.

[93] M. Ebrahimi, S. A. Khajehoddin, and M. Karimi-Ghartemani, "An improved damping method for virtual synchronous machines," *IEEE Transactions on Sustainable Energy,* vol. 10, no. 3, pp. 1491-1500, 2019.

[94] M. Ahmed, F. Alsokhiry, A. S. Abdel-Khalik, K. H. Ahmed, and Y. Al-Turki, "Improved damping control method for grid-forming converters using lqr and optimally weighted feedback control loops," *IEEE Access,* vol. 9, pp. 87484-87500, 2021.

[95] P. M. de Almeida *et al.*, "Systematic design of a DLQR applied to grid-forming converters," *IEEE Journal of Emerging and Selected Topics in Industrial Electronics,* vol. 1, no. 2, pp. 200-210, 2020.

[96] S. P. Me, S. Zabihi, F. Blaabjerg, and B. Bahrani, "Adaptive virtual resistance for postfault oscillation damping in grid-forming inverters," *IEEE Transactions on Power Electronics,* vol. 37, no. 4, pp. 3813-3824, 2021.

[97] Y. Zhu, S. Jiang, J. Pou, and G. Konstantinou, "Virtual Arm Impedance Emulation and Stability Improvement in Modular Multilevel Converters," *IEEE Transactions on Power Electronics,* 2024.

[98] G. N. Baltas, N. B. Lai, A. Tarraso, L. Marin, F. Blaabjerg, and P. Rodriguez, "AI-based damping of electromechanical oscillations by using grid-connected converter," *Frontiers in Energy Research,* vol. 9, p. 598436, 2021.

[99] H. Shuai, B. She, J. Wang, and F. Li, "Safe Reinforcement Learning for Grid-Forming Inverter Based Frequency Regulation with Stability Guarantee," *Journal of Modern Power Systems and Clean Energy,* 2024.

[100] G. N. Baltas, N. B. Lai, L. Marin, A. Tarrasó, and P. Rodriguez, "Grid-forming power converters tuned through artificial intelligence to damp subsynchronous interactions in electrical grids," *IEEE access,* vol. 8, pp. 93369-93379, 2020.

[101] J. Li, X. Wang, Q. Zhang, and P. Tang, "Multi-objective optimization of EMS facilities using multi-source data: A case study in Dangtu, China," *Frontiers of Architectural Research,* vol. 14, no. 4, pp. 1090-1107, 2025.

[102] M. M. Zadeh, P. M. Rezayi, S. Ghafouri, M. Alizadeh, and G. Gharehpetian, "IoT-based stochastic EMS using multi-agent system for coordination of grid-connected multi-microgrids," *International Journal of Electrical Power & Energy Systems,* vol. 151, p. 109191, 2023.

[103] A. J. O. Rasool Heydari, Jean-Philippe Hasler. "Stability Enhancement of Weak Grids with High Penetration of Renewables." https://www.hitachihyoron.com/rev/contents/202505/tech_docs/04/index.html (accessed 10 May 2026.

[104] W. Sun, C.-C. Liu, and L. Zhang, "Optimal generator start-up strategy for bulk power system restoration," *IEEE Transactions on Power Systems,* vol. 26, no. 3, pp. 1357-1366, 2010.

[105] A. M. El-Zonkoly, "Renewable energy sources for complete optimal power system black-start restoration," *IET generation, transmission & distribution,* vol. 9, no. 6, pp. 531-539, 2015.

[106] J. Su, C. Chen, and Z. Bie, "Optimal Generator Start-Up Sequence Strategy Considering Renewable Energy Participation," in *Annual Conference of China Electrotechnical Society*, 2022: Springer, pp. 934-945.

[107] A. Alassi and O. Ellabban, "Design of an intelligent energy management system for standalone PV/battery DC microgrids," in *2019 2nd International Conference on Smart Grid and Renewable Energy (SGRE)*, 2019: IEEE, pp. 1-7.

[108] N. P. Project. "NASA POWER Data Access Viewer." https://power.larc.nasa.gov/data-access-viewer/ (accessed 2025.

[109] NationalGrid, "CONNECTION CONDITIONS (CC) CONTENTS," 2024. Accessed: 2025. [Online]. Available: https://www.nationalgrid.com/sites/default/files/documents/8589935284-Connection%20Conditions.pdf

[110] I. Taczi, I. Vokony, B. Hartmann, and K. P. Juhasz, "Time domain assessment of power system stability in case of high share of non-synchronous generation–limitation analysis of electromechanical transient simulations," *RE&PQJ,* vol. 23, no. 3, pp. 84-89, 2025.

Appendix A: The EMS Algorithm

```
function [battpower,battpower2,dynp,cnt] =
fcn(cuschoice,sunny,solarpower,soc,maxxharge,gridsupport,loadshed,literp)
  if (solarpower>0) %d
    if(loadshed==0) %d
      if (solarpower>=500*3) %d
        if ((solarpower-500e3*3)>maxxharge || soc>=100) %d
          if (gridsupport==1) %d
            battpower=maxxharge;
            battpower2=0;
            dynp=500*3;
            cnt=0;
          else
            battpower=maxxharge;
            battpower2=0;
            dynp=500*3;
            cnt=1;
          end
        else
        battpower=solarpower-500*3;
        battpower2=0;
        dynp=500*3;
        cnt=0;
        end
      else
        if (soc>0.1) %d
        battpower=solarpower-500*3;
        battpower2=0;
        dynp=500*3;
        cnt=0;
        else
        battpower=0;
        battpower2=0;
        dynp=solarpower;
        cnt=0;
        end
      end
    else
      if (solarpower<=500 && soc>=0.1) %d
        dynp=500;
        battpower=solarpower-500;
        battpower2=0;
        cnt=0;
      elseif (solarpower<500 && soc<=0.1)
        dynp=solarpower;
        battpower2=0;
        battpower=0;
```

```
            cnt=0;
        elseif (solarpower>=500 && soc<70)
            battpower=min(solarpower-500,maxxharge);
            battpower2=0;
            dynp=solarpower-battpower;
            cnt=0;
        elseif (solarpower>500 && soc>=70)
            if (soc<100) %d
            dynp=min(500*3,solarpower);
            battpower2=0;
            battpower=solarpower-dynp;
            cnt=0;
            else
               if (gridsupport==1) %d
            dynp=min(500*3,solarpower);
            battpower2=0;
            battpower=0;
            cnt=0;
               else
            dynp=min(500*3,solarpower);
            battpower2=0;
            battpower=0;
            cnt=1;
               end
            end
        else
            dynp=solarpower;
            battpower=0;
            battpower2=0;
            cnt=0;
        end
    end
elseif (solarpower<=0)
            if (soc>=70) %d
              dynp=500*3;
              battpower=-dynp;
              battpower2=0;
              cnt=0;
            elseif (soc >= 50)
              dynp=500*2;
              battpower=-dynp;
              battpower2=0;
              cnt=0;
            elseif (soc > 0.1)
              dynp=500*1;
              battpower=-dynp;
              battpower2=0;
              cnt=0;
            else
              if(sunny==0 && literp>0)  %d
```

```
dynp=500*1;
battpower=0;
battpower2=-500;
cnt=0;
elseif (sunny==0 && literp<=0)
dynp=0;
battpower=0;
battpower2=0;
cnt=0;
elseif (sunny==1)
if( literp>0 && cuschoice==0)
dynp=500*1;
battpower=0;
battpower2=-500;
cnt=0;
elseif ( literp<=0 && cuschoice==0)
dynp=0;
battpower=0;
battpower2=0;
cnt=0;
elseif ( literp>0 && cuschoice==1)
        if (literp>=70) %d
            dynp=500*3;
            battpower=0;
            battpower2=-dynp;
            cnt=0;
        elseif (literp>=50)
            dynp=500*2;
            battpower=0;
            battpower2=-dynp;
            cnt=0;
        else
            dynp=500;
            battpower=0;
            battpower2=-dynp;
            cnt=0;
        end
elseif ( literp<=0 && cuschoice==1)
dynp=0;
battpower=0;
battpower2=0;
cnt=0;
else
 dynp=0;
battpower=0;
battpower2=0;
cnt=0;
end
 else
 dynp=0;
```

```
            battpower=0;
            battpower2=0;
            cnt=0;
            end
          end

   else
      battpower=500;
      battpower2=0;
      dynp=500*3;
      cnt=0;
   end
end
```